Efficient Multi-Objective Optimization of an Automotive Crush Rail

Under Axial and Oblique Impact

by

David N. Booth

A thesis

presented to the University of Waterloo

in fulfillment of the

thesis requirement for the degree of

Master of Applied Science

in

Mechanical and Mechatronics Engineering

Waterloo, Ontario, Canada, 2021

AUTHOR'S DECLARATION

This thesis consists of material of which I authored or co-authored: see Statement of Contributions included in this thesis. This is a true copy of the thesis, including any required final revisions, as accepted by my examiners.

I understand that my thesis may be made electronically available to the public.

STATEMENT OF CONTRIBUTIONS

Sections of this work have been incorporated into a manuscript titled "Multi-Objective Optimization of a Multi-Cellular Aluminum Extruded Crush Rail Subjected to Dynamic Axial and Oblique Impact Loading Conditions." This manuscript was submitted for review on February 17, 2021, to the journal of *Thin-Walled Structures* for possible publication (TWST-S-21-00308). This manuscript is currently under review at the time of the writing of this thesis. The manuscript is co-authored by my supervisor Professor Kaan Inal, Dr. Christopher Kohar – a post-doctoral fellow, and myself. Professor Inal supervised this work, provided necessary resources, contributed to the review and editing of the manuscripts, and handled the project administration and funding acquisition. Dr. Kohar closely guided this project, provided invaluable advice, provided guidance in the original drafting of the manuscript, reviewed and edited the manuscripts to prepare it for publication, guided the conceptualization, aided in the development of the methodology and analysis, created some of the data visualizations, and wrote the custom Yld2004 material model subroutine for LS-Dyna.

The sections of this thesis are outlined here, with the relationships to the submitted paper indicated:

Abstract: The thesis version is expanded, and many sections are verbatim the same as the paper.

Chapter 1: Original to the thesis.

Chapter 2: Some descriptions of the RSM/ASA-RSM within Section 2.4 were adapted from the original draft of the manuscript. Similarly, the literature review and deficiency in the literature were adapted from the initial draft of the manuscript. The balance is original to this thesis.

Chapter 3: Original to the thesis.

Chapter 4: Many figures and tables from the manuscript are presented in the thesis. The written content of this section has been extended to include model verification, consideration of more impact angles, and more detailed information of the model construction.

Chapters 5 – 8: This is adapted from the original draft of the paper. It has been edited for coherence in this thesis.

Chapter 9: Original to the thesis.

ABSTRACT

Oblique impact conditions are of increasing research importance, and this kind of study is becoming more common in the crashworthiness literature. Optimization strategies, such as the Response Surface Methodology (RSM), are commonly used in a virtual design environment to investigate various loading conditions and configurations. However, the typical usage of the RSM in the crashworthiness literature does not take advantage of many recent enhancements to the RSM. This thesis presents a multi-objective shape optimization study of a multi-cellular aluminum extrusion subjected to dynamic axial and oblique (20° angled) impact loading conditions. Finite element models are developed, validated with experimental data, parameterized, and used to exhaust the design space using a complete factorial design of experiments. An analysis of different energy absorption characteristics, such as axial and oblique mean crush force, crush efficiency, and oblique impact coefficient, are presented. A multi-objective optimization problem is defined to generate new solutions that dominate a baseline profile in all aspects of performance, which produced a geometry with at least 6-17% improvements in energy absorption. The parametric study is used to define the "true" Pareto front, which is the set of non-dominated designs and the solution to the optimization problem. The RSM is used to perform the multi-objective optimization analysis. Feedforward neural networks and non-dominated sorting genetic algorithms (NSGA-II) are used as the metamodel and optimizer, respectively. This thesis research utilizes the Adaptive Surrogate-Assisted (ASA) - RSM, which is an advanced RSM approach, to perform the optimization analysis and demonstrate performance enhancements. The traditional RSM approach is compared to ASA-RSM in their speed and ability to correctly identify the actual Pareto front. The traditional RSM approach required approximately 63% of the entire domain to accurately identify the 94% of true Pareto front. The ASA-RSM was able to identify 87% of the true Pareto front using 25% of the entire domain. In some instances, the ASA-RSM was able to correctly identify the true Pareto front by using 33% of the domain. The traditional RSM approach was only able to correctly identify 10% of the true Pareto front when sampling less than 15% of the domain or using traditional stopping criteria. Depending on the configuration, the ASA-RSM achieved 40-80% accuracy in predicting the Pareto front when sampling up to 15% of the domain. This study provides a comprehensive understanding of the performance gains of multi-objective optimization in the application of structural crashworthiness considering various loading conditions.

ACKNOWLEDGEMENTS

I would like to thank my supervisor Prof. Kaan Inal for giving me the opportunity to be part of the Computational Mechanics Research Group (CMRG) at the University of Waterloo and for his leadership and support. I would like to acknowledge Prof. Sanjeev Bedi and Prof. Cliff Butcher, the members of my thesis review committee, who made sure of the quality of this thesis. Dr. Christopher Kohar edited this work in preparation for submission.

Special thanks and gratitude is due to Dr. Christopher Kohar of CMRG at the University of Waterloo for constantly supporting this project and for providing invaluable contributions across all areas of the work. His guidance and technical knowledge pushed the quality of this research to a higher level, and this work would not have been possible without him.

Thank you to all of the members of the CMRG, especially Daniel Connolly, for his many technical insights, explanations, and late-night company in the office; Larry Li for his interesting discussion; and Dr. Trevor Sabiston for recommending and introducing me to the group. Thanks go out to all of the graduate and undergraduate students and post-doctoral researchers in the office, especially Erin Grant, for her friendship and support; Sarah Pearce, for always being supportive; and Prusodman Sathananthan for reminding me to be excited about what I was learning. Thanks to all of the students and friends who organized lunches, brunches, and writing groups.

I would like to thank my friends outside the university, in Waterloo, Calgary, and elsewhere in the world for your encouragement and understanding. To Dominic Mayhew, Kristen Wesenberg, Steven Wong, Paris Hollenbeck, and Naanak Sodhi – thank you. Enormous thanks go to my amazing parents, who provided selfless support, life teachings, and who trusted in me and were always there for me. I would like to thank Justin McGirr for his remarkable friendship and unfailing companionship. Finally, to Becca Carmichael, thank you for everything.

TABLE OF CONTENTS

LIST OF FIGURES

LIST OF TABLES

1   INTRODUCTION

Government regulations place increasing demands on automotive manufacturers to develop fuel-efficient vehicles and reduce CO_2 emissions. The Company Average Fuel Consumption (CAFC) standards for Canadian vehicles between 2017 and 2025 require automakers to improve the fuel efficiency of their vehicles by 5% per year [1]. At the same time, crash test standards and demand for safe vehicles are increasing. The range of frontal crash tests performed by the Insurance Institute for Highway Safety (IIHS) has expanded over time from a single full-frontal crash into a rigid wall to include a 25% and 40% offset test on both the passenger and driver sides ([2], [3]). This creates an eccentric loading condition on the vehicle structure, known as oblique loading. The United States National Highway Traffic Safety Administration (NHTSA) has also proposed new standard crash tests to address much more challenging oblique frontal crash scenarios [4]. To meet these demands, it is essential to design lightweight and highly effective crash structures. Some parts of a vehicle structure, such as the front rails and bumpers, are ideal targets for weight reduction as they contribute significantly to the vehicle mass while providing little day-to-day functional use for an occupant. Lightweighting the vehicle frame is particularly effective because the overall vehicle then requires a smaller engine, lighter suspension, etc. Unfortunately, lightweighting and vehicle safety are often in conflict because a lighter vehicle frame can potentially offer less energy absorption capacity in a crash scenario. Thus, there is a need to design new crash structures that are lighter than the current state-of-the-art structures while improving crash performance. Furthermore, crash performance under impacts from multiple loading conditions must be considered in addition to the classic full-frontal crash.

Prior to developing a vehicle crash testing program, designers typically perform an extensive preliminary evaluation of the individual components subjected to representative loading conditions to anticipate their full-vehicle performance. Oblique impact loading of individual components has received more attention due to their representative behaviour of off-axis loading [5]–[7]. Many studies often focus primarily on axial crushing of components [8]–[10]. Since crash testing is destructive by nature, building physical prototypes of the individual components, let alone an entire prototype vehicle, for evaluating crash performance under multiple loading conditions is costly and time-consuming. More importantly, the "trial-and-error" process of physical testing is wasteful. Computational tools, such as finite element (FE) analysis, are heavily utilized to reduce the number of physical prototypes required to identify performance and design trade-off relationships. Designers can explore various designs and configurations in a virtual environment before the physical prototyping stage. However, FE simulations of crashworthiness are highly non-linear problems that require substantial computational resources. Even though FE modelling requires fewer

resources than physical prototyping, designers can become plagued by a virtual "trial-and-error" process that leads to long development cycles. Yet, the relative ease at which FE models can be evaluated allows the use of artificial intelligence and optimization algorithms to efficiently guide a designer in their design exploration (e.g. [11]–[14]). The Response Surface Methodology (RSM) [15] is a framework that is commonly employed in the optimization process of vehicle and component-level crashworthiness analysis (e.g. [16]–[19].). The RSM framework constructs a mathematical model, known as a metamodel, to predict an FE model's output response for a given set of inputs. Then, an optimization algorithm is performed on the metamodel to identify potential new designs for enhanced performance.

Various studies have been presented that utilize the RSM framework in multi-objective optimization of lightweight structures subjected to oblique impact loading [20]–[22]. Although these works show good performance in satisfying their specific optimization problem, many of these works perform the optimization step "out-of-loop." This means that the optimization process begins after the metamodel achieves good predictive capabilities. This creates a potential deficiency where the metamodel error has converged while the optimal set does not yet have sufficient resolution to be identified. Advancements in the RSM framework, such as the adaptive surrogate-assisted response surface methodology (ASA-RSM) by Stander [23], have brought the optimization process "into-the-loop" during the metamodel construction and sampling process. These are known as sequential, successive, or adaptive methods. This architecture modification can offer enormous potential in achieving more lightweight solutions efficiently with minimal increase in complexity. However, many of these works mentioned above do not systematically compare the result of their multi-objective optimization solution to the "true" solution to evaluate the suitability of their proposed framework.

The objective of the present work is to investigate the multi-objective optimization process of a multi-cellular aluminum extrusion under axial and oblique impact loading conditions. Recently, Kohar et al. [24]–[26] investigated the design optimization of extruded automotive aluminum front rails for energy absorption applications. A new front rail design, known as the UWR4, was developed using RSM and shown to outperform the energy absorption response of a Baseline profile. This result was verified using FE analysis and experimental testing by Zhumagulov [27]. However, Kohar et al. [24]–[26] only focused on analyzing a single (axial) loading condition. It is plausible that the UWR4 may be negatively affected by off-axis loading conditions, such as oblique impact. However, it is also possible that the UWR4 shows little to no sensitivity to oblique impact loading, such that a single objective that considers only axial loading is sufficient. The commercial software LS-Dyna is used to generate finite element simulations of these profiles, which are validated against experimental measurements presented by Zhumagulov [27]. Comparisons are presented between the UWR4 and the Baseline profile for various oblique loading

conditions. The FE model of the UWR4 is then selected for a parametric study to fully exhaust the design space using a complete factorial design of experiments with almost 10,000 simulations of different geometric design parameter combinations. This parametric study will identify trends between the different energy absorption criteria, define the true solution to the specified optimization problem, and be used to establish performance benchmarks for different optimization strategies. The traditional RSM approach, where optimization is performed after achieving metamodel convergence, will be compared with the ASA-RSM approach presented in Stander [23]. Accuracy and convergence speed in obtaining the true Pareto front are presented and discussed. This study will provide critical insight into the performance and value of the different optimization approaches.

This thesis is structured in the following manner: In Chapter 2, a review of the crashworthiness literature is provided, along with background information on FE methods and optimization, as they pertain to the present work. This chapter will also outline the current deficiencies in the literature. Chapter 3 summarizes the scope and objectives of this research to address the gap outlined in Chapter 2. Chapter 4 details the finite element models used in this work. This chapter includes details regarding the geometry of two aluminum extrusions used as automotive energy absorbers, their corresponding FE model construction, and verification with experimental measurements. In Chapter 5, the exhaustive parametric study of the UWR4 is presented. Chapter 6 formally introduces the multi-objective design optimization study considered in this thesis. The "true" solution to the multi-objective optimization problem is presented in this chapter. In Chapter 7, the traditional RSM solution is presented as a baseline metric for evaluating the capability of these optimization techniques in achieving the true solution to the multi-objective optimization problem. This chapter also presents a comparison between the traditional RSM approach and the ASA-RSM approach presented by Stander [23]. The key findings of this research are summarized in Chapter 8 with future recommendations and improvements outlined in Chapter 9.

2   BACKGROUND AND LITERATURE REVIEW

2.1   Experimental Crashworthiness

2.1.1 Vehicle Crashworthiness Testing

In the late 1970s, the National Highway Traffic Safety Administration (NHTSA) in the United States introduced the New Car Assessment Program (NCAP) for evaluating new vehicle designs for safety through means of destructive frontal crash testing at 35mph (56km/h) [28]. This government mandate later expanded to encompass various crash scenarios, such as side barrier impact (50km/h) and side pole impact (32km/h), shown in Figure 2.1. Since the inception of this program, the NCAP program has evolved to include advanced technology in occupant safety, such as supplementary restraint systems (e.g., seatbelts, airbags), and active accident prevention (e.g., forward collision warning systems, automatic emergency braking systems). These innovations in technology have led to a dramatic improvement in occupant safety.
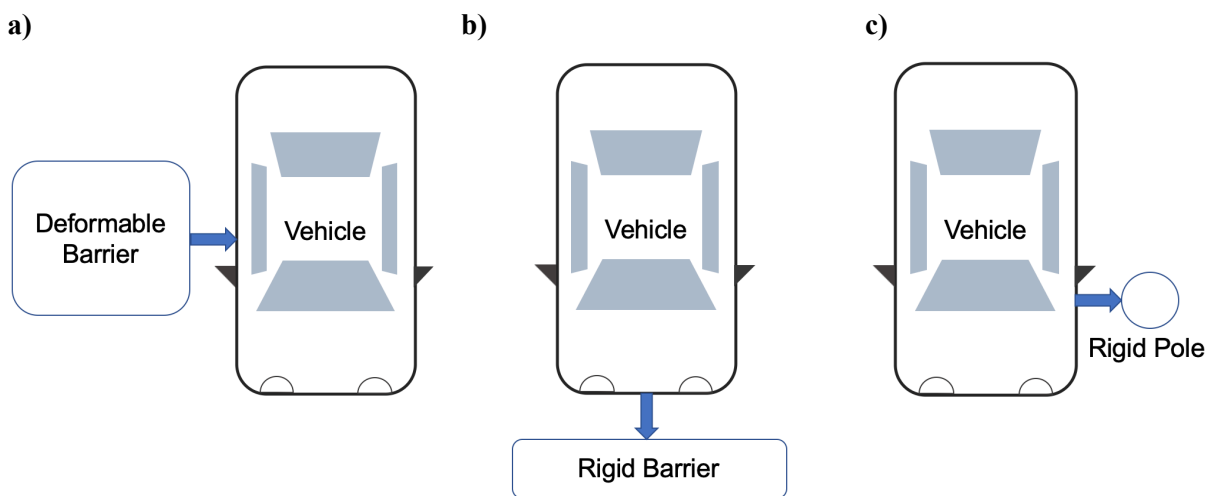
Figure 2.1: Schematic of the NHTSA a) Side Barrier, b) Frontal Impact, and c) Side Pole Impact Test.

Today, there are many regulatory agencies worldwide that have introduced their own NCAP program to evaluate new vehicles for safety. In addition to the United States government-mandated NCAP program, the Insurance Institute for Highway Safety (IIHS) is a third-party organization that performs testing and publishes its own standards for vehicle safety. The European NCAP (Euro-NCAP) program is the primary governing body for new vehicles for sale in Europe. Both the Euro-NCAP and IIHS program includes an offset frontal impact test that is far more challenging for engineers than frontal impact. Figure 2.2 presents a schematic of the offset frontal impact tests. In this loading condition, a vehicle is directed straight forward at 17.8m/s (64km/h) into a deformable barrier that overlaps only part of the front of the vehicle ([2], [3], [29]). This loading scenario introduces an oblique loading onto the vehicle, which causes

the vehicle to rotate. Rotation is extremely dangerous to vehicle occupants, to such an extent that the Brain Injury Criterion (BrIC) used by the NHTSA considers rotational velocity of the head as the sole indicator of brain injury risk [30]. The recent introduction of these tests is part of a growing trend of increasing standards for vehicle safety.
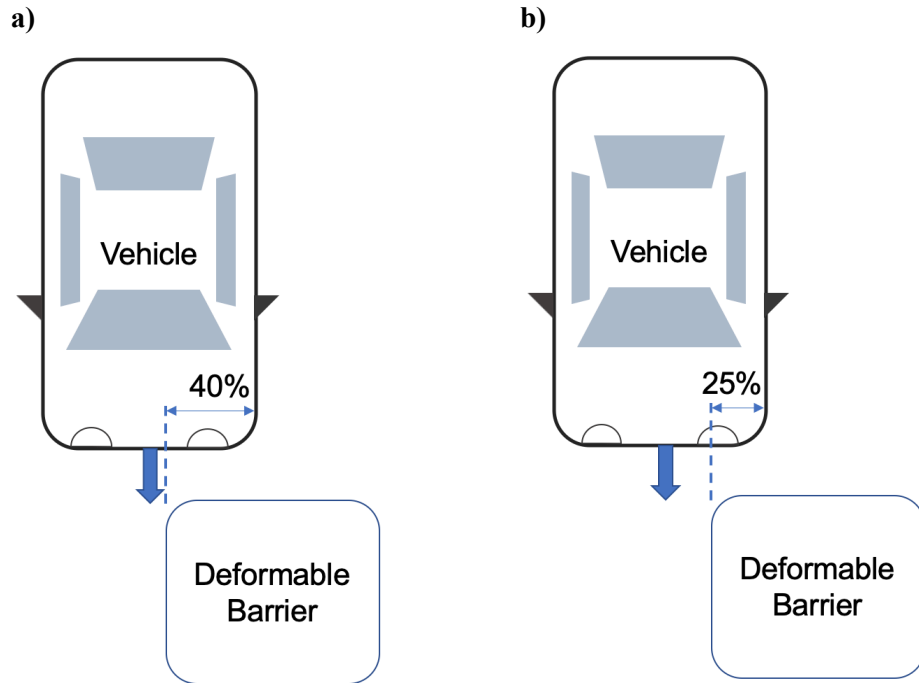
Figure 2.2: a) 40%-Overlap Test (IIHS and Euro-NCAP) and b) 25%-Overlap Test (IIHS).

These kinds of full-vehicle crash tests are extremely valuable and essential to any crashworthiness test program. Today, the structure of a vehicle is a highly complex, integrated system composed of many complex materials designed to dissipate as much kinetic energy as possible in the event of a crash. Every aspect of the vehicle design will play some part in the event of a crash. Yet, it is simply not possible to perform a comprehensive full-scale experimental crashworthiness program to enhance a vehicle's performance. This would require numerous prototype vehicles for destructive testing before production, which would drastically increase the engineering design cycle and cost.

2.1.2 Component Crashworthiness Testing

Due to the high cost associated with full-vehicle crash testing, automotive designers typically rely on preliminary evaluation of individual components subjected to representative loading conditions of their in-service performance. In the late 1950s, research began into the energy absorption properties of individual thin-walled tubes for their applications in light rail transit crash safety [31] and safety in nuclear energy structures [32]. Later, interest in thin-walled structures expanded into the automotive safety community for

their efficiency in mass, energy absorption, and packaging (e.g. [31]–[33]). Preliminary experiments were performed quasi-statically using a hydraulic press or dynamically in a drop tower apparatus under axial crushing conditions.

2.1.2.1   Experimental Testing of Components Under Axial Loading Conditions

Figure 2.3 presents experimental setups using the hydraulic press and a drop tower. In a quasi-static press, the specimen is fixed to a rigid plate, and a second rigid plate moves at a very slow speed (e.g. 0.508mm/s [27], 0.194mm/s [34]) to crush it while the reaction force is recorded. This simple test allows automakers to utilize widely available hydraulic equipment to obtain a lot of useful information, such as force-displacement and deformation behaviour. However, automotive crash is a highly dynamic process with important inertial and strain-rate effects. In the drop tower experiment, a mass (typically 80 – 100kg) is raised above a specimen and released to achieve a maximum impacting speed of approximately 11m/s (40km/h) [35]. Although this captures the strain-rate effect, this requires an increase in the complexity of the apparatus. More importantly, the drop tower experiment is often limited by the total amount of input energy (i.e., ~3000N-m with 100kg at 3 m) generated by elevating a mass to a height.

More recently, linear crash sled testing apparatuses have been developed to overcome this deficiency. Figure 2.4 presents a linear crash sled apparatus setup at the University of Waterloo. In this setup, a compressed air accumulator fires an instrumented linear mass along a set of rails into a rigid wall with an instrumented component mounted to it. These sleds can use heavy masses (up to 1400kg) that can be propelled to high enough speeds (up to 90km/h) to replicate the energy (169500N-m) involved in a vehicle crash event (e.g. [36]). Load cells on the fixed side record the forces during the crushing process, and equipment such as high-speed cameras can be used to determine the kinematics of the crash event.

2.1.2.2   Experimental Testing of Components Under Oblique Loading Conditions

Due to the vast amount of kinetic energy involved, off-axis and oblique impact tests present a significant projectile hazard in a linear sled setup, and are still typically performed in the confinement of a drop tower (e.g. [35]) or quasi-static press (e.g. [34]). The test apparatus used by important experimental works are shown in Figure 2.5. Drop tower testing of oblique crushing was initially performed in the mid 1980s and led by Reid and Reddy [35], who studied axial and oblique crushing of tapered rectangular tubes. The oblique impact angle was set to be equal to the taper angle, such that one side of the tube was colinear with the axis of the impacting mass. This reduced the risk of a projectile hazard. Oblique quasi-static press experiments were performed on square tubes by Reyes et al. [34][39][40]) and conical tubes by Ahmad et al. [39]. There are some variations in the experimental setup: Reid and Reddy [35] and Ahamad et al. [39] fixed the tube to the moving portion of the apparatus, while Reyes et al. [34][39][40] fixed it to the

stationary base. In all cases, the kinematics of the setup are similar: a tube is mounted to an angled surface, and crushed by a flat surface, such that there is an angle between the axis of the tube and the line of action of the crushing force.

a)

b)
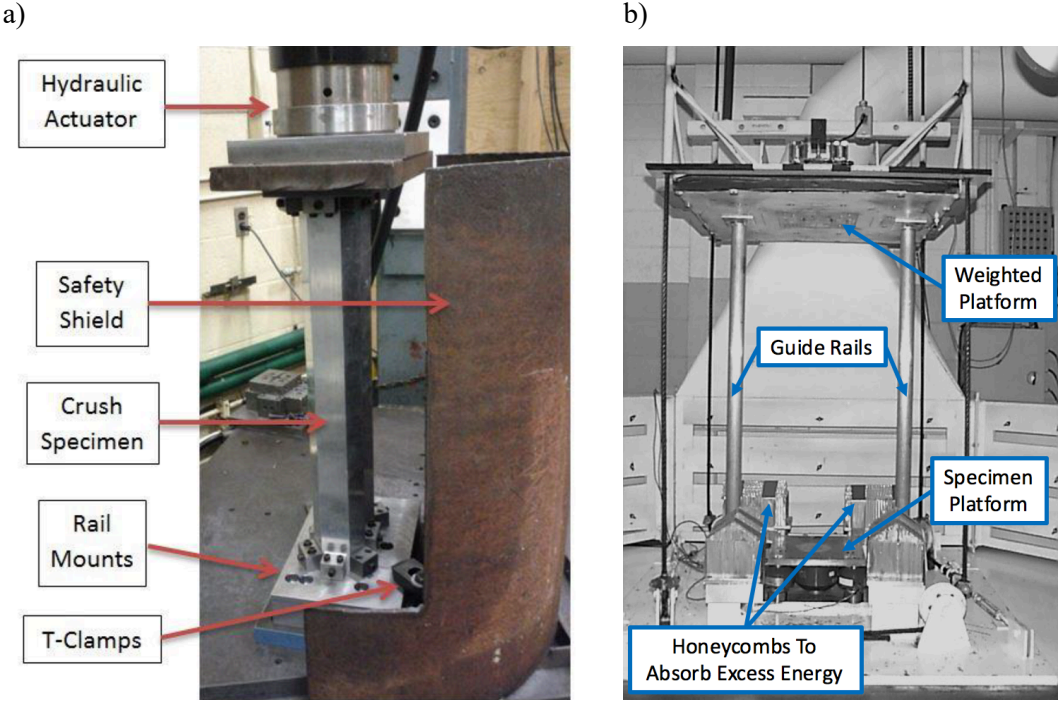
Figure 2.3: a) Hydraulic Press Setup for Quasi-static [27] and b) Drop Tower Setup for Dynamic Crush Testing [40].
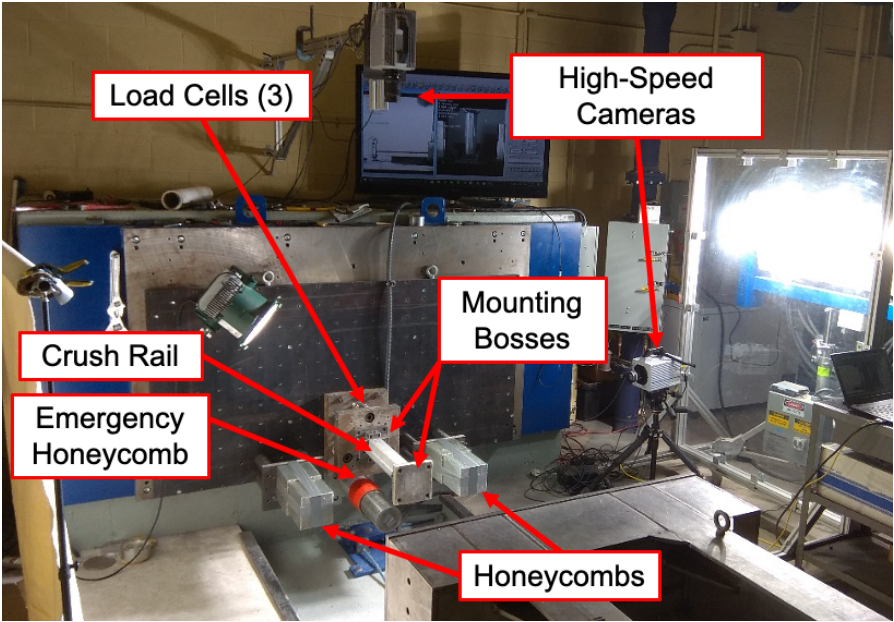
Figure 2.4: Linear Crash Sled Setup at University of Waterloo [41].
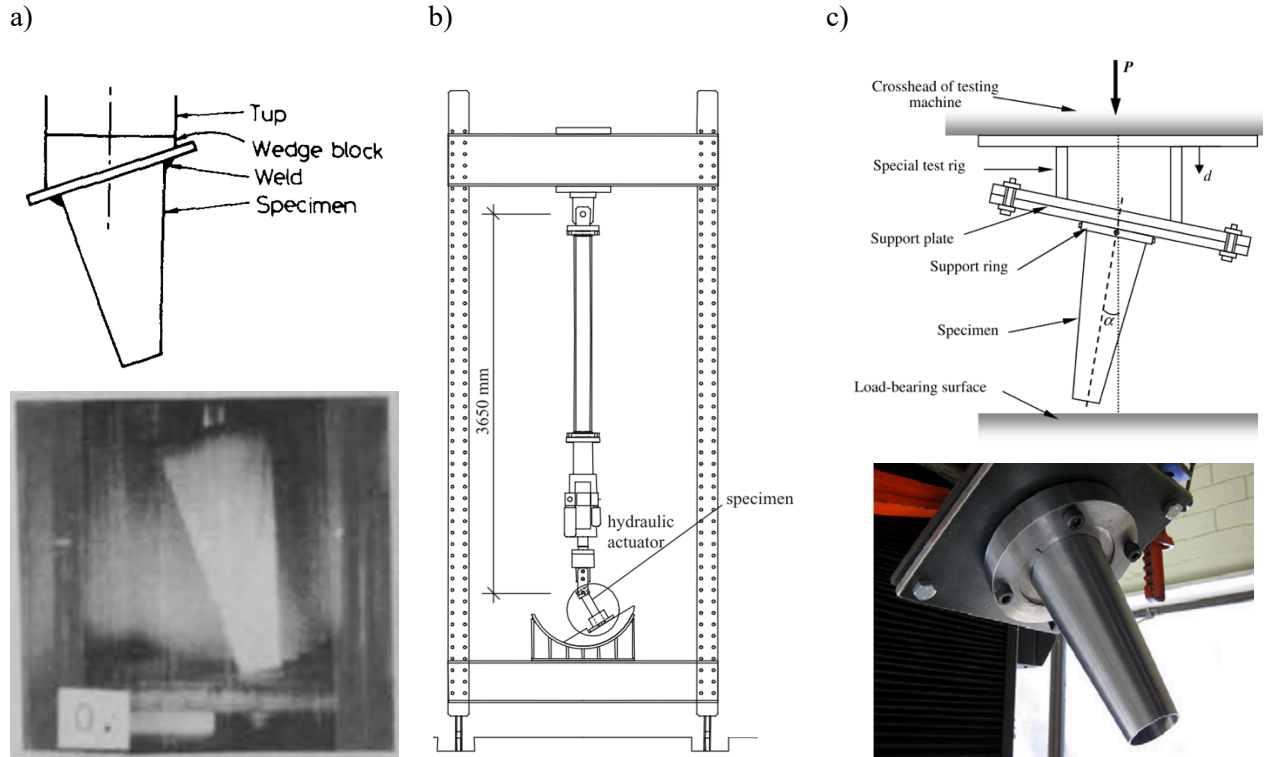
Figure 2.5: Oblique Impact Experimental Apparatus: a) Drop Tower Used by Reid and Reddy [35], b) Quasi-Static Press used by Reyes et al. [34], c) Quasi-Static Press used by Ahmad et al. [39].

Component-level testing allows structural components to be designed for crashworthiness more rapidly and at a lower cost than full-vehicle tests. In general, the knowledge from a component-level test can be transferred to the performance of a full-vehicle crash. However, full-vehicle testing is still required to ensure that the interaction between components does not produce unexpected behaviour.

2.1.3 Mechanics of Experimental Crushing

2.1.3.1   Mechanics of Axial Crushing of Thin-Walled Structures

Thin-walled structures undergo various deformation modes during axial crush. In the 1980s, Jones and Abramowicz [42][43] performed extensive drop tower experiments of axial crushing of square tubes to identify these key deformation modes. Their pioneering work identified four deformation modes: inextensional, extensional, mixed, and bending. Each of these deformation modes has an implication on the experimental force-displacement response. Jones and Abramowicz [42] reported that the inextensional mode was the most common deformation mechanism for axial crushing for square tubes. Figure 2.6 presents square crush rails with inextensional, extensional, and mixed crush patterns. Inextensional folding is thus named because the in-and-out pattern generates little circumferential extension of the tube.

8

In some cases, the extensional folding mechanism was observed, where the hinge deformation is entirely outwards or entirely inwards, causing substantial circumferential extension. This deformation mechanism absorbs more energy because more deformation is associated with stretching than plastic hinging in the inextensional mode. It is also possible for mixed modes to form where both inextensional and extensional folds are present. For example, Figure 2.6c presents a case where the bottom fold consists of three lobes that folded outwards (causing extensional deformation) and one which folded inwards. In some cases, typically only in long slender tubes [44], there is a transition to an overall bending mode, shown in Figure 2.7, called global buckling. This deformation mode has the worst energy-absorption characteristics because it only involves a single fold. Bending deformation is more common in oblique impact cases and is discussed in more detail in Section 2.1.3.2 below.

a)   b)   c)
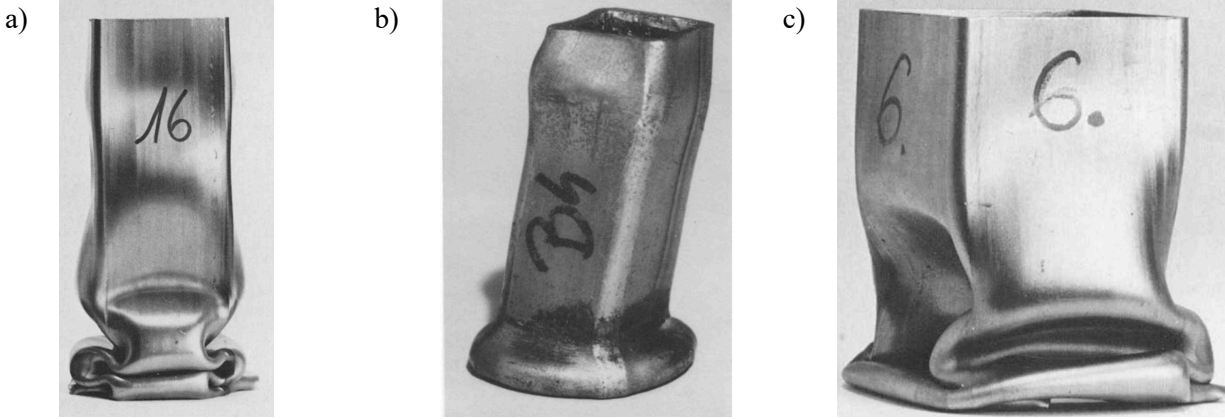
Figure 2.6: Axially Crushed Square Tube with a) Inextensional, b) Extensional and c) Mixed Crush Modes [43].
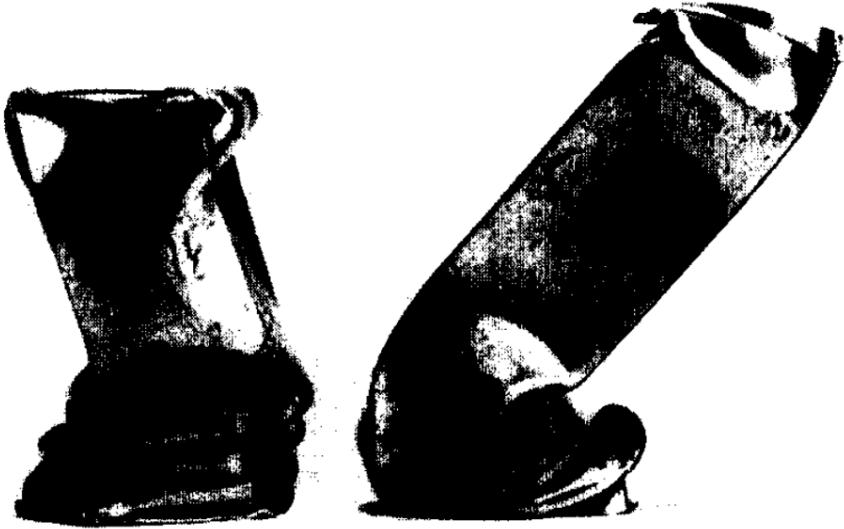
Figure 2.7: Bending Mode of Axially Crushed Square Tubes [42].

Figure 2.8 presents a typical force response, F(x), as a function of displacement, x, during the axial crushing of a hollow square tube up to a crushing displacement, δ. During the initial phase of deformation, there is an initial elastic loading of the structure until it reaches its elastic limit. Once the structure reaches its elastic limit for a thin-walled structure, the structure yields due to compression, forms a plastic hinge, and begins to crush. As a result, there is a sudden drop in the force-displacement response during the plastic hinge formation. This initial peak typically corresponds to the highest observed force, known as the peak crush force, F_{peak}. As the plastic hinge forms a complete lobe, the structure begins to stiffen through direct contact of the lobe against the structure. This causes a sudden increase in the force that causes a new plastic hinge to form. However, due to the instability and inhomogeneity of the previous fold, the force required to generate the sequential fold is lower than the initial peak force. This process continues in an oscillatory manner of progressive crushing that dissipates the kinetic energy through plastic deformation.

Multi-cellular crush tubes have more complicated deformation patterns, including mixed-mode folds, and more complicated force-displacement responses. Figure 2.9 presents an example of a multi-cellular crush tube and the experimentally measured crush force-response. Multi-cellular tubes typically have a higher mean force response because the folds interact with one another and stiffen the structure as it deforms. The force-displacement response is typically more chaotic, as folds in various tube regions are formed at different times.
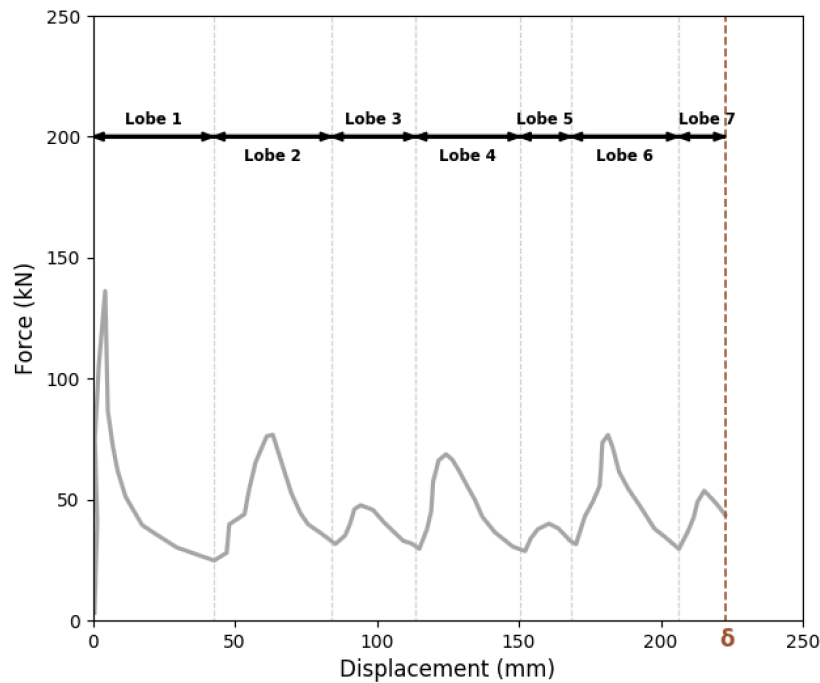
Figure 2.8: Typical Force-Displacement Response during Axial Crush.
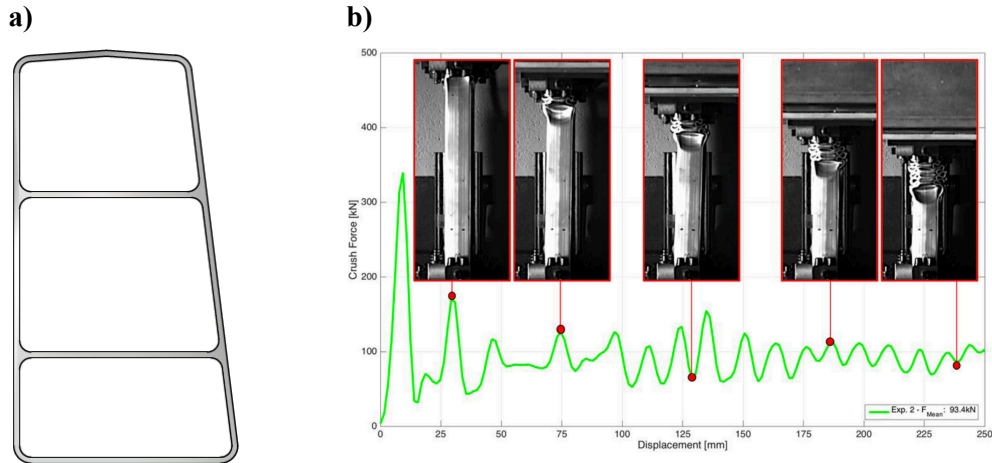
Figure 2.9: a) Cross Section of Multi-Cellular Rail and b) Force-Displacement Response during Dynamic Axial Crush [25].

2.1.3.2   Mechanics of Oblique Crushing of Thin-Walled Structures

Like axial impacts, oblique impacts may produce inextensional, extensional, mixed, and bending deformation modes. However, some degree of global bending, which is rare in axial impacts, is ubiquitous in oblique impact cases. Reyes et al. [34][39][40] observed that squares loaded at an angle to their longitudinal axis would buckle globally in a quasi-static press. Figure 2.10 presents the resultant deformation and force-displacement response of the global bending mode. Once this deformation mode begins, it dominates the collapse, and the entire tube deforms in a global buckling mode. With only a single plastic hinge, the bending deformation mode tends to be extremely inefficient in dissipating energy compared to the local buckling and progressive folding mechanisms. This is seen in the force-displacement response, where the crushing force monotonically decreases after the initial peak. Thus, this deformation mechanism is undesirable in vehicle crashworthiness applications.
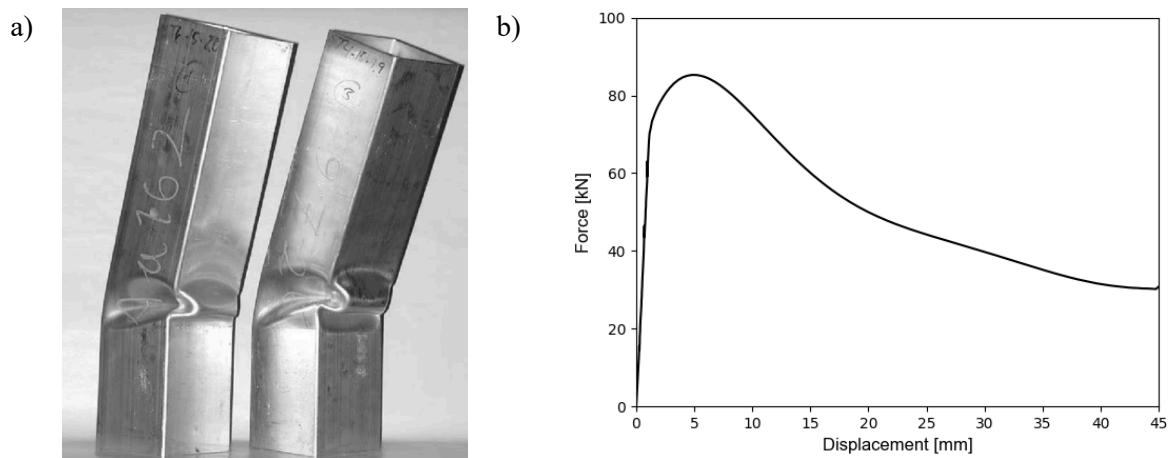
Figure 2.10: a) Global Buckling Mode and b) Typical Shape of the Global Buckling Force-Displacement Curve, as Presented in Reyes et al [37].

11

Although oblique impact generally causes some degree of bending deformation to occur, it does not always cause global buckling. In many cases, there will be a combination of bending and progressive crush modes. This is common in vehicle crashworthiness applications due to the various interactions of components and multi-cellular structures. An example of the first case can be found in the work of Zhang et al. [45], shown in Figure 2.11a. This is a significant result because it highlights that the combination of bending and progressive crush is prevalent in real-world crashworthiness applications. Multi-cellular structures are generally more robust in oblique impact than single-cellular structures because it is more difficult for a single plastic hinge to form and cause global buckling. Figure 2.11b shows a simulation of a multi-cell triangular tube impacted at a 15° angle from a study by Tran [46]. The combination of bending and progressive crush is exhibited. Further examples can be seen in the studies by Qi et al. [7] and Yang et al. [5]. This combination of bending and crushing is responsible for the reduced energy absorption in oblique crush. Bending deformation absorbs less energy than crushing, and there is proportionally more bending deformation as the impact angle is increased. At sufficiently large impact angles, global buckling will still occur.

a)   b)
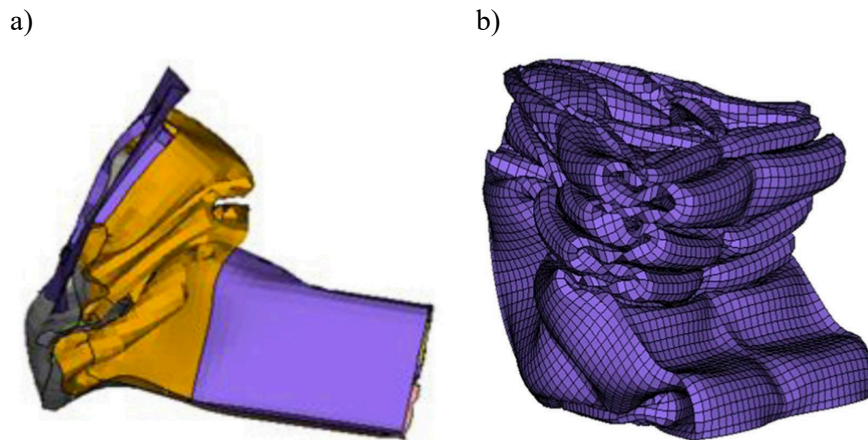
Figure 2.11: Deformed Shape of Obliquely-Impacted Crush Rails: a) Crush Rail from Full-Vehicle Model [45], b) Multi-Cell Triangular Tube [46].

2.1.4 Measuring Performance from Component-Level Testing

From these instrumented experiments, several metrics for evaluating a component's performance during crush can be determined. Hanssen et al. [47] identified a comprehensive summary of performance metrics commonly used for component performance evaluation during axial crush. The peak crush force, F_{peak}, is defined as

$$F_{peak} = Max(\,F(x)\,)\,, 0 \leq x \leq \delta \tag{2.1}$$

The energy absorbed, EA, by the structure is a key performance metric defined as

$$EA = \int_0^\delta F(x)dx \tag{2.2}$$

Another critical performance metric is the mean crush force, F_{mean}, which is defined as

$$F_{mean} = \frac{EA}{\delta} \tag{2.3}$$

Hanssen et al. [47] also introduced the concept of crush efficiency, η_{crush}, as a metric for evaluating performance, such that

$$\eta_{crush} = \frac{F_{mean}}{F_{peak}} \tag{2.4}$$

where an ideal structure would have a crush efficiency of $\eta_{crush} = 1.0$. To differentiate between structures that have similar energy absorption but have different mass, Andrews et al. [48] introduced the specific energy absorption, SEA, which is defined as

$$SEA = \frac{EA}{Mass} = \frac{F_{mean}\delta}{Mass} \tag{2.5}$$

These metrics may be defined for either axial or oblique crush, with no change to their calculation. A superscript may be used to indicate the impact scenario (as in Equation 2.6). If not otherwise indicated, values should be assumed to refer to axial crushing.

The force-displacement response for a singular crush tube will be different in axial and oblique impact. Thus, additional performance metrics may be defined to capture the relationship between the axial and oblique performance. Tran et al. [49] defined the *oblique impact coefficient* as the relationship between the axial force and the oblique force, such that

$$\lambda_{mean} = \frac{F_{mean}^{oblique}}{F_{mean}^{axial}} \qquad \lambda_{peak} = \frac{F_{peak}^{oblique}}{F_{peak}^{axial}} \tag{2.6}$$

The oblique impact coefficients are important metrics of the crush performance, as they not only characterize the oblique impact performance given axial performance but can also be thought of as representing the sensitivity of a particular design to oblique loading. Tran et al. [49] found that the oblique impact coefficient for the shapes studied in their work remained approximately constant for a given impact angle, with small higher-order secondary effects caused by changes in the geometry of the profiles.

13

2.2 Analytical Modelling of Crashworthiness

Many researchers have made contributions to the field of analytical crush modelling. In these works, the emphasis is on developing a mathematical model of the crush process based on the principles of mechanics. These serve as initial hand-calculations that are useful for preliminary design generation, which can provide crucial insight into the structure's crush mechanics. Alexander [32] presented some of the earliest works in the field of analytical crush mechanics. In this fundamental work, an analytical expression was derived for the mean crushing force of a rigid-perfectly-plastic cylindrical tube undergoing progressive folding and crushing. Alexander [32] determined that two sources contributed to the energy absorption: bending and stretching. The expression for the mean crushing force in a cylindrical tube was derived as

$$F_{mean} = [hH\pi] + \left\{\frac{2h^2 r\sigma_{ten}}{H}\right\} \tag{2.7}$$

where h is the wall thickness, r is the tube radius, σ_{ten} is the yield strength in tension, and H is the half of the length of the tube that is involved in a single fold (the "half-wavelength"). The first term in the square brackets represents the contribution from the material stretching, and the other term represents bending. The relationship between each term and H is of critical importance to understanding tube crush mechanics. Long wavelengths increase the force required to stretch the material, and short wavelengths increase the force required to bend the material. Alexander [32] assumed that the system would take on a deformation pattern that naturally minimizes energy absorption and thus crushing force. In other words, H will take on a value that minimizes Equation 2.7 ($\partial F_{mean}/\partial H = 0$). Performing this minimization and substituting the result back into Equation 2.7, the final result produced by Alexander [32] was

$$F_{mean} \propto h^{1.5}\sigma_{ten}\sqrt{r} \tag{2.8}$$

Wierzbicki and Abramowicz [50] performed a detailed analytical study on the crushing mechanics of square tubes undergoing either *Type I* (Figure 2.12a) or *Type II* deformation (Figure 2.12b). The model is a kinematically admissible "super folding" collapse element created from four plane surfaces, two conical surfaces, two cylindrical surfaces, and one toroidal surface (Figure 2.12c). Analytical approximations of the mean crushing force are derived using the same method as Alexander's derivation, with C as the tube width

$$\text{Type I:} \quad F_{mean} = 9.56h^{\frac{5}{3}}\sigma_y C^{\frac{1}{3}} \tag{2.9}$$

$$\text{Type II:} \quad F_{mean} = 4\sqrt{\pi C}h^{1.5}\sigma_y + 2h^{1.5}\sigma_y \tag{2.10}$$
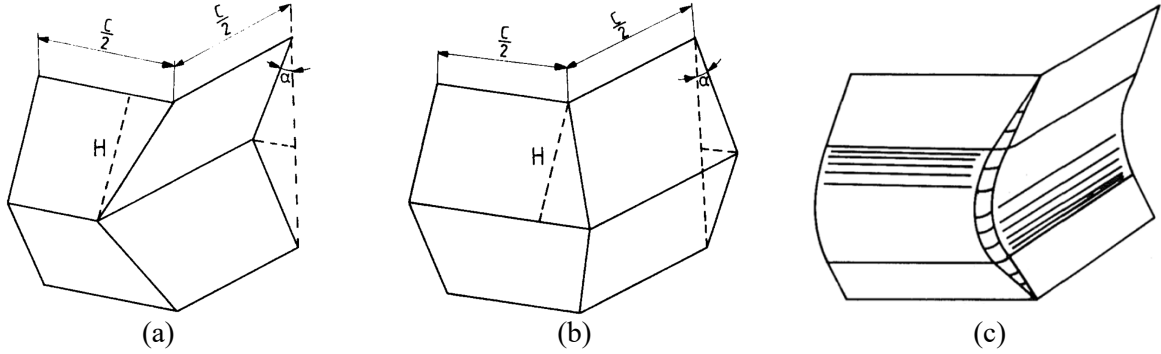
Figure 2.12: Illustration of Kinematically Admissible Collapse Elements, a) Simplified Type I, b) Simplified Type II, c) Type I with all Kinematic Features [50].

Wierzbicki et al. [51] introduced a "super beam" element to extend the super folding element to incorporate cases of bending and combined bending/compression. For a square tube in bending, the mean force was determined to be

$$F_{mean} = 1.71\pi\sigma_y h^{5/3} C^{1/3} \tag{2.11}$$

To account for work hardening, Chen and Wierzbicki [52] introduced an "energy equivalent flow stress" that is the average flow stress between the yield point and ultimate strain. This equivalent flow stress is given by

$$\sigma_{equiv} = \frac{1}{\varepsilon_u} \int_0^{\varepsilon_u} \sigma d\varepsilon \tag{2.12}$$

where ε_u is the ultimate strain. A convenient closed-form solution can be found by utilizing an analytical hardening model, such as the power-law model, where the equivalent flow stress is defined as

$$\sigma_{equiv} = \sqrt{\frac{\sigma_0 \sigma_{UTS}}{n+1}} \tag{2.13}$$

An extension of these models to include material strain-rate effects is possible by assuming the strain-rate is constant and uniform. Abramowicz and Jones [43] proposed that the strain rates in Type I and II collapse elements can be computed based on the impact velocity (V) and width provided by

$$\dot{\varepsilon} = \frac{V}{3C} \text{ (Type I), and } \dot{\varepsilon} = \frac{V}{4C} \text{ (Type II)} \tag{2.14}$$

Assuming the material follows a Cowper-Symonds [53] strain rate sensitivity model, the dynamic effects can be accounted through

$$\sigma_{equiv}^{Dynamic} = \sigma_{equiv}\left(1 + \left(\frac{\dot{\varepsilon}}{M}\right)^{\frac{1}{q}}\right) \tag{2.15}$$

where M and q are the Cowper-Symonds strain rate sensitivity parameters.

Chen and Wierzbicki [52] proposed one of the first attempts of analytical modelling of multi-cellular structures by using a simplified version of the super folding element to calculate peak force for multi-cell columns. Their approach was based on dividing the tube into distinct "angle elements" that are assumed to contribute to the overall response individually. Figure 2.13 illustrates this concept by showing an example geometry and an exploded view with the angle elements separated. The number of flanges in each angle element is indicated in Figure 2.13b. The total number of flanges in each intersection point is summed to produce a final value of N_f for the tube ($N_f = 14$ in Figure 2.13b). This value was then used to predict the peak crushing force as

$$F_{peak} = \frac{2}{3}\sigma_{equiv}h\sqrt{\pi N_f A} \tag{2.16}$$

where A is the cross-sectional area of the structure. Zhang et al. [54]–[59] extended the approach of Chen and Wierzbicki [27] by performing numerous studies to develop analytical models for different types of angle elements. They contributed predictive mean force equations for various angled elements, three-panel elements, and four-panel elements.

a)   **b)**
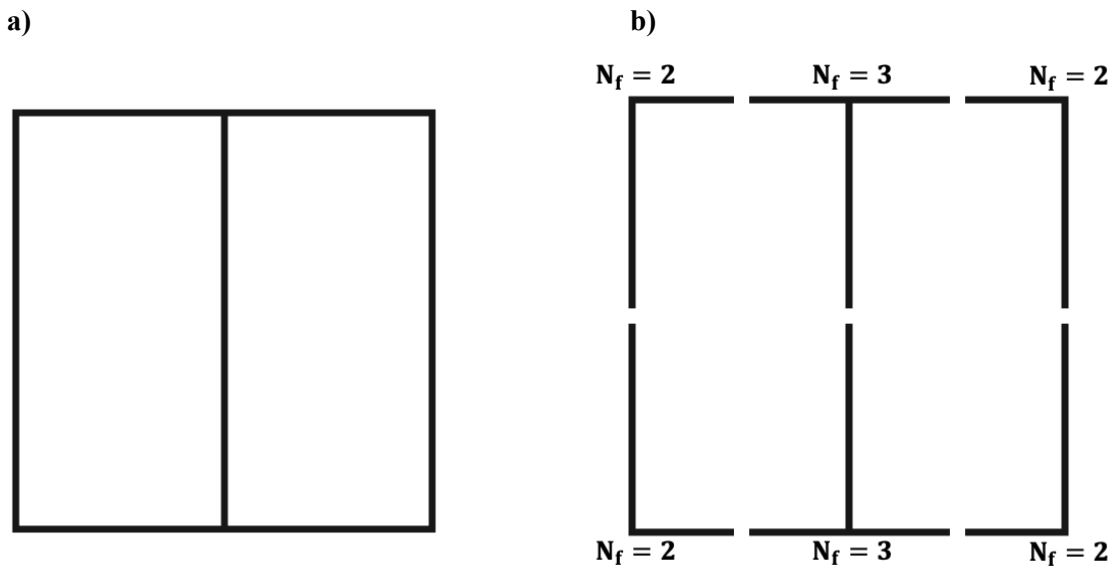
Figure 2.13: a) Multi-Cellular Structure and b) Exploded View Showing Angle Elements and Flanges per Element.

There is also literature that focuses on predicting the final consolidated length of the structure. Abramowicz [60] performed an analysis on the shapes of the folds in order to provide an estimate for the length of the tube after crushing. It was found that the crushing distance (δ) in a square column is

$$\delta \cong 0.7l \qquad (2.17)$$

where l is the initial length. Wierzbicki and Abramowicz [50] investigated the concept of *solidity ratio*, ϕ, defined as

$$\phi = \frac{A}{A_p} \qquad (2.18)$$

where A is the cross-sectional area of the actual tube material, and A_p is the cross-sectional area enclosed by the outer perimeter of the tube. For square tubes, they analytically determined that, given constant cross-section and yield stress, the mean force should be proportional to solidity to the power of two-thirds. Meran [61] later performed a numerical study on solidity ratio and arrived at similar conclusions. Although these analytical models provide closed-form solutions to a reasonably complex phenomenon, such as crushing, higher fidelity is often required for crashworthiness applications. In many of these analytical models, simplifications with respect to the material and geometry behaviour are often made to facilitate the approach. They are also limited in capturing all physical phenomena involved in the process and are typically limited to axial impacts of single-cell structures.

2.3   Numerical Simulation of Crashworthiness

Over the past few decades, the availability of high-performance computing technologies has revolutionized the development process of engineered systems. Although physical experimentation can provide direct insight into evaluating performance, the "trial and error" experimental approach to product development is often plagued with high cost and high development time. As such, scientists and engineers have turned to using computational techniques, such as numerical modelling, to perform virtual experiments of their system prior to production. This allows a scientist or engineer to rapidly explore the design space without the need for costly experiments. In the automotive industry, the commonly employed computational technique for modelling crashworthiness problems is commercial finite element packages, such as LS-Dyna. LS-Dyna is a nonlinear multi-physics finite element package for evaluating the large deformation response of structures [62]. This also allows scientists and engineers to incorporate nonlinear phenomena, such as large deformation and rotation, contact with multiple bodies and self-contact, and nonlinear constitutive response, into the crush calculations that cannot be accomplished using analytical methods. However, achieving high accuracy levels with finite elements, which is critical for evaluating

crashworthiness, is still challenging. Even with recent technological advances, accurate finite element simulation of crashworthiness is still a computationally expensive task that requires significant attention to capture all these nonlinearities. In the present work, LS-Dyna will be used to perform computational component-level crashworthiness experiments. The following section presents an overview of the nonlinear finite element formulation employed in this work and its application to the simulation of crashworthiness.

2.3.1 The Finite Element Method

Most engineering systems can be defined using partial differential equations over some domain (in structural applications – usually the geometry of the body). Solving such equations analytically for any domain and any combination of initial conditions or boundary conditions is generally not possible. The finite element (FE) method is a numerical method that approximates the solution to a time and boundary value problem that is governed by partial differential equations. The FE method is very popular in engineering due to its ability to solve various problems, including many physical effects. A brief overview of the theory and its application to crashworthiness is provided in this section. Detailed derivations for linear problems can be found in Belytschko and Fish [63] and Hughes [64]. The extension to nonlinear problems is described in great detail by Belytschko and co-authors [65], and specifics of the implementation of the theory in LS-Dyna are available in the LS-Dyna theory manual [62].

The method involves creating a discretized model of the system (mesh) that consists of points (nodes) and the connections between the points (elements). An example of this is illustrated in Figure 2.14. The problem is then solved at the nodes of the discretized domain. The solution at any point in the domain (within the elements) can be found using interpolation functions, known as *shape functions*, which are associated with the elements. The number of elements into which the domain is divided is a critical factor in the accuracy of the final solution. The usual terminology refers to how *fine* or *coarse* the mesh is, and the typical approach is to begin with a coarse mesh and perform *mesh refinement* to successively finer meshes until the desired accuracy is achieved.

In the application of crashworthiness, the governing partial differential equation in strong form is the conservation of momentum, given by the Cauchy momentum equation, as

$$\nabla \boldsymbol{\sigma} + \rho \mathbf{f}_{body} = \rho \ddot{\mathbf{u}} \tag{2.19}$$

where σ is the Cauchy stress tensor, ρ is density, f_{body} is the body force, and $\ddot{\mathbf{u}}$ is the body acceleration. Note that $\ddot{\mathbf{u}} = \frac{D\mathbf{v}}{Dt} = \frac{\partial \mathbf{v}}{\partial t} + \frac{\partial \mathbf{v}}{\partial \mathbf{X}} \frac{\partial \mathbf{X}}{\partial t}$. In a Lagrangian coordinate system $\frac{\partial \mathbf{X}}{\partial t} = 0$, so $\ddot{\mathbf{u}} = \frac{\partial \mathbf{v}}{\partial t}$. The nodal displacements are used as an input in this equation (primarily for calculating stress), which allows for the

subsequent calculation of the accelerations and the completion of the time integration scheme (discussed in Section 2.3.1.1). The system is also subject to traction stress, $\bar{\mathbf{t}}$, along Γ_t, and displacement boundary conditions, $\mathbf{u} = \bar{\mathbf{u}}$, along Γ_u (Figure 2.14).
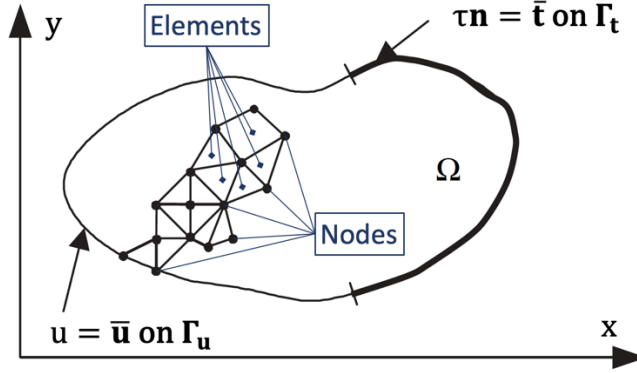
Figure 2.14: Example 2D Body, Partly Meshed with Example Nodes and Elements Labeled.

Through the standard method of introduction of a trial function ($\boldsymbol{\omega}$) and integration by parts, the strong form of the second-order partial differential equation can be reduced to a weak form first-order partial differential equation as [62]

$$\int_\Omega \rho\boldsymbol{\omega}\ddot{\mathbf{u}}\,d\Omega + \int_\Omega \boldsymbol{\nabla}\boldsymbol{\omega}\,\boldsymbol{\sigma}d\Omega - \int_\Omega \rho\boldsymbol{\omega}\,\mathbf{f_{body}}d\Omega - \int_{\Gamma_t} \boldsymbol{\omega}\bar{\mathbf{t}}\,d\Gamma_t = 0, \qquad \boldsymbol{\omega} = 0 \text{ on } \Gamma_u \qquad (2.20)$$

Note that in the above, there are certain mathematical restrictions, particularly that the trial function must be a member of the first Hilbert space. For more detail, the reader is referred to [63] or [64]. Using a set of interpolation functions, $\mathbf{N}(\xi, \eta, \zeta)$, the discretized form of the system is defined as

$$\mathbf{u}(\mathbf{X}, t) = \sum \mathbf{N}(\xi, \eta, \zeta)\mathbf{u}(t) \qquad (2.21)$$

where $\mathbf{u}(t)$ is the displacements of the nodes and $\mathbf{N}$ is a matrix of Lagrange polynomials that interpolate the displacements throughout the elements. A brief discussion of element types is given in Section 2.3.1.3. The gradient of displacement is calculated as

$$\frac{\partial \mathbf{u}}{\partial \mathbf{X}}(\mathbf{X}, t) = \sum \frac{\partial \mathbf{N}(\xi, \eta, \zeta)}{\partial \mathbf{X}}\mathbf{u}(t) = \sum \mathbf{B}(\xi, \eta, \zeta)\mathbf{u}(t) \qquad (2.22)$$

where $\mathbf{B}(\xi, \eta, \zeta) = \frac{\partial \mathbf{N}(\xi,\eta,\zeta)}{\partial \mathbf{X}}$. Thus, strain tensors can be defined as functions of nodal displacements. These shape functions are constant with respect to time, which leads to

$$\ddot{\mathbf{u}}(\mathbf{X}, t) = \sum \mathbf{N}(\xi, \eta, \zeta)\ddot{\mathbf{u}}(t) \tag{2.23}$$

In Galerkin's finite element method, the shape functions, $\mathbf{N}$, are used as the trial function, $\boldsymbol{\omega}$ [63]. The summation of each finite element leads to the discrete finite element equations for the governing equations

$$\sum_{e=1}^{\#\,\text{elems}} \left\{ \int_{\Omega^e} \rho[\mathbf{N}^{(e)}]^{\mathrm{T}}[\mathbf{N}^{(e)}][\ddot{\mathbf{u}}^{(e)}]d\Omega + \int_{\Omega^e} [\mathbf{B}^{(e)}]^{\mathrm{T}}[\boldsymbol{\sigma}^{(e)}]d\Omega - \int_{\Omega^e} \rho[\mathbf{N}^{(e)}]^{\mathrm{T}}\mathbf{f}_{\text{body}}d\Omega - \int_{\Gamma_1} [\mathbf{N}^{(e)}]^{\mathrm{T}}\bar{\mathbf{t}}d\Gamma \right\} = 0 \tag{2.24}$$

Using Gauss-Quadrature for integrating the spatial equations, the discrete finite element equations can be expressed in a condensed form that follows the method of direct assembly to develop the global equation from the element-level terms

$$[\mathbf{M}][\mathbf{a}] + [\mathbf{F}] - [\mathbf{P}] = 0 \tag{2.25}$$

where $[\mathbf{a}]$ is a vector of all nodal accelerations, $[\mathbf{M}]$ is the mass matrix defined as

$$[\mathbf{M}] = \sum_{e=1}^{\#\,\text{elems}} \left\{ \int_{\Omega^e} \rho[\mathbf{N}^{(e)}]^{\mathrm{T}}[\mathbf{N}^{(e)}]d\Omega \right\} \tag{2.26}$$

$[\mathbf{F}]$ is a vector consisting of all internal forces defined by

$$[\mathbf{F}] = \sum_{e=1}^{\#\,\text{elems}} \left\{ \int_{\Omega^e} [\mathbf{B}^{(e)}]^{\mathrm{T}}[\boldsymbol{\sigma}^{(e)}]d\Omega \right\} \tag{2.27}$$

where $[\boldsymbol{\sigma}^{(e)}]$ is the internal stress generated within an element. Calculating the stress can be a complex operation. Stress is a function of displacements (typically through the strain tensor) and various other state variables that are tracked throughout the deformation. This term represents the role of the constitutive model in the solution of the problem and can be responsible for a large part of the computational cost. Details about the constitutive model are presented in Section 2.3.2. $[\mathbf{P}]$ is a vector consisting of all external forces acting on the body, defined by

$$[\mathbf{P}] = \sum_{e=1}^{\#\,\text{elems}} \left\{ \int_{\Omega^e} \rho[\mathbf{N}^{(e)}]^{\mathrm{T}}\mathbf{f}_{\text{body}}d\Omega + \int_{\Gamma_1} [\mathbf{N}^{(e)}]^{\mathrm{T}}\bar{\mathbf{t}}d\Gamma \right\} \tag{2.28}$$

It is important to note that the external force vector, $[\mathbf{P}]$, accounts for both body forces and traction forces. In LS-Dyna, the external force vector also includes contact forces and hourglass forces acting on the nodes. Hourglassing is a phenomenon that occurs in finite element formulations that underutilize the number of

integration points in the Gauss-Quadrature scheme for computational efficiency. This can lead to the existence of zero-energy (also called hourglass) deformation modes with no stiffness. Hourglassing is briefly discussed in Section 2.3.1.3. For more information about contact and hourglass forces, the reader is referred to the LS-Dyna Theory Manual [62]. Rearrangement of Equation 2.25 leads to

$$\mathbf{a}_n = \mathbf{M}^{-1}(\mathbf{P}_n - \mathbf{F}_n) \tag{2.29}$$

where n denotes the instance in time. This shows that the sum of all internal and external forces acting on the discretized mass matrix can be used to determine the acceleration of all nodes in the system at the current instance of time. Using a numerical method, such as the central difference method, the displacement at the next instance of time can be determined and, thus, solve the transient behaviour of the system.

2.3.1.1   Explicit Time Integration

Explicit central-difference time integration is used to solve for the displacements as they change with time. Figure 2.15 presents a simplified schematic of the explicit time integration scheme for a single node. All known variables are highlighted in black, and all unknowns are highlighted in red. At the current instance of time, t_n, the current displacement, $\mathbf{u}_n$, is known. The history of the node, such as the velocity, $\mathbf{v}_{n-\frac{1}{2}}$, at time $t_{n-\frac{1}{2}}$, is also known. Lastly, the current acceleration is also known from the solution of Equation 2.29. At the next instances of time, the velocity at $\mathbf{v}_{n+\frac{1}{2}}$ and displacement at time $\mathbf{u}_{n+1}$, are unknown. Using the central difference method, the displacement at the next time step (black circles indicate time-steps) is approximated as

$$\mathbf{v}_{n+0.5} = \frac{\mathbf{u}_{n+1} - \mathbf{u}_{n-1}}{t_{n+1} - t_n} \quad \rightarrow \quad \mathbf{u}_{n+1} = \mathbf{u}_{n-1} + (t_{n+1} - t_n)\mathbf{v}_{n+0.5} \tag{2.30}$$

This requires the computation of the *intermediate* velocity at $\mathbf{v}_{n+\frac{1}{2}}$ to calculate the displacement at the next time step. This method is derived from a Taylor series expansion about $t_{n+0.5}$ and has a second-order truncation error. Thus, the displacement at the next time step, $\mathbf{u}_{n+1}$, is entirely determined by the velocity at the previous half-time step, $\mathbf{v}_{n-0.5}$, and the current acceleration. The displacement at the next time step is then used to calculate the next increments in stress and external forces, and thus, the acceleration at the next time step. This iteration process continues until the simulation finishes. Figure 2.16 presents a flowchart of the algorithm for each time step in the explicit dynamic FE formulation.
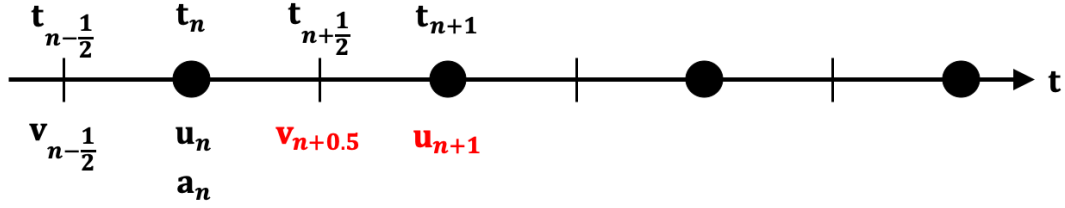
Figure 2.15: Timesteps in Explicit Time Integration Scheme (Beginning of New Timestep).
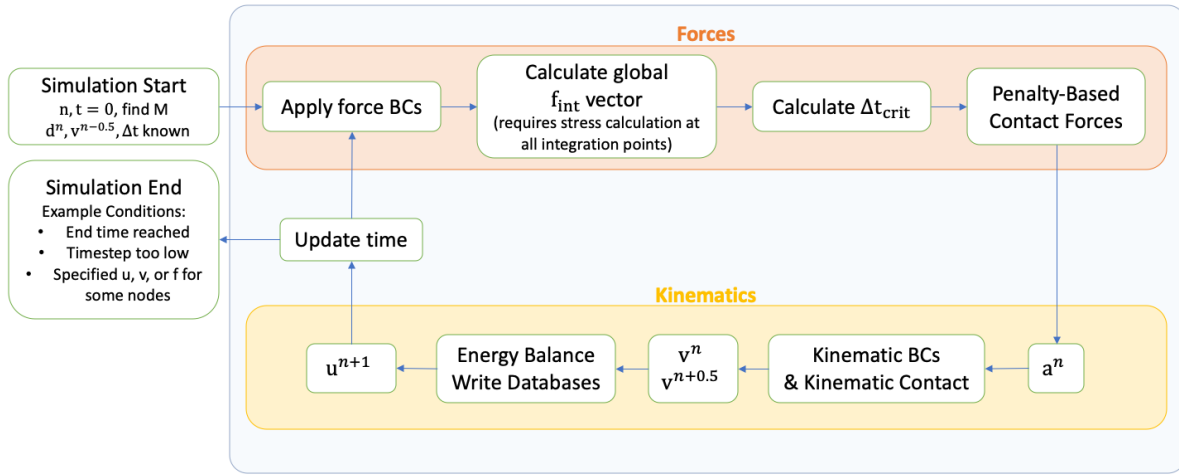
Figure 2.16: Flowchart of Explicit Dynamic FE Algorithm.

As mentioned above, this explicit method is an approximate solution for time integration. The truncation error introduces a critical time step that governs stability in the system. This critical time step is controlled by the Courant-Friedrichs-Lewy criterion determined by the speed of sound in a material and the element size [65]. It is worth noting that the critical time step is only a guideline, and does not guarantee the solution's stability. Other checks should be performed to ensure that instabilities are not present in the solution.

2.3.1.2   Energy Balance

Solution stability can be challenging to determine from simply analyzing the results of the FE simulation. For instance, Belytschko et al. [65] describes an "arrested instability" where some form of nonlinearity causes instability while the material is in the elastic region, causing the stress to diverge rapidly until yielding stabilizes the behaviour. This would lead to a large over-prediction of displacements without an incorrect final result. Such instabilities can be detected because any instability will cause energy to be spuriously generated. Therefore, it is useful to calculate the energy balance at each step, allowing stability to be checked. The associated equations are as follows:

$$W_{int/ext}^{n+1} = W_{int/ext}^n + 0.5\Delta\mathbf{u}\left(\mathbf{f}_{int/ext}^n + \mathbf{f}_{int/ext}^{n+1}\right) \tag{2.31}$$

22

$$W_{kin}^{n+1} = 0.5\mathbf{v}^{n+1}\mathbf{M}\mathbf{v}^{n+1} \tag{2.32}$$

$$\text{Conservation of Energy: } |W_{int} + W_{kin} - W_{ext}| < \epsilon \tag{2.33}$$

where ϵ is some small tolerance, ideally zero, generally on the order of 10^{-2}. If Equation 2.33 is not satisfied, it indicates the presence of instabilities in the solution.

2.3.1.3 Element Formulations

The role of the elements, as described above, is to provide interpolation of the solution between nodes. The topic of element formulations is briefly discussed in this section. For a complete discussion, the reader is referred to the textbook by Hughes [64]. In general, elements can be categorized by their dimensionality, which, in the context of this work, creates a distinction between what are known as *shell* elements and *solid* elements. Solid elements have a relatively simple formulation with the same number of dimensions as the problem. In this work, each solid element has a three-dimensional shape, and each node has three displacement degrees of freedom. Shell elements have a more complicated formulation, based on Reissner-Mindlin plate bending theory, which eliminates a physical dimension of the element but introduces additional degrees of freedom. These differences are illustrated in Figure 2.17. Instead of being directly represented, the thickness of the element is a parameter assigned to the element and used in the calculations performed by the element formulation.
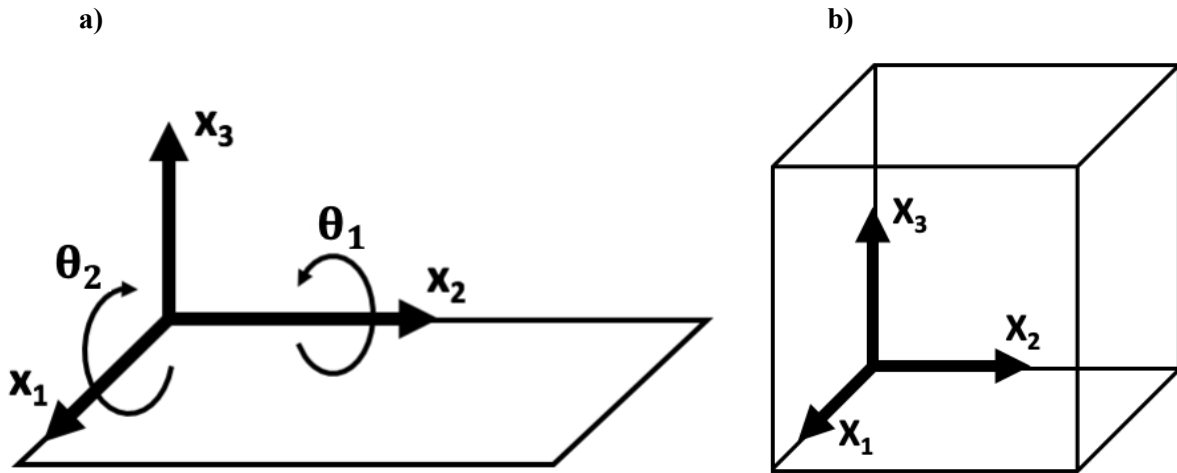
Figure 2.17: Element Shapes with Degrees of Freedom Indicated, a) Shell Element, b) Solid Element.

Element formulations are numerical approximations of the behaviour of a continuum, and as such, are susceptible to some numerical difficulties. In particular, *pressure locking, shear locking,* and *hourglassing* are FE behaviours of concern. A very brief overview of these phenomena will be presented below using the example of a four-node quadrilateral element. It should be noted that this is a 2D representation of a solid element and should not be confused with a shell element. It has a node at each

corner, each with two degrees of freedom. The stress and strain distribution are linear in each dimension. As described above, Gauss Quadrature is used to perform integration within the element. The quadrature scheme may either be fully-integrated where a 2x2 grid of points is used (Figure 2.18a), or under-integrated where the integral is evaluated using only a single point in the centre (Figure 2.18b).
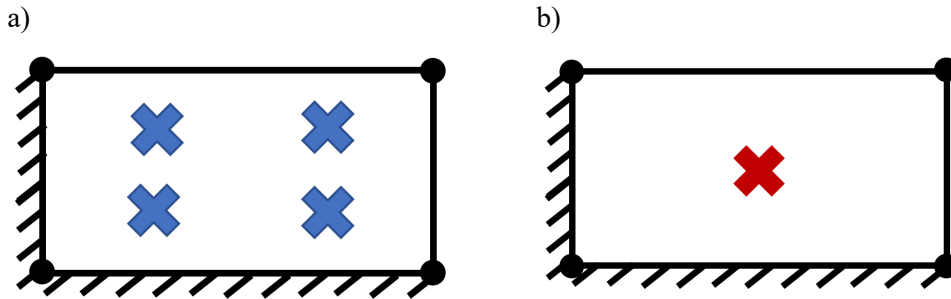
Figure 2.18: Quadrilateral Elements with a) Under-Integrated and b) Fully-Integrated Formulations.

Pressure locking occurs in incompressible materials and is also relevant for near-incompressible materials, such as metals undergoing large plastic deformations. Figure 2.18 gives examples of two elements, each with two edges fixed and one free node. Thus, these elements have two degrees of freedom, corresponding to the two degrees of freedom of the fixed node. There are four incompressibility constraints in the fully-integrated element (Figure 2.18a), one at each integration point, and the element is therefore over-constrained. To avoid this, *selectively reduced integration* is used, where the hydrostatic strain is evaluated with an under-integrated scheme (as in Figure 2.18b), and the deviatoric strain is evaluated with a fully-integrated scheme (as in Figure 2.18a). Thus, there is only one incompressibility constraint, and the element is not over-constrained. In many cases, *fully reduced integration* will be used, which only evaluates all strains at a single point. This is a popular formulation in explicit dynamics for its high calculation efficiency.

Shear locking occurs in bending problems. Figure 2.19 presents an application of pure bending using a 4-node quadrilateral element. Due to the limitations of the element formulation, the true boundary conditions (Figure 2.19a) collapse to simple forces applied at each node (Figure 2.19b). As a result, the classical elasticity solution – in which no shear strain is produced, and the element forms a curved shape (Figure 2.19c) – is not realized. Instead, the element deforms in a manner that generates large shear stresses in the material, seen at the integration points in Figure 2.19d. These shear strains make the element very stiff.

Hourglassing can take many forms in different elements, but the core problem is the same in all cases. When the stiffness matrix of the element is *rank-deficient*, i.e. when the number of stiffness terms is less than the number of degrees of freedom, there will be deformation modes that do not cause any stress

or strain to be raised in the element. Therefore, the element can deform in these modes indefinitely. In the case of the 4-node quadrilateral, the element as a whole has five degrees of freedom (two at each node, minus three rigid body modes). However, the stiffness matrix for the under-integrated formulation only has three terms, implying the existence of two zero-energy deformation modes. Figure 2.19c and Figure 2.19d highlight this – in the bending case, no strain is seen by the centre of the element, so this mode is zero-energy for an under-integrated formulation. The second zero-energy mode is the same as the first, simply in the other spatial dimension.

The poor performance of solid elements in bending problems, especially in applications with high thickness to width aspect ratios, motivated the development of shell elements. Shell element models perform well in bending applications with large element sizes, which allow for much quicker solution times. The disadvantage of shell elements is that they assume that the through-thickness strain is constant, the stress state is plane stress, the in-plane gradient of through-thickness displacement is small, and the rotations are small. Depending on how closely the actual physics of the problem meets these conditions, shell elements may or may not provide acceptable accuracy. More advanced shell element formulations are available, which allow for a linear through-thickness strain distribution to be part of the formulation. These formulations describe a 3D strain state and may be used with 3D constitutive models.
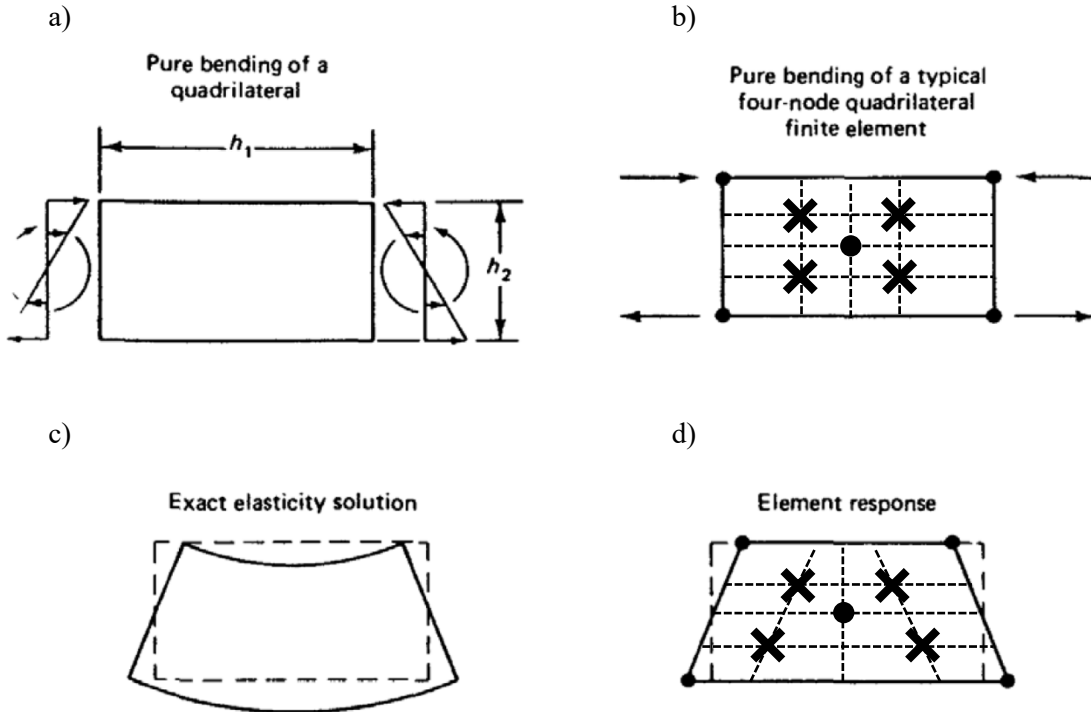
Figure 2.19: Pure Bending of a Quadrilateral Element, Adapted from Hughes [64].

2.3.2 Constitutive Modelling

This section presents an overview of the constitutive modelling approach used during nonlinear FE simulation of dynamic crush. A constitutive model is a set of mathematical equations that relates some properties of a material to the deformation. In the present solid mechanics application, the constitutive model determines the stress generated from applied deformations. The constitutive model receives deformation information in the form of a strain tensor, which in the finite element method is determined from the displacements by the element formulation. Within LS-Dyna, over 280 constitutive models exist to capture different material phenomena such as strain rate effects, failure criteria, equations of state, thermal effects, anisotropy, damage, and tension-compression asymmetry [66]. The development of new material models to capture different material phenomena is an ongoing field of research with many more material models to develop. Important active research areas in material modelling include: advanced material models for steel (e.g. [67]) and aluminum (e.g. [68]–[70]) based on crystal plasticity; measurement of anisotropic hardening (e.g. [71]); models of advanced materials such as carbon fibre composites (e.g. [72]) and magnesium (e.g. [73]); and advanced fracture models (e.g. [74]).

The kinematics of deformation are determined by the deformation gradient, $\mathbf{F}_n$, at an instance of time

$$\mathbf{F}_n = \frac{\partial \mathbf{x}(t)}{\partial \mathbf{X}} = \frac{\partial \mathbf{u}}{\partial \mathbf{X}} + \mathbf{I} \tag{2.34}$$

Note that the deformation gradient can be computed directly from the FE shape functions in Equation (2.23). The time derivative of the deformation gradient, $\dot{\mathbf{F}}_n$, can be calculated using a forward Euler scheme

$$\dot{\mathbf{F}}_n = \frac{\mathbf{F}_n + \mathbf{F}_{n-1}}{t_n - t_{n-1}} \tag{2.35}$$

and the velocity gradient, $\mathbf{L}_n$, as

$$\mathbf{L}_n = \dot{\mathbf{F}}_n \mathbf{F}_n^{-1} \tag{2.36}$$

The symmetric strain-rate tensor, $\mathbf{D}_n$, and anti-symmetric spin tensor, $\mathbf{W}_n$, can be calculated as

$$\mathbf{D}_n = \frac{1}{2}\left(\mathbf{L}_n + \mathbf{L}_n^{\mathrm{T}}\right) \ \ \text{and} \ \ \mathbf{W}_n = \frac{1}{2}\left(\mathbf{L}_n - \mathbf{L}_n^{\mathrm{T}}\right) \tag{2.37}$$

For small deformations with no rotations, the rate of stress can be related to the strain-rate tensor through Hooke's Isotropic Elasticity Law

$$\dot{\boldsymbol{\sigma}}_n^{\mathrm{J}} = \mathcal{L}^{\mathrm{el}} : \mathbf{D}_n \tag{2.38}$$

26

where $\dot{\boldsymbol{\sigma}}_n^J$ is the Jaumann rate of the Cauchy stress-rate tensor, and $\boldsymbol{\mathcal{L}}^{el}$ is the fourth-order elasticity tensor described in Voigt notation as

$$\boldsymbol{\mathcal{L}}^{el} = \frac{E}{(1+v)(1-2v)} \begin{bmatrix} 1-v & v & v & 0 & 0 & 0 \\ v & 1-v & v & 0 & 0 & 0 \\ v & v & 1-v & 0 & 0 & 0 \\ 0 & 0 & 0 & \dfrac{1-2v}{2} & 0 & 0 \\ 0 & 0 & 0 & 0 & \dfrac{1-2v}{2} & 0 \\ 0 & 0 & 0 & 0 & 0 & \dfrac{1-2v}{2} \end{bmatrix} \tag{2.39}$$

where E is the elastic modulus and v is Poisson's ratio. In this case, Hooke's Isotropic Elasticity Law is used to relate stress and strain. The Jaumann rate of stress is equal to the Cauchy rate of stress, $\dot{\boldsymbol{\sigma}}_n$ if there are no rotations. However, vehicle crashworthiness involves metal components that undergo large rotations. As such, an objective rate of stress that accounts for large rotations using a forward Euler scheme is calculated as

$$\dot{\boldsymbol{\sigma}}_n = \dot{\boldsymbol{\sigma}}_n^J + \mathbf{W}_n : \boldsymbol{\sigma}_{n-1} - \boldsymbol{\sigma}_{n-1} : \mathbf{W}_n \tag{2.40}$$

Beyond these large rotations, vehicle crashworthiness involves components that undergo severe plastic (permanent) deformations that require a constitutive model beyond Hooke's Isotropic Elasticity Law. Furthermore, manufacturing induced anisotropy in the material presents an additional challenge in accurate FE modelling of crashworthiness [25]. In the following section, the anisotropic elastic-plastic constitutive model is presented. The numerical implementation of this constitutive model follows the convex cutting plane algorithm presented in Chung and Richmond [75]. The reader is referred to the following literature for details about the numerical implementation of the elastic-plastic constitutive model into the finite element framework: Chung and Richmond [75], Yoon et al. [76], Abedrabbo et al. [77] and Kohar et al. [78].

2.3.2.1 The Elastic-Plastic Constitutive Model

The elastic-plastic constitutive model decomposes the total strain rate tensor into an elastic, $\mathbf{D}^*$, and plastic strain rate, $\mathbf{D}^P$, as

$$\mathbf{D} = \mathbf{D}^* + \mathbf{D}^P \tag{2.41}$$

Note that the time increment subscript has been removed for simplicity. Using Hooke's Elasticity tensor, the increase in stress rate is related to the elastic strain rate as

$$\dot{\boldsymbol{\sigma}}^{\mathrm{J}} = \mathcal{L}^{\mathrm{el}} : \mathbf{D}^* = \mathcal{L}^{\mathrm{el}} : (\mathbf{D} - \mathbf{D}^{\mathrm{P}}) \tag{2.42}$$

The direction of the plastic strain rate can be related to a plastic potential function, $g(\boldsymbol{\sigma})$, by a plastic multiplier, $\dot{\lambda}$, [79], [80]

$$\mathbf{D}^{\mathrm{P}} = \dot{\lambda} \frac{\partial g(\boldsymbol{\sigma})}{\partial \boldsymbol{\sigma}} \tag{2.43}$$

In the elastic-plastic model, plasticity is governed by the flow rule, Φ, defined as

$$\Phi = \sigma_{\mathrm{eq}}(\boldsymbol{\sigma}) - \overline{\sigma}(\overline{\varepsilon}^{\mathrm{P}}) \leq 0 \tag{2.44}$$

where $\overline{\varepsilon}^{\mathrm{P}}$ is defined as the effective plastic strain, $\sigma_{\mathrm{eq}}(\boldsymbol{\sigma})$ is called the yield function and relates the stress tensor to an equivalent stress, and $\overline{\sigma}(\overline{\varepsilon}^{\mathrm{P}})$ is called the flow stress and describes the work hardening behaviour of a material. From work conjugacy, the effective stress and plastic strain rate, $\dot{\overline{\varepsilon}}^{\mathrm{P}}$, can be related to the stress and plastic strain rate tensor [81]

$$\sigma_{\mathrm{eq}}(\boldsymbol{\sigma})\dot{\overline{\varepsilon}}^{\mathrm{P}} = \boldsymbol{\sigma} : \mathbf{D}^{\mathrm{P}} \tag{2.45}$$

Assuming that the plastic potential function is equivalent to the yield function (known as the associative flow rule assumption), the effective plastic strain rate is equivalent to the plastic multiplier ($\dot{\overline{\varepsilon}}^{\mathrm{P}} = \dot{\lambda}$). At any instance of time, the deformation is elastic and governed by Hooke's Isotropic Elasticity Law when $\Phi < 0$. However, the deformation is plastic when $\Phi = 0$ and constrained by $\sigma_{\mathrm{eq}}(\boldsymbol{\sigma}) = \overline{\sigma}(\overline{\varepsilon}^{\mathrm{P}})$. These constraints lead to the consistency equation ($\dot{\Phi} = 0$) that describes the rate of effective plastic strain, $\dot{\overline{\varepsilon}}^{\mathrm{P}}$. The application of the chain rule on the consistency criteria of Equation (2.44) leads to

$$\dot{\Phi} = \frac{\partial \sigma_{\mathrm{eq}}(\boldsymbol{\sigma})}{\partial \boldsymbol{\sigma}} : \dot{\boldsymbol{\sigma}}^{\mathrm{J}} - \frac{\partial \overline{\sigma}(\overline{\varepsilon}^{\mathrm{P}})}{\partial \dot{\overline{\varepsilon}}^{\mathrm{P}}} \dot{\overline{\varepsilon}}^{\mathrm{P}} = 0 \tag{2.46}$$

where $\partial \sigma_{\mathrm{eq}}(\boldsymbol{\sigma})/\partial \boldsymbol{\sigma} : \dot{\boldsymbol{\sigma}} = \partial \sigma_{\mathrm{eq}}(\boldsymbol{\sigma})/\partial \boldsymbol{\sigma} : \dot{\boldsymbol{\sigma}}^{\mathrm{J}}$. Substitution of Equation (2.42) into (2.46) and rearrangement for $\dot{\overline{\varepsilon}}^{\mathrm{P}}$ gives

$$\dot{\overline{\varepsilon}}^{\mathrm{P}} = \frac{\dfrac{\partial \sigma_{\mathrm{eq}}(\boldsymbol{\sigma})}{\partial \boldsymbol{\sigma}} : \mathcal{L}^{\mathrm{el}} : \mathbf{D}}{\dfrac{\partial \sigma_{\mathrm{eq}}(\boldsymbol{\sigma})}{\partial \boldsymbol{\sigma}} : \mathcal{L}^{\mathrm{el}} : \dfrac{\partial \sigma_{\mathrm{eq}}(\boldsymbol{\sigma})}{\partial \boldsymbol{\sigma}} + \dfrac{\partial \overline{\sigma}(\overline{\varepsilon}^{\mathrm{P}})}{\partial \dot{\overline{\varepsilon}}^{\mathrm{P}}}} \tag{2.47}$$

2.3.2.2 Yield Functions

The isotropic von Mises [82] yield criterion is a classical yield function that is used to determine the onset of plastic flow in solid mechanics. The yield function is given mathematically as

$$\sigma_{eq,vm}(\boldsymbol{\sigma}) = \sqrt{\frac{(\sigma_{11}-\sigma_{22})^2 + (\sigma_{22}-\sigma_{33})^2 + (\sigma_{33}-\sigma_{11})^2 + 6(\sigma_{12}+\sigma_{23}+\sigma_{32})^2}{2}} \tag{2.48}$$

This yield function is very simple, easy to implement, and computationally efficient. However, this yield criterion assumes isotropic deformation. Real-world materials may be anisotropic, where the yield strength in each direction is different. The Lankford coefficients (the ratio of plastic strains in different directions) may also vary [83]. Furthermore, the texture of the material may evolve under deformation, causing the material properties to change as the deformation progresses [70].

A variety of yield functions exist in the literature that can capture a variety of anisotropic behaviours (e.g. [84][85][86][87][88][89]). Recently, the Barlat et al. [90] yield function, known as the Yld2004-18p, has been shown to capture the anisotropic response of lightweight automotive alloys, such as aluminum, for crashworthiness applications [25]. As a result, the Yld2004-18p yield function is employed in this study. The Yld2004-18p yield function is a 3-dimensional symmetric formulation that uses two linear stress transformations tensors, $\mathbf{c}'$ and $\mathbf{c}''$, that operate on the deviatoric Cauchy stress tensor, $\mathbf{s}$, such that

$$\tilde{\mathbf{s}}' = \mathbf{c}':\mathbf{s} \quad \text{and} \quad \tilde{\mathbf{s}}'' = \mathbf{c}'':\mathbf{s} \tag{2.49}$$

where $\tilde{\mathbf{s}}'$ and $\tilde{\mathbf{s}}''$ are the first and second transformed deviatoric stress tensors respectively. The deviatoric Cauchy stress tensor is defined as $\mathbf{s} = \boldsymbol{\sigma} - \frac{1}{3}\text{trace}(\boldsymbol{\sigma})$. The first and second transformation tensors (in Voigt notation) are defined as

$$\mathbf{c}' = \begin{bmatrix} 0 & -c'_{12} & -c'_{13} & 0 & 0 & 0 \\ -c'_{21} & 0 & -c'_{23} & 0 & 0 & 0 \\ -c'_{31} & -c'_{32} & 0 & 0 & 0 & 0 \\ 0 & 0 & 0 & -c'_{44} & 0 & 0 \\ 0 & 0 & 0 & 0 & -c'_{55} & 0 \\ 0 & 0 & 0 & 0 & 0 & -c'_{66} \end{bmatrix} \quad \mathbf{c}'' = \begin{bmatrix} 0 & -c''_{12} & -c''_{13} & 0 & 0 & 0 \\ -c''_{21} & 0 & -c''_{23} & 0 & 0 & 0 \\ -c''_{31} & -c''_{32} & 0 & 0 & 0 & 0 \\ 0 & 0 & 0 & -c''_{44} & 0 & 0 \\ 0 & 0 & 0 & 0 & -c''_{55} & 0 \\ 0 & 0 & 0 & 0 & 0 & -c''_{66} \end{bmatrix} \tag{2.50}$$

where these 18 coefficients (c'_{ij} and c''_{ij}) define the yield function and are calibrated to experimental measurements of anisotropy. The equivalent stress function that is defined by the Yld2004-18p yield function is

$$\sigma_{eq,Yld2004-18p}(\boldsymbol{\sigma}) = \left(\frac{1}{4}\sum_{i=1}^{3}\sum_{j=1}^{3}\left|\tilde{S}'_i - \tilde{S}''_j\right|^m\right)^{\frac{1}{m}} \tag{2.51}$$

where $\tilde{S}'_i$ and $\tilde{S}''_i$ are the principal stress components of the first and second transformed deviatoric stress tensors, respectively. Experimental and crystallographic measurements suggest that values of $m = 6$ are appropriate for body-centred cubic materials, such as steel [91], and $m = 8$ for face-centred cubic [92] materials, such as aluminum. For materials that follow the normality rule, the yield surface must be convex [93]. Therefore, m must be greater than 1 in all cases. Note that the values $c'_{ij} = c''_{ij} = 1$ and $m = 2$ revert the Yld2004-18p yield function back to the isotropic von Mises yield function. The Yld2004-18p model is able to capture anisotropy of both Lankford coefficients and yield strength, but does not capture the effects of texture evolution.

2.3.2.3 Flow Stress

The flow stress model is used to represent the work hardening behaviour associated with the accumulation of dislocations in metals. A variety of hardening models exist in the literature [62]. This work utilizes the Voce hardening rule [94] for the flow stress model during quasi-static loading. The quasi-static flow stress, $\bar{\sigma}_0$ is defined as

$$\bar{\sigma}_0 = \sigma_{UTS} - (\sigma_{UTS} - \sigma_y)\exp(-D\bar{\varepsilon}^P) \tag{2.52}$$

where σ_y is the initial yield stress, σ_{UTS} is the ultimate tensile stress exhibited when the flow stress saturates, and D is a work hardening coefficient. Many metals used in the automotive industry exhibit rate-sensitive behaviour where the stress-strain response of the material is different depending on the strain rate (e.g. see refs [95]–[99]). A variety of models for capturing this effect within the classical plasticity framework exist, including the Johnson-Cook [100] and the Zerilli-Armstrong [101] rate-sensitivity models. These models incorporate an aspect of temperature sensitivity as well as rate effects; thus, these models require more calibration parameters and more experiments. This work will employ the Cowper-Symonds model for strain-rate sensitivity, which requires fewer experiments to calibrate because it does not consider temperature effects[53]. It defines a dynamic flow stress that is a scaled version of the "static" flow stress and normalized at some reference strain rate. The dynamic flow stress is calculated as

$$\bar{\sigma}(\bar{\varepsilon}^P) = \bar{\sigma}_d = \bar{\sigma}_0 \left(1 + \left(\frac{\dot{\varepsilon}}{M}\right)^{\frac{1}{q}}\right) \tag{2.53}$$

where M is the strain-rate sensitivity coefficient of the reference material and q is the strain-rate sensitivity exponent.

2.3.3 Application of Finite Element Methods to Crashworthiness

Since the proliferation of computational power in the late 1990s [57][91], scientists and engineers have turned to commercial FE software for modelling and designing axial crush structures (e.g. [103]–[105]). Otubushin [103] utilized a preliminary version of the LS-Dyna software, known as DYNA3D, to perform some of the first non-linear finite element simulations of the axial crushing experiments presented in Abramowicz and Jones [42]. The correlations between the simulations and experiments in the work of Otubushin are some of the earliest works that were used to validate the LS-Dyna software. Langseth et al. [104] performed one of the earliest comprehensive studies of crashworthiness that incorporated both experiments and FE simulations of aluminum structures. In their work, the effect of mass ratio and impact velocity on the crashworthiness response of aluminum extrusions was studied. Their FE model consisted of a square tube modelled with plane stress shell elements with quarter-symmetry to reduce computational requirements. Geometrical imperfections were used to trigger the crush folds. They used an isotropic von Mises yield function with the Voce flow stress model but no rate-sensitivity model. A simplified set of boundary conditions were applied to the nodes on one end of the tube, and a rigid body struck the other end of the tube with a prescribed constant velocity. Frictionless self-contact algorithms were applied to the tube. A reasonable agreement was found between the simulations and experiments, and although the exact force-displacement response showed some deviations, their FE model captured the general trends of the response. The total energy absorption predicted by the simulation showed good agreement with the measured experimental response (13% error or better), and the deformation modes appeared visually similar. Their parametric study showed that higher mean crush force correlated with increased impact speeds due to lateral inertia forces. Their results also showed that beyond a certain mass ratio (15:1), increasing the ratio of the impacting body mass to the tube mass had little effect on the crush response. The results of their numerical studies were further supported by the experimental studies of Karagiozova and Jones [106].

Han and Park [105] used FE analysis to perform parametric studies on square steel tubes under oblique loading. Figure 2.20 presents the FE model construction in their study. The modelling approach of Han and Park followed a similar approach outlined in Langseth et al. [104]; the FE model constructed by Han and Park [105] used shell elements with an isotropic von Mises elastic-plastic model without rate sensitivity. The entire geometry was modelled without symmetry with different boundary conditions to capture the off-axis loading condition. The striker mass was fixed to the end of the crush tube (shown as Area 2) and was constrained to move only in the initial direction of the tube axis.
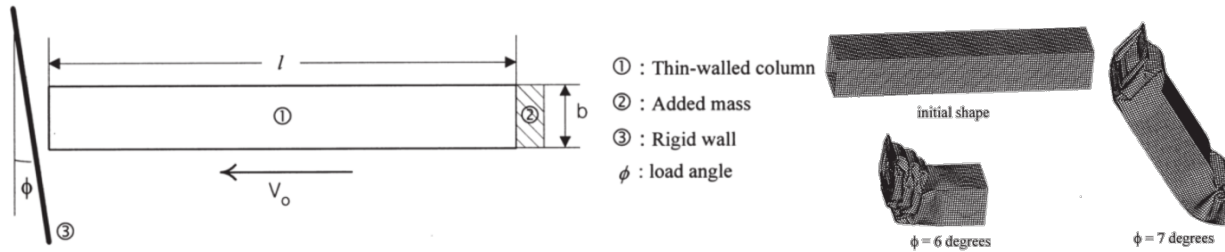
Figure 2.20: FE Model Setup for Oblique Loading and Selected Simulation Results [105].

Simulations were performed under different load angles. It was found that there was a critical load angle where the collapse mode would suddenly change from progressive buckling to a global buckling mode that would reduce the mean force by as much as 60%. It was found that changing the wall thickness had little effect on the value of this angle, but varying the rectangular aspect ratio had a significant effect.

Reyes et al. [34], [37], [38] performed numerical studies alongside their experimental studies of square aluminum tubes under quasi-static oblique loading. Figure 2.21 shows sample experimental and simulated results from these studies. The FE modelling approach followed a similar approach outlined in Langseth et al. [104]. Their FE models generally captured the correct deformation mode and mean crush force response but underestimated the post-buckling force response and overestimated the peak load unless initial imperfections were introduced to the FE model. This was the first major study to analyze oblique crush with experimental data provided for validation numerically and was a key source of oblique impact data available in the literature to validate computational models of oblique crush events (e.g. [5], [6], [107]).
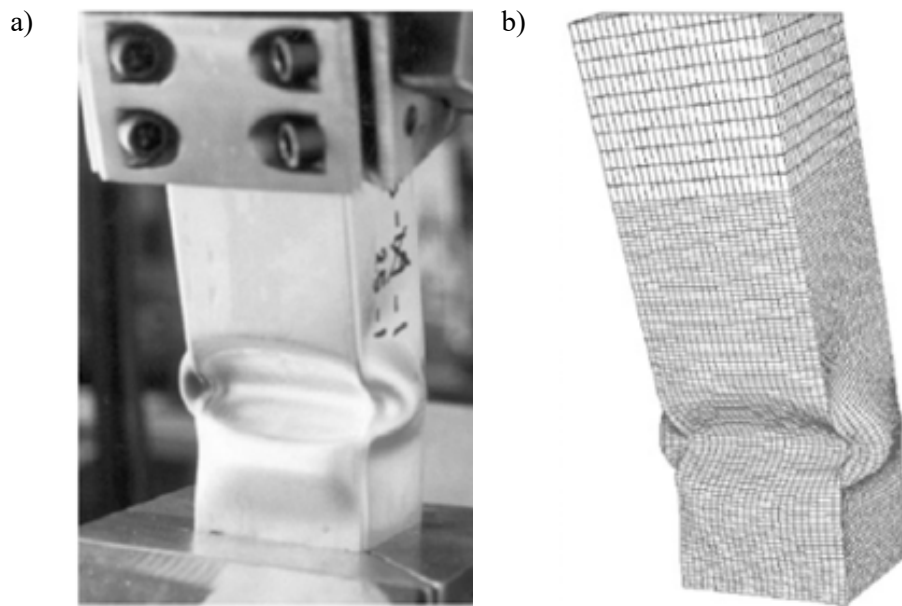
Figure 2.21: Quasi-Static Oblique Crush: a) Experimentally Crushed Tube, and b) FE Model [34].

Fyllingen et al. [108] investigated the difference between different element formulations, such as shell elements and solid elements. It was found that solid elements and a more advanced shell formulation that included a linear through-thickness strain distribution (*SECTION_SHELL TYPE=25 in LS-Dyna) were more accurate predicting the force-displacement response than traditional plane stress shell elements. In the case of solid elements, it was reported that using a mesh with only one element in the through-thickness direction was very inaccurate at predicting the force-displacement response. Refining the mesh to have two elements through-thickness was found to improve the prediction greatly. Further mesh refinement with more than two through-thickness elements showed quickly diminishing returns to improve accuracy at a great computational expense. Therefore, a mesh with two elements through-thickness is recommended when using solid elements. This result is further supported by the mesh refinement study performed by Kohar et al. [109].

Williams et al. [95] studied the influence of anisotropy on the axial crush response of hydroformed square aluminum tubes. Numerical simulations were performed with and without anisotropy and rate sensitivity using the Johnson-Cook model [100] and compared with experimental measurements. The Barlat et al. [88] Yld2000 yield function was used as the constitutive model to capture material anisotropy. Their results showed that including anisotropy lowered the predicted energy absorption. This occurred because the calibrated anisotropic yield surface had a smaller normalized area than the isotropic von Mises yield surface commonly used. Later, Giagmouris et al. [110] studied localization and failure in AA6061 during crush. Their results highlighted the importance of including 3-dimensional effects with a non-quadratic anisotropic yield function to obtain reasonable predictions of the onset of localization during crush.

Kohar et al. [109] performed a hybrid analytical-numerical study on the effects of the elastic-plastic response on the energy absorption of square crush tubes. Their work systematically studied the sensitivity of energy absorption characteristics to variations in the yield strength, ultimate tensile strength, hardening rate and failure strain. FE models were created using solid elements and shell elements, which highlighted the necessity for solid elements in predicting energy absorption (Figure 2.22). A simple fracture model was implemented in this work, which would delete elements if the effective plastic strain within them reached the failure strain of the material. It was found that increasing the yield strength will improve crush efficiency if the hardening capabilities are high enough but will otherwise decrease it.
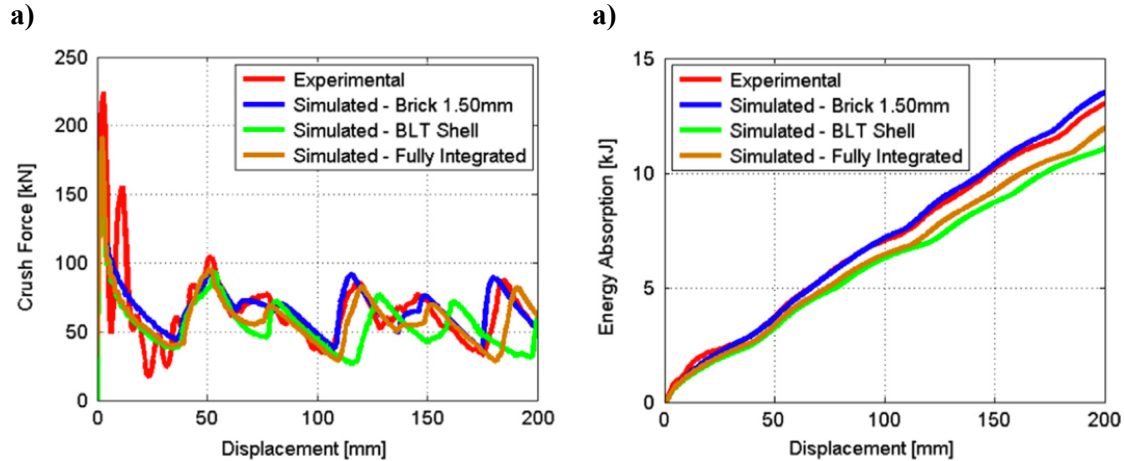
Figure 2.22: a) Force-Displacement and b) Energy Absorption Response Using Different Elements [109].

Another work by Kohar et al. [78] investigated the effects of yield function curvature and anisotropy on the crush response of circular aluminum tubes. The advanced CPB06ex2 [111] yield function was used in their study, capturing variations in yield stress, the direction of plastic flow, and tension/compression asymmetry. A detailed analysis was taken at various locations to study the critical strain paths during crush. It was generally found that the material begins in compression and moves through a state of shear towards plane strain bending combined with balanced biaxial stretching. It was shown that varying the shape of the yield surface had a significant effect on the stress and strain states of the material and the resulting response of the tube. The variation of yield stress anisotropy influences the crush forces, and the direction of plastic flow affected the deformation modes. It was also found that the energy absorption is very dependent on the area of the yield surface; this result was later echoed in a later study by the same authors [25].

Kohar et al. [25] also performed a study investigating the effect of the yield function choice on the outcome of an optimization study of a multi-cellular commercial crush rail design. Results from finite element models using both plane stress shell elements and 3-D solid elements are reported. The use of various yield surfaces (Von-Mises [82], Hosford [112], and Yld2004-18p [90]) is considered. It was found that the models utilizing solid elements with the Yld2004-18p yield function were the most accurate, and all 2-D formulations significantly under-predicted the energy absorption response. This was investigated using highly detailed finite element models that included contact with elastic steel bosses (clamps on the tube ends), plates, and the impacting sled. It was found that the SEA of the final design was up to 10% higher when using Yld2004-18p instead of Von-Mises, and up to 6% higher when using the generalized Hosford function. This work highlights the importance of using advanced yield functions when modelling and optimizing extruded crush tubes.

2.4   Design Optimization Principles

Optimization is the process of selecting the "best" option from a set of possible options. In structural design optimization, the set of options is called the *design space*, **q**, and each design has a variety of design parameters (e.g. thickness, material, etc.) that uniquely define a set. An *objective function* is used to define performance for each design, which mathematically expresses the criteria for selecting the "best" design. Typically, the goal of the optimization is to maximize or minimize the objective function.

A large variety of optimization methods exist, and the choice method depends on the type of problem. Various factors define the type of problem, such as:

- The number of objective functions to minimized/maximized;
- Degree of nonlinearity and convexity of each objective function;
- Cost in evaluating each objective function;
- Constraints on the design space (may be simple bounds on parameters or complex relations between parameters that must be satisfied);
- Sampling of the domain (Continuous data vs. discrete data).

There is typically no single optimum point in optimization problems that deal with multiple objectives (multi-objective optimization). Usually, objectives will conflict with each other to some degree, and there will be a set of optimal designs, representing the trade-offs between maximizing each objective independently. This set is referred to as a Pareto (optimal) front or non-dominated front. The Pareto front can be mathematically described as

$$f_i(\mathbf{q}^d) \geq f_i(\mathbf{q}^n) \quad i = 1{:}\,m \tag{2.54}$$

where $\mathbf{q}^d$ and $\mathbf{q}^n$ are two points in the design space, and *m* is the number of objectives, f. The design $\mathbf{q}^d$ is said to be "non-dominated" by $\mathbf{q}^n$ if at least one of the conditions in Equation 2.54 is satisfied, and $\mathbf{q}^d$ "dominates" $\mathbf{q}^n$ if all of the conditions in Equation 2.54 are satisfied [113]. The Pareto front is the set of designs that are non-dominated by all other points in the design space. Figure 2.23 presents an example for the design trade-off of the classical bending stiffness (flexural rigidity) of a structural beam. The geometry of the cross-section determines the flexural rigidity. As more material is added to the cross-sectional profile, the flexural rigidity will generally increase (desirable). Conversely, as material is removed, the flexural rigidity will decrease—however, less material results in lower mass, translating into lower cost (desirable). Therefore, there will be a Pareto front representing the trade-off between mass/cost savings (compared to the heaviest design) and high flexural rigidity. However, some cross-sectional shapes make more efficient

use of the additional mass than others. Thus, the most efficient designs will make up the Pareto front, and the remainder will be dominated.
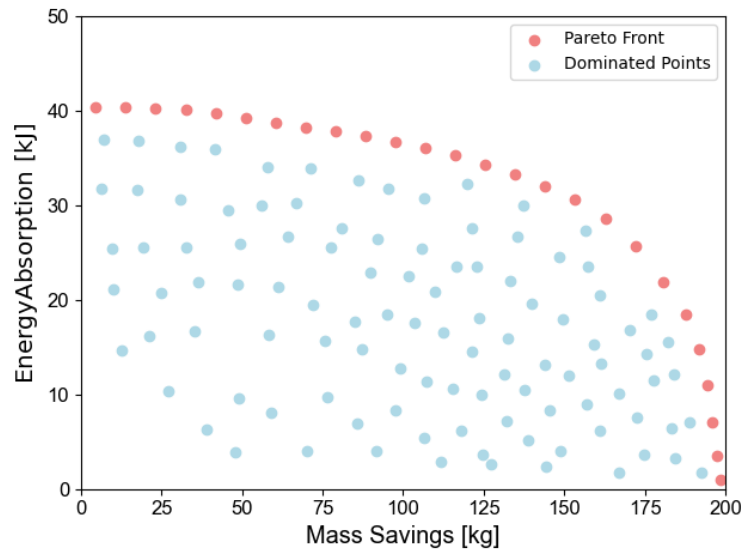
Figure 2.23: Example of a Pareto Front for a Simple Structural Problem.

Many multi-objective optimization techniques have been developed that aim to generate the entire Pareto front. These methods are often generalizations of single-objective optimization techniques and collapse to a single-objective method if only one objective is considered. In structural design applications that utilize multi-objective optimization, some subjective *preference* information is required to select a single point from the optimum set. Once a Pareto front is generated, a Multi-Criteria Decision Making (MCDM) technique may be used to select a single optimal point, such as the VIKOR technique, the Technique for the Order of Prioritisation by Similarity to Ideal Solution (TOPSIS), or a weighted average [114]. This may be established *a priori* (i.e., before the optimization is performed), *a posteriori* (i.e., after the Pareto front has been found), or with an interactive or hybrid technique [115]. A priori methods use *scalarization* to establish a single objective based on multiple objectives. An example of scalarization is to construct a single objective function using a weighted average of the objectives. The advantage of this approach is that single-objective optimization is often simpler and faster than multi-objective optimization. However, the benefit is limited, as only a single point on the Pareto front is found, and the decision-maker has no access to information about other non-dominated designs.

Most optimization algorithms rely on a large number of objective function evaluations when finding a global optimum. For many engineering problems, evaluating each function for every possible design within the design space is too computationally expensive. The response surface method for structural optimization proposed by Roux et al. [15] is an efficient strategy to overcome this challenge.

2.4.1 Traditional Response Surface Method

The response surface method(ology) (RSM) is based on the concept of optimizing a *metamodel* that is fast to evaluate instead of optimizing the objective function directly. The metamodel performs *regression analysis*, which takes existing data and maps the inputs and outputs. In structural optimization using the RSM approach, the design parameters and results from finite element simulations are used as the data for establishing this input-output relationship. Once this metamodel is generated, it can then be extended to predict/interpolate the outputs for any inputs. Thus, only a limited number of points need to be evaluated directly, and then the optimization is performed on the metamodel. A simple flowchart for the Response Surface Method is shown in Figure 2.24. In the traditional RSM approach that is commonly used in literature for structural optimization ([6], [10], [17], [20], [116], [117]), the steps are as follows:

1. *Optimization Problem Definition*: Define the objectives, constraints, and design variables. The stopping criteria for the RSM and the sampling rate (number of new points sampled each iteration) must also be defined.

2. *Define Initial Domain of Interest (DOI)*: The bounds for each design variable dimension are defined. For a discrete problem, the step sizes in each dimension are defined as well.

3. *Sample Points in Domain*: Within the DOI, new sample points (according to the sampling rate) are selected. There are many methods for choosing new points, described below in Section 2.4.1.1.

4. *Evaluate Sampled Points*: FE analysis is performed for the new samples in the domain, and the values of the objective functions are determined.

5. *Calibrate Metamodel*: The results of the sample evaluations are used to calibrate the metamodel. The details of the calibration process depend on the metamodel choice, but it is typically a minimization process to determine the metamodel parameters that minimize the metamodel error.

6. *Check Metamodel Accuracy*: The iteration scheme terminates once the metamodel error is less than the defined tolerance, $\epsilon_{\text{tol}}^{\text{err}}$, for a prescribed number of consecutive iterations. If this criterion is not satisfied, the framework iterates again from Step 3.

7. *Optimize on Metamodel*: Once the iterative loop ends, due to the metamodel error criterion being satisfied, the implication is that the metamodel is sufficiently accurate to represent the objective functions in the DOI. Then, an optimizer is run on the metamodel function in order to identify the solution. Function optimization is a large field, with many methods available. A summary is given in Section 2.4.1.1.

8. *Compute the Pareto Front*: The optimizer returns the final Pareto front for the optimization problem.
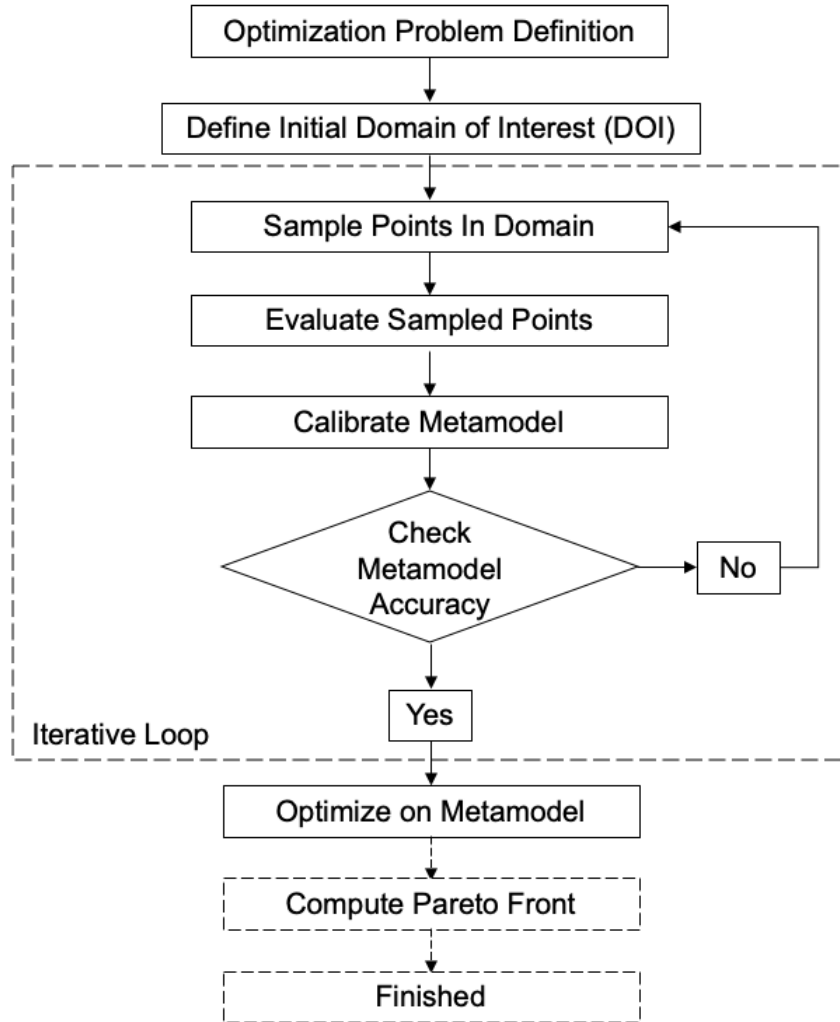
Figure 2.24: Flowchart of Traditional RSM.

The goal of the RSM approach is to use as few samples as possible while still being able to construct a metamodel that is accurate enough to capture the true optimum of the space. The results generated by the RSM approach are dependent on the sampling selection scheme, metamodelling technique, and optimization techniques. Details regarding the key elements and concepts of these three components of the RSM approach are discussed below in Sections 2.4.1.1 - 2.4.1.3.

2.4.1.1 Sample Selection Schemes

In each iteration of the RSM, several samples are selected from the design space for evaluation. Obtaining maximum coverage of the domain, known as *space-filling*, is a non-trivial problem with numerous available algorithms and methods. A simple approach is to perform random sampling from the space. A more methodical approach for relatively small problems is *factorial* sampling. In factorial sampling, a certain number of levels are assigned to each variable (e.g. two (2) levels in maximum and

minimum; three (3) levels in maximum, minimum, and median, etc.), and every combination is sampled. The number of samples generated is

$$\# \text{ of samples } = m^n \tag{2.55}$$

where m is the number of design variables, and n is the number of levels. However, for high dimensionality problems or greater resolution, the computational expense of a factorial approach is often prohibitive. This has motivated the development of many intelligent sampling approaches aiming to sample the design space as sparsely as possible while still acquiring sufficient information. Common methods include: Koshal [118], Latin Hypersquare [119], Taguchi [120], D-Optimal [118], and maximin/minimax [121]. These algorithms are powerful and flexible but have no built-in "guarantees". In contrast, a method such as LHS guarantees that each dimension of the space will be evenly sampled.

Table 2.1 presents a summary of the costs and benefits of each sampling scheme.

In Koshal sampling, the number of samples chosen is equal to the number of parameters of the regression model, such that it can uniquely identify each regression model parameter. This will require the fewest number of samples of any method but may be quite inaccurate due to the low sample density.

In the Latin Hypersquare (LHS) approach, the design space is divided into bins to create a grid representation. The number of bins for each design variable is equal to the number of samples. Then, samples are distributed such that each bin has exactly one sample [119]. This method provides good diversity of the sample space for the number of points sampled but is difficult to implement on discrete datasets which already have pre-set "bins" - which may be inconsistent across the dimensions of the space.

The Taguchi [120] method uses orthogonal arrays of sample points to create an efficient fraction of a full-factorial design. This offers an efficient alternative to full-factorial sampling but is inflexible in the number of samples a user may choose to select and may be less efficient than a LHS method, which allows for sparser sampling.

D-optimal [118] sampling selects the set of points that minimizes the generalized variance of the parameter estimates of the specified model, given a specified number of points to be sampled. Thus, it is metamodel-specific. Roux et al. [15] found that the D-optimal approach resulted in a lower maximum error and higher mean error than other sampling techniques, but that it is non-trivial to calculate which set is D-optimal, and usually it cannot be guaranteed that the optimal set has been selected.

The maximin and minimax algorithms are approaches that consider each new point one at a time with respect to all existing points and seek to either maximize the minimum distance between them or vice-

versa [121]. The algorithm selects one initial point that is either randomly chosen or seeded. At each iteration, the set of samples is chosen by adding points one at a time. For instance, in maximin sampling, each point added is chosen, such that it maximizes, $\Phi_{maximin}$, the minimum distance between the new sample point and any currently sampled point in the domain of interest

$$\Phi_{maximin}(X_n) = \min_{i \neq j} ||x_i - x_j|| \tag{2.56}$$

These algorithms are powerful and flexible but have no built-in "guarantees". In contrast, a method such as LHS guarantees that each dimension of the space will be evenly sampled.

Table 2.1: Comparison of Sampling Methods.

	Advantages	Disadvantages
Full Factorial	• Very dense sampling of the space • Acquires most information	• Very expensive • Often prohibitively with high domain dimensionality
Koshal	• Inexpensive • Simple to use	• Very sparse • Acquires limited information • Dependent on metamodel choice
Latin Hypersquare	• Diversity in sampling • Flexibility in the number of samples	• Difficult to use with discrete data (in particular for high density sampling)
Taguchi	• More efficient than factorial • Reasonably density in sampling	• Fixed number of samples • May be more expensive than methods that allow for sparser sampling
D-Optimal	• Minimizes the variance of the parameter estimates • Flexibility in the number of samples • Sampling from irregular domains	• Difficult to determine: requires optimization techniques to determine points, may not be able to guarantee D-optimality
Maximin/ minimax	• Spreads out samples with diversity (maximin pushes to boundaries more than minimax) • Allows for additional samples to be iteratively added while maintaining sample diversity • Flexibility in the number of samples • Sampling from irregular domains	• Does not guarantee even sampling across each dimension of the space (e.g. compared to Latin Hypersquare)

2.4.1.2 Metamodelling Techniques

As mentioned above, the RSM requires the use of a regression model to function as the metamodel. A regression model is a mathematical function that predicts the output response, $\tilde{\mathbf{y}}$, to a given input, $\mathbf{x}$. The operation of identifying the parameters in the regression model is known as training or fitting, which is a minimization exercise that reduces an error function between the predicted response of the regression model, $\tilde{\mathbf{y}}$, and the actual measurements, $\mathbf{y}$, for a given set of data, such that

$$Min(Error) = Min\big(f(\mathbf{y} - \tilde{\mathbf{y}})\big) \tag{2.57}$$

The regression model can then be used to predict the outputs of any inputs it is given. Typically, regression models perform best when interpolating but can be used for extrapolation.

Regression models often operate on multi-dimensional data that have various ranges in magnitudes of units. In the application of structural component design, the length of a crush rail can vary between the ranges 10^2 to 10^3mm, while the thickness of a wall section is confined to a range of 10^0mm. Furthermore, a mixture of units from different design properties (i.e., yield strength on the order of MPa, elastic modulus on the order of GPa, fracture strains that are unitless [mm/mm]) introduces an additional challenge of consistent units in defining an error metric. Utilizing different magnitudes and ranges of inputs and output values will often result in parameters with larger magnitudes dominating the error function, such that parameters with small magnitudes will fit poorly. In many regression models, their key element may have a desired functionality over a specific range of values (generally between a value of -1 to 1) and are not scale-invariant. Therefore, data normalization is typically performed prior to fitting or training, where the inputs and outputs where a linear mapping function is used. Common normalization operations are to map a parameter to a range of 0 to 1 using

$$\bar{\mathbf{x}} = \frac{\mathbf{x} - \min(\mathbf{x})}{\text{range}(\mathbf{x})}, \qquad \bar{\mathbf{x}} \in [0,1] \tag{2.58}$$

or to a range of -1 to 1 using

$$\bar{\mathbf{x}} = 2\left(\frac{\mathbf{x} - \min(\mathbf{x})}{\text{range}(\mathbf{x})}\right) - 1, \qquad \bar{\mathbf{x}} \in [-1,1] \tag{2.59}$$

The inverse mapping is then performed on the outputs of the regression model to convert them back to the original units/scale of the problem.

Various regression models can be employed in the RSM approach. Classical regression models used as metamodels include polynomial regression, kernel ridge regression, support vector regression, nonlinear regression, and feedforward neural networks. The following sections present a description of each method, technical insight and context for the choice of metamodel used in this work.

2.4.1.2.1 Polynomial Regression

The most fundamental regression model is polynomial regression through the least-squares method [122]. Polynomial regression fits a polynomial function to the available data by minimizing the MSE between the function predictions and the actual values of the data points [123]. The polynomial function is defined as

$$\tilde{y} = \boldsymbol{\beta}^{\mathsf{T}}\mathbf{x} \tag{2.60}$$

where $\mathbf{x} = [x^0, x^1, x^2, \dots x^m]$ are the inputs, $\boldsymbol{\beta} = [\beta_0, \beta_1, \beta_2, \dots \beta_m]$ are the parameters, m is the degree of the polynomial, and $\tilde{y}$ is the predicted output of the regression model. The goal is then to find the parameters of the function, $\tilde{\mathbf{y}}$, that minimize the error function, $\mathbf{E}$, with respect to the actual data, $\mathbf{y}$. The error is defined as

$$\mathbf{E} = (\mathbf{y} - \boldsymbol{\beta}\mathbf{X})^2 \tag{2.61}$$

By minimizing the error with respect to each parameter ($\partial\mathbf{E}/\partial\boldsymbol{\beta} = 0$), a closed-form solution with respect to the parameters is achieved, such that

$$\boldsymbol{\beta} = (\mathbf{X}^{\mathsf{T}}\mathbf{X})^{-1}\mathbf{X}^{\mathsf{T}}\mathbf{y} \tag{2.62}$$

Increasing the model complexity can reduce the regression model error. Although having zero regression model error is always desirable, increasing the model complexity to achieve lower error can result in a loss of the model's generalizability. Unless the data is exceptionally smooth, such a high level of accuracy often implies that the model has been fit not only to the general trends of the data but also to random noise and outliers. This is known as overfitting. This will severely impact the ability of the model to generalize to new data. Figure 2.25 demonstrates the concept of overfitting. In this example, a very high-order polynomial function (6th order) fits the data well compared to a lower-order polynomial function (2nd order). Even though the 6th order polynomial perfectly matches the input-output data, large oscillations and gradients are present within the interpolation region that may be undesirable or non-physical.
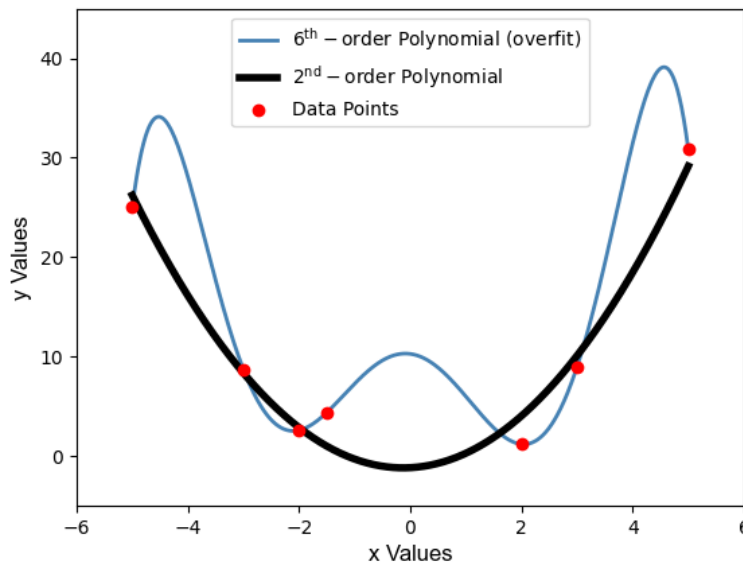
Figure 2.25: Example of Overfitting.

2.4.1.2.2 Kernel Ridge Regression

The simple polynomial model with a closed-form solution can perform very well for many engineering applications. However, it is possible that the parameters of the polynomial model $\boldsymbol{\beta}$ can become ill-conditioned such that very small changes to the input (i.e., machine error or rounding error) produces a very large change to the output. A regularization term may be added to the error function that better conditions the matrix to prevent this undesired effect. This is known as the ridge regression method [124], which has the following form for the error function

$$\mathbf{E} = \left|\left|\mathbf{y} - \boldsymbol{\beta}\mathbf{X}\right|\right|^2 + \Gamma\left|\left|\boldsymbol{\beta}\right|\right|^2 \tag{2.63}$$

where Γ is a regularization parameter that determines the strength of regularization. This addition to the error function will give preference to smaller coefficients, and the problem will be better conditioned. Following a similar methodology for minimization, the solution is given by

$$\boldsymbol{\beta} = \left(\mathbf{X}^T\mathbf{X} + \Gamma\mathbf{I}\right)^{-1}\mathbf{X}^T\mathbf{y}, \ \ \tilde{y} = \mathbf{x}^T\boldsymbol{\beta} \tag{2.64}$$

where $\mathbf{I}$ is an identity tensor. Although the above assumes a polynomial form, it can be extended to nonlinear functions by the "kernel trick", which maps the data through a kernel function into a linear space in which the linear regression method operates. The kernel can be any nonlinear function of form $k(x_1, x_2) = \Psi(x_1) \cdot \Psi(x_2)$, and is implemented by replacing every $\mathbf{x}$ in Equation 2.64 with $\Psi(x)$. This method is called Kernel Ridge Regression.

Kernel Ridge Regression and polynomial regression both have a closed-form solution. This is advantageous on small data sets, where the solution can be very quickly calculated without the need for an iterative method. However, on large data sets, the matrix inversion step required by this solution process can become very computationally expensive.

2.4.1.2.3 Nonlinear Regression

Regression in the style of the least-squares methods given above is also possible with arbitrary nonlinear functions, in the *nonlinear regression* method. The nonlinear function follows

$$\tilde{y} = f\left(\left[x_1, x_2, \ldots x_j\right], \left[\beta_1, \beta_2, \ldots \beta_k\right]\right) \tag{2.65}$$

In this method, any parameterization is allowed beyond the form given by Equation 2.60 above. Similar to the parameter identification for a polynomial regression, the nonlinear regression model parameters are determined through an error minimization exercise. However, no closed-form solution is available. Since the error function follows a nonlinear response, iterative solutions, such as the Gauss-Newton method, are

commonly employed optimizers used to identify the parameters [125]. The error function for nonlinear regression models is defined as

$$\mathbf{E} = (\mathbf{y} - \tilde{\mathbf{y}})^2 \tag{2.66}$$

The values of the coefficients, $\boldsymbol{\beta}^{(\alpha+1)}$, are determined iteratively according to

$$\boldsymbol{\beta}^{(\alpha+1)} = \boldsymbol{\beta}^{(\alpha)} - \left(\mathbf{J}^T\mathbf{J}\right)^{-1}\mathbf{J}^T\mathbf{E}^{(\alpha)}\boldsymbol{\beta}^{(\alpha)} \tag{2.67}$$

where α is the current iteration, and $\mathbf{J}$ is the Jacobian matrix of the residual error. The Jacobian matrix is defined by

$$J_{ij}^{(\alpha)} = \frac{\partial E_i^{(\alpha)}}{\partial \beta_j} \tag{2.68}$$

An initial guess $\boldsymbol{\beta}^{(0)}$ is required to begin the procedure. Nonlinear regression models allow a tailored mathematical model to capture individual mechanisms and phenomena that are observed directly. As a result, the formulations and parameters offer the most intuition about the system they are representing. However, this requires expert knowledge about the system. Furthermore, these nonlinear regression models can have multiple local optima that can make it challenging to identify a solution.

2.4.1.2.4 Regression with Neural Networks

More recently, neural networks have become an increasingly popular approach for solving nonlinear regression problems [126]–[129]. Neural networks are composed of many units, called neurons, which have inputs and outputs connected in a specified way to create the network. Each neuron uses a perceptron to process its inputs and determine the output value. Figure 2.26 shows a schematic of a multi-input perceptron. A perceptron takes the aggregate sum of each input, x_n, multiplied by a corresponding unique weighting factor, w_n, and applies an activation function, Φ, to get the final output value. In a vectorized form, the output of the perceptron is

$$\tilde{y} = \Phi\left(\mathbf{x}^T\mathbf{w}\right) \tag{2.69}$$

where Φ is an activation function. Common activation functions for a neuron include the logistic sigmoid, hyperbolic tangent (Tanh), rectified linear unit (Relu), and Softplus functions, shown in Figure 2.27. The Relu activation function follows the equation of a line when greater than 0; otherwise, the value is 0. However, using an exact value of zero for all negative x values causes the gradients to vanish [130]. Typically, the "leaky" formulation, which retains a slight slope when x is negative, is used to avoid this issue. The Softplus function is a smoother version of Relu to remove the discontinuity at x = 0.
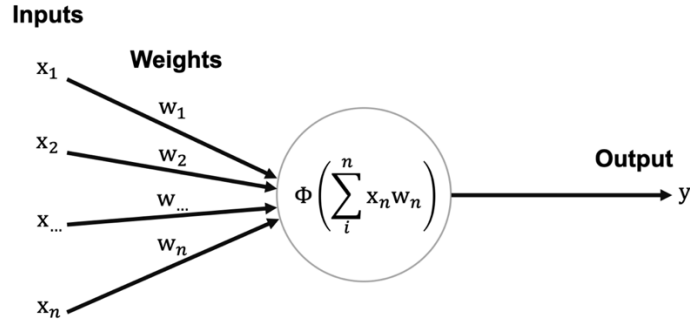
Figure 2.26: Schematic of a Multi-Input Perceptron.

Figure 2.28 illustrates a fully connected neural network with a single output. The output of neurons are connected as the inputs to additional neurons to form a hierarchal structure, known as a dense (hidden) layer. A neural network can contain any number of dense layers and number of neurons per layer. Furthermore, each neuron can have a unique activation function that is dependent on the application. These network architecture parameters are user-defined aspects of the neural network, and are known as hyperparameters. The flexibility of the network controls the degree of the nonlinearity that the model can capture. The architecture presented in Figure 2.28 is known as a feedforward neural network because the information from the input propagates forward to the output layer. In this architecture, each neuron of the current layer is connected to all outputs of the previous layer. This creates a complex function where the weights of the network are the parameters of the regression model.

A variety of optimization schemes exist to find the set of weights that minimizes the error of the model (called *loss* in the context of neural networks). There are three common error definitions: mean absolute error (MAE), mean squared error (MSE), and root mean squared error (RMSE), which are defined as

$$E = MAE = \frac{1}{N}\sum_i^N |y_i - \tilde{y}_i| \tag{2.70}$$

$$E = MSE = \frac{1}{N}\sum_i^N (y_i - \tilde{y}_i)^2 \tag{2.71}$$

$$E = RMSE = \sqrt{MSE} \tag{2.72}$$

where N is the number of samples. The values are always positive for all three error metrics, and a value of 0.0 is ideal. MSE and RMSE will proportionally penalize samples with higher errors more than MAE. RMSE will have the same units as the function values. However, RMSE introduces an additional

complexity by incorporating the square root operation for computing a gradient with respect to the function. MSE is typically used as the loss function in neural networks because it corresponds well to gaussian error distributions and has fewer complexities in calculation gradients.

a) **Logistic Sigmoid**   b) **Hyperbolic Tangent**

c) **Leaky Relu**   d) **Softplus**
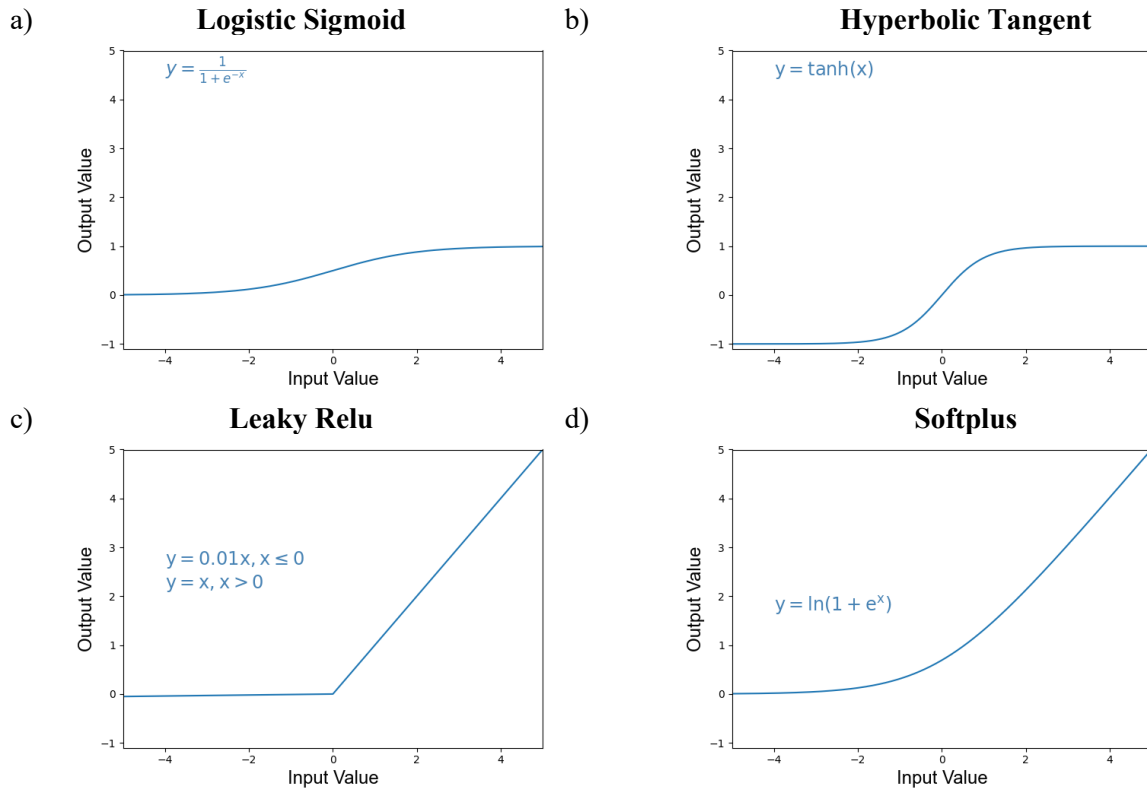
Figure 2.27: a) Logistic Sigmoid, b) Hyperbolic Tangent, c) Leaky Relu, and d) Softplus Neural Network Activation Functions.
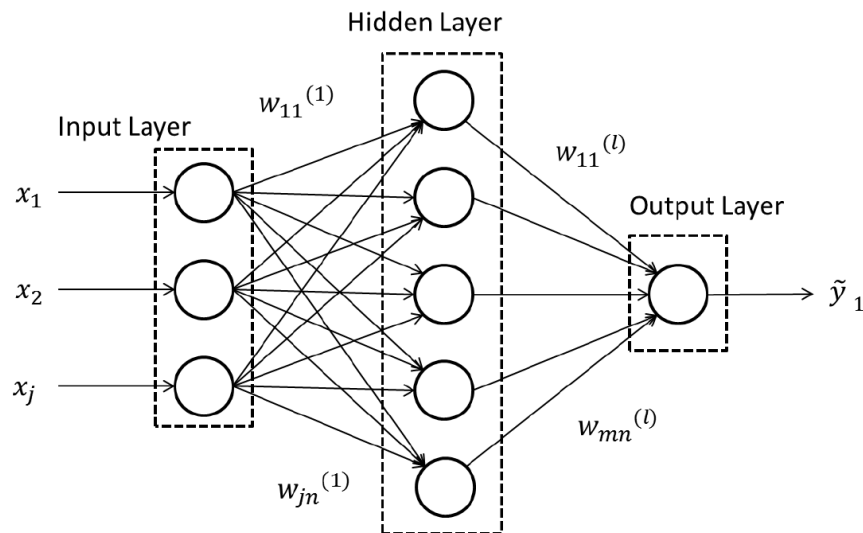
Figure 2.28: Fully Connected Neural Network [26].

Most optimization schemes for training neural networks are based on some form of the backpropagation algorithm first proposed by Rumelhart et al. [131]. The backpropagation algorithm updates the weights in the output layer by computing

$$w_{jk}^{(l)(\alpha+1)} = w_{jk}^{(l)(\alpha)} - N \frac{\partial E}{\partial w_{jk}^{(l)}} \tag{2.73}$$

where α is the current iteration (called an epoch), and N is the learning rate. $\partial E / \partial w_{jk}^{(l)}$ is the gradient of the error with respect to each weight, which is computed through a series of chain rules. Similarly, the change in the weights in any previous hidden layer is also dependent on the gradient of the error of the current layer. The gradients of the error can be evaluated and propagated to the previous layer for computation through additional chain rules.

For small networks, a quasi-newton gradient descent method, such as the L-BFGS algorithm described below in Section 2.4.1.3.1, may be used to optimize the network weights. The *stochastic gradient descent* (SGD) method, or a variation of it, is typically used for larger networks. SGD calculates the gradient using only a randomly sampled set of points in the training data rather than the entire set. This produces an approximate gradient and requires much less computational power and memory. A new random set is sampled for each calculation. More sophisticated methods are also commonly used, such as the Rmsprop [132] algorithm, which divides the gradient by a running average of its current magnitudes, or the Adam [133] method, which adds momentum to Rmsprop. A disadvantage of the backpropagation method is that the weights will change very slowly if the gradients become very small. This is called the vanishing gradient problem and arises mostly in deep or recurrent neural networks, where multiple derivatives are multiplied together [134].

In parameter identification of neural networks, known as training, the dataset is typically divided into three subsets: training data, validation data, and test data. The chosen fractions are problem-dependent, but the majority of the data will often remain in the training set (usually 80-90% of the data). The iterative scheme of the network parameter identification is performed using only the training data. The validation data set error is also computed to serve as a check for overfitting, which is a common problem for neural networks due to their ability to capture very complex behaviour. If the network begins to overfit to the training data, the error on the validation data will begin to increase, signalling that training should be stopped. It should be reiterated that the error of the validation data set is not utilized in updating the weights in the neural network. Finally, the network is verified with the test data as a final check to ensure that the

model has good generalizability. The critical difference between the test and validation data set is the test set is never used at any point in the training process (i.e., identification of overtraining).

Neural networks can be susceptible to overfitting due to their inherent flexibility with weights and various network architectures. Many approaches have been developed to promote good generalizability and avoid overtraining neural networks. There are a variety of regularization schemes available for neural networks. A straightforward approach is to include the L2 norm of the weights in the cost function, which follows a similar approach as ridge regression, where a penalty is applied to large network weights in the error function. Overfitting may also be combated by adjusting the network architecture or data during training, such as with the dropout method [135] or k-fold validation [136].

2.4.1.2.5 Nonparametric Regression and Kriging

The regression methods discussed so far can all be classified as *parametric* methods. In all cases, the form of the model is determined ahead of time, with specific parameters that are varied to minimize the error of the model (e.g. the coefficients of a polynomial or weights of neural network). However, there is also a class of non-parametric methods, in which the model structure itself is created from the data. This can have the advantage of flexibility - able to learn the functionality of the data without any previous knowledge. However, because the data is used to calibrate the estimation and create the model structure, more data points need to be sampled. The Kriging method [137] is a nonparametric regression model commonly used for crashworthiness applications (e.g. [5], [9], [117], [138]). In Kriging, the model structure is created between the provided training points by interpolating with a Gaussian process with covariance values set by the interpolation of a kernel function. The Kriging approach aims to maximize the log-marginal-likelihood of the interpolation. Figure 2.29 illustrates the concept: the model is exactly fit at the data points and is modelled in-between as the mean of a statistical process.
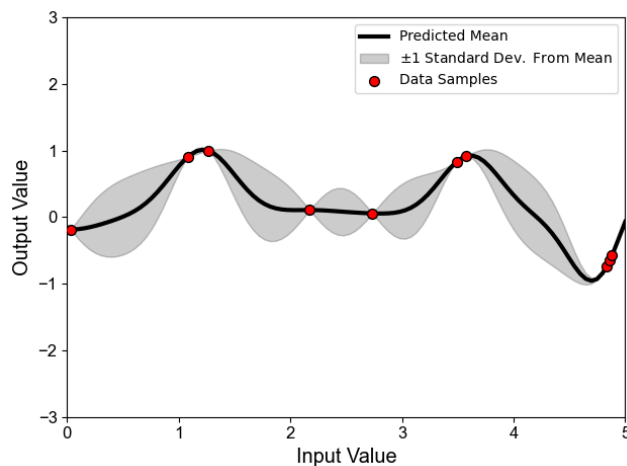
Figure 2.29: Example of a Kriging Model Fit to Data Points.

2.4.1.2.6 Comparison of Metamodel Techniques

A brief overview of the high-level advantages and disadvantages of the various metamodels is presented in Table 2.2. The main differences are the management and scalability of large data sets, the functionality of the model, and the number of hyperparameters. The neural network model shows good potential for capturing highly nonlinear and non-trivial relations, such as crash, if provided sufficient training information. However, the number of hyperparameters can be tremendous and significant effort may be required to design a good neural network model.

Table 2.2: Comparison of the Various Metamodelling Techniques.

	Advantages	Disadvantages
Polynomial Regression	• Closed form solution • Fast on small to medium data sets	• Slower on large data sets because of matrix inversion step • Limited functionality (i.e. only polynomial) • May suffer from ill-conditioned matrix
Kernel Ridge Regression	• Closed form solution • Fast on small to medium data sets	• Need to pick a kernel • Limited by kernel functionality
Nonlinear Regression	• Any analytical function may be used as the model • Model form and parameters provide the most intuition and meaning about the system	• Difficult to train: requires optimization scheme to find best parameters • Requires expert knowledge of system to formulate the model
Feedforward Neural Network	• Can capture very complex, even discontinuous behavior • Naturally identifies level of complexity required	• May be computationally expensive to train • Black box model • More difficult to implement: need to choose many parameters including network architecture
Kriging	• Non-parametric: does not assume any prior form for the functionality	• May require more sample points than parametric methods

2.4.1.3 Nonlinear Optimization Techniques

Nonlinear optimization methods are a class of numerical tools used to find the "best available" points in a nonlinear domain. They can be broadly classified into one of three categories:

- Algorithmic with finite termination
- Convergent iterative
- Heuristic

Algorithmic methods with finite termination are generally designed for solving a particular problem (i.e., finding the roots of a cubic function). For more general problems, convergent iterative and heuristic methods are the preferred choices for an optimizer.

Convergent iterative methods are methods that iterate towards a local solution until they have converged to a stationary point. They can be categorized by whether they require a Hessian evaluation, a gradient, or only the function values. These methods can be thought of as providing an "exact" solution, although they are limited to local optimization in the initial point neighbourhood. Convergent iterative methods converge to a single point and are therefore may not suitable for multi-objective optimization. Important methods in this class include gradient descent [139], Newton's method, and the BFGS (Broyden–Fletcher–Goldfarb–Shanno) algorithm [140].

Heuristic methods are procedures (also usually iterative) that have been experimentally found to solve optimization problems effectively. These procedures are often based on a set of rules and protocols that are found in nature. Heuristic methods make no assumptions about the functionality of the problem, and therefore, do not have the challenges associated with computing a gradient. Heuristic methods can be divided into two categories: *single-solution* or *population-based*. Single-solution methods, such as the Adaptive Simulated Annealing algorithm [141], consider only a single point and attempt to improve it as the optimization process progresses. Population-based methods consider a large group of points (referred to as *individuals*) at each step of the process. Important examples include differential evolution [142], Particle Swarm Optimization (PSO) [143], and Genetic Algorithms (GA) [144], all of which belong to a sub-category of population-based heuristics referred to as Evolutionary Computation. Population-based methods can search many regions of the problem domain at once and can converge to multiple points. This allows them to perform effective global and multi-objective optimization. However, convergence to a global optimum is not guaranteed. Additionally, heuristic methods can take much more time to converge than convergent iterative methods. Nevertheless, this has led to the adoption of heuristic methods - particularly genetic algorithms - in a wide variety of fields.

The following section presents a discussion on select convergent and heuristic-based optimization methods commonly employed in structural optimization applications.

2.4.1.3.1 Gradient Descent

Gradient descent [139] is a relatively simple convergent iteration scheme that aims to find the minimum value of f(x) by relying on the computation of the functions gradient. Given an initial guess x_0,

$$z_{n+1} = -\nabla f(x_n) \tag{2.74}$$

$$x_{n+1} = x_n + \gamma z_{n+1} \tag{2.75}$$

where z_{n+1} is the gradient of the $f(x_n)$ and γ is a step size. In each iteration, z_{n+1} points the function against the gradient towards the minimum, and the point x_n takes a step in this direction. Formulas are available to calculate upper bounds on γ to guarantee convergence [139]. Gradient descent will only find a minimum that is local to the initial guess. However, global optimization problems can be achieved by repeating the method with many random starting points. Gradient descent can become plagued with local minima convergence. Therefore, gradient descent can be augmented by the addition of *momentum* to Equation 2.74 [139] to help "push" the solution out of a local minimum through

$$z_{n+1} = -\nabla f(x_n) + p z_n, \quad p > 0 \tag{2.76}$$

where p is the momentum parameter and z_n is the previous computation of the gradient. With this addition, the direction in each step is influenced partly by the direction taken in the previous step. For many problems, particularly loss minimization in neural networks, the addition of momentum is found to improve significantly convergence speed [145].

2.4.1.3.2 Broyden–Fletcher–Goldfarb–Shanno) Algorithm

Newton's method [146] is a convergent iterative method that can be used to find the roots of the gradient if the Hessian (a matrix of second derivatives) can be computed. This finds a minimum or maximum point because these points have zero gradients. However, calculating the Hessian is often impractical. Therefore, a "quasi-Newton" method, which approximates the Hessian, is commonly used. A notable quasi-newton method is the BFGS algorithm for minimization, which approximates the Hessian using an iterative update that does not require matrix inversions. For a complete description of the BFGS algorithm, the reader is referred to Gill et al. [140]. The steps of the method are as follows:

1. Choose an initial guess for the optimal point, $\mathbf{x}^{(0)}$, and for the Hessian, $\mathbf{H}^{(0)}$. $\mathbf{H}^{(0)} = \mathbf{I}$ may be used in the absence of more information. A convergence parameter, ϵ, must be set, such as $\epsilon = 10^{-5}$. Set $k = 0$ and compute the gradient,

$$\mathbf{c}^{(0)} = \nabla f(\mathbf{x}^{(0)}) \tag{2.77}$$

2. Calculate the gradient norm, $||\mathbf{c}^{(k)}||$. If $||\mathbf{c}^{(k)}|| < \epsilon$, terminate and return $\mathbf{x}^{(k)}$.

3. Find the search direction, $\mathbf{d}^{(k)}$, by solving the system of equations

$$\mathbf{H}^{(k)}\mathbf{d}^{(k)} = -\mathbf{c}^{(k)} \tag{2.78}$$

4. Compute the step size, α, which minimizes $f(\mathbf{x}^{(k)} + \alpha \mathbf{d}^{(k)})$, by line search. In practice it is unnecessary to find the exact optimal α, merely one which satisfies the Wolfe conditions [147].

5.

6. Calculate the next point

$$\mathbf{x}^{(k+1)} = \mathbf{x}^{(k)} + \alpha \mathbf{d}^{(k)} \tag{2.79}$$

7. Update the Hessian approximation

$$\mathbf{H}^{(k+1)} = \mathbf{H}^k + \frac{\left(\mathbf{c}^{(k+1)} - \mathbf{c}^{(k)}\right)\left(\mathbf{c}^{(k+1)} - \mathbf{c}^{(k)}\right)^{\mathrm{T}}}{\left(\mathbf{c}^{(k+1)} - \mathbf{c}^{(k)}\right) \cdot \left(\alpha \mathbf{d}^{(k)}\right)} + \frac{\mathbf{c}^{(k)}\mathbf{c}^{(k)\,\mathrm{T}}}{\mathbf{c}^{(k)} \cdot \mathbf{d}^{(k)}} \tag{2.80}$$

8. Increment k and repeat from step 2.

BFGS is a powerful quasi-newton optimizer for finding local optima. However, it requires the storage of an $n \times n$ Hessian matrix in memory, resulting in a quadratic memory requirement (n is the number of problem variables). This can be prohibitive for large problems, such as the parameter identification in neural network training or implicit finite element calculations [65]. To address this, a limited-memory BFGS (L-BFGS) variation is often used instead of the base algorithm. L-BFGS does not store the entire Hessian matrix; Instead, L-BFGS stores a history of vectors with past m updates of the positions and gradients. L-BFGS uses these values to approximate the Hessian matrix,. As a result, it has only linear memory requirements, which allows for larger optimization problems to be solved [148]. Still, these convergent iterative methods can have difficulties overcoming problems that multiple local minima. Furthermore, these approaches assumed that a gradient (or a Hessian) could be computed. However, these convergent-based approaches can have difficulties with complex gradients that have discontinuities in their functionality.

2.4.1.3.3 Genetic Algorithms

Genetic algorithms (GA) are a population-based heuristic method that was developed to follow the "survival of the fittest" type methodology that was inspired by evolution in nature [149]. Typically, the first step of the genetic algorithm approach is to encode each sample as a collection of *chromosomes* – one per parameter – which are each represented by a discrete bit string. Figure 2.30 presents an example of three design parameters (A, B, C) that use binary encoding for a value 0 to 31. Each parameter requires 5 bits to ensure the entire range of values can be covered. The set of *chromosomes* defines the *genes* of an *individual* (i.e., set of design parameters). The performance of the individual is defined by their measure of *fitness*. Fitness is the optimization objective function to be maximized/minimized.

	Actual Value	2^4	2^3	2^2	2^1	2^0	Fitness
A	3	0	0	0	1	1	
B	17	1	0	0	0	1	85
C	21	1	0	1	0	1	

Figure 2.30: Binary Bit String Representation of a Sample for Genetic Algorithm.

Genetic algorithms use operations called *crossover* and *mutation* to "breed" new individuals from an existing set. This creates a new "generation" of individuals, from which the best members are chosen. In crossover, a random location along the length of a chromosome is picked, and values in chromosomes between two individuals are "crossed over" at that point, as shown in Figure 2.31. This is intended to represent the "mating" of *parents* to produce *offspring*. There are extensions of this concept, such as crossing over at multiple points. Most commonly, two random locations will be picked, and the bits in between will be swapped [150]. Mutation is simply when a random bit is flipped for a particular chromosome. This mutation has the potential to introduce a new diverse gene throughout the population that could provide better offspring.
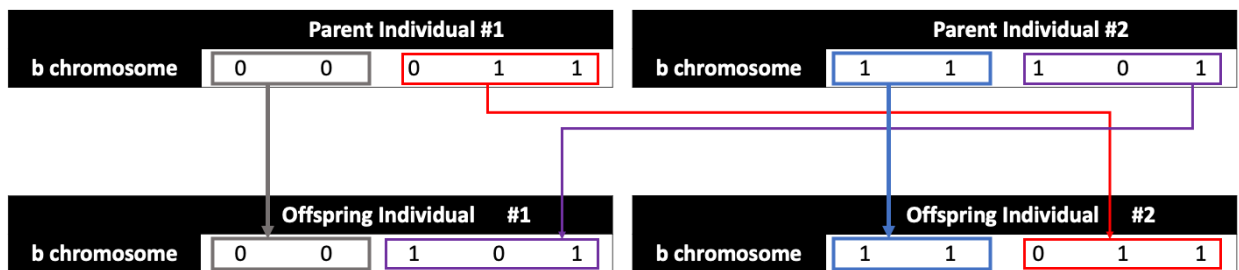
Figure 2.31: Example of Single-Point Crossover in a Genetic Algorithm.

The genetic algorithm process of iteratively creating generations is as follows [151]:

1. A population of length N is established and evaluated (the first generation) and the optimal solution is recorded.
2. Selection is performed on the existing (parent) population to make a new population with length N.
3. Crossover and mutation are performed on the new population to create a new (offspring) population.
4. The offspring and parent populations are combined and the N best individuals are taken, forming the next generation's parent population.
5. Stopping criteria are checked, and if not satisfied, the process repeats from Step 2.

The selection in Step 2 can be handled in several ways. The two most common are *roulette* and *tournament* selection. In roulette selection [152], the total fitness of the population is found by summing the fitnesses of all the individuals. Each individual's chance of being selected is equal to its fitness divided by the total population fitness. This can be thought of as the size of a wedge on a roulette wheel where a larger wedge has a higher probability of being selected. In tournament selection [153], a specified number of individuals is randomly chosen from the population. Only the individual with the highest fitness is chosen to be added to the next population. This would then be repeated until the population set is complete.

Techniques for using genetic algorithms without the need for binary encoding have also been developed, such as the simulated binary crossover (SBX) and polynomial mutation presented by Deb et al. [154]. Critically, when using these real-encoded methods, *distribution indices*, η_c and η_m must be defined for the crossover and mutation, respectively. The polynomial mutation process will be briefly discussed to illustrate the effect of these parameters. In this example, x is a parameter to be mutated. The lower and upper bounds of $x_L = 0$ and $x_H = 100$, and an initial value of $x_0 = 35$. The mutated value is calculated as follows:

1. Calculate the normalized distance to the edges of the domain:

$$\Delta_1 = \frac{x_0 - x_L}{x_H - x_L}, \qquad \Delta_2 = \frac{x_H - x_0}{x_H - x_L} \tag{2.81}$$

2. Flip a coin (random 1 or 0) between mutating upwards or downwards. Then, let r be a random number between 0 and 1.

$$\text{If downward:} \quad \Delta_q = \left(r + (1-r)(1-\Delta_1)^{1+\eta}\right)^{\frac{1}{\eta+1}} - 1 \tag{2.82}$$

$$\text{If upwards:} \quad \Delta_q = 1 - \left(1 - r + r(1-\Delta_2)^{1+\eta}\right)^{\frac{1}{\eta+1}} \tag{2.83}$$

3. Unnormalize:

$$x^* = \Delta_q * (x_H - x_L) \tag{2.84}$$

4. Bring inside domain, if outside:

$$x_1 = \min(\max(x^*, x_L), x_H) \tag{2.85}$$

Figure 2.32 shows the distribution of the mutated value for different values of η_m. For each value of η_m, the x_1 values corresponding to $r = [0, 0.01, 0.02 \dots 1]$ were plotted.
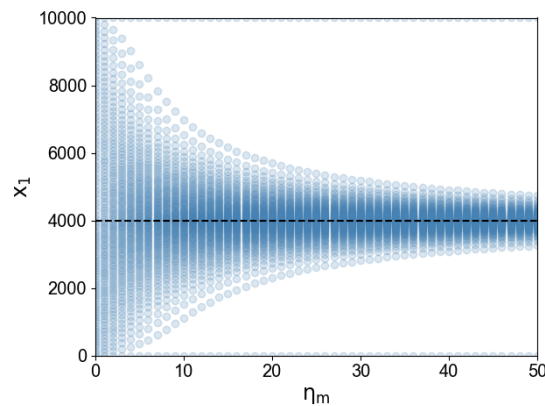
Figure 2.32: Distribution of Mutated Value for Different Distribution Indices in Polynomial Mutation.

2.4.1.3.4 Multi-Objective Genetic Optimization with NSGA-II

The genetic algorithm approach can be extended to solve multi-objective problems. Various multi-objective genetic algorithm techniques have been developed, such as the Pareto Archived Evolution Strategy (PAES) [155], Strength-Pareto Evolutionary Algorithm [156], and the Non-dominated Sorting Genetic Algorithm (NSGA-II) developed by Deb et al. [157]. Deb et al. [157] showed that NSGA-II outperforms PAES and the Strength-Pareto Evolutionary Algorithm across various difficult problems. With this in mind, a description of the NSGA-II algorithm is given here.

The key contributions of NSGA-II are the introduction of a fast non-dominated sorting algorithm, the use of a "crowding distance" metric, a fast algorithm for calculating it, and the introduction of a "crowded-comparison" operator that uses both non-domination and crowding distance to rank designs. The non-dominated sorting algorithm assigns a "front rank" to each design, such that designs that are non-dominated by any other design have a rank of one, the designs which are non-dominated by any other design except the rank-one designs have a rank of two, etc. The crowding distance for a particular point estimates the perimeter of the hyper-cuboid formed by using the nearest neighbours (in the space of the objective functions) as vertices. Thus, it measures the density of the populated solution space around that point. The crowded-comparison operator combines the front rank and crowding distance into one metric defined as:

$$\mathbf{q}^d \prec \mathbf{q}^n \quad \text{if} \quad \mathbf{q}^n_{\text{rank}} < \mathbf{q}^d_{\text{rank}} \ \text{OR} \ \left(\mathbf{q}^n_{\text{rank}} = \mathbf{q}^d_{\text{rank}} \ \text{AND} \ \mathbf{q}^d_{\text{distance}} > \ \mathbf{q}^n_{\text{distance}}\right) \qquad (2.86)$$

It is a two-level sort; first on the front rank of non-dominance, then on crowding distance, and preferring less-crowded designs.

The actual optimization process follows the same five steps as presented above for single-objective GA, with two modifications:

   i.   In Step 2, the crowded-comparison operator is used to compare designs (Deb et al. [157] use a binary tournament for their selection),

  ii.   In Step 4, the N "best" designs are determined by ranking with the crowded-comparison operator.

2.4.1.3.5 Comparison of Optimization Techniques

A brief overview of the advantages and disadvantages of the optimization strategies is presented here. The critical difference is that L-BFGS (and other iterative methods) are local optimizers and require a function gradient, whereas GA can perform global optimization and multi-objective optimization and only requires function values. Thus, convergent iterative methods will give a poor result for many optimization problems, and a heuristic method such as GA should be used. However, in optimization problems where the drawbacks of convergent iterative methods are not significant, methods such as L-

BFGS provide very fast convergence to an "exact" solution and will usually vastly outperform heuristic methods.

Table 2.3: Comparison of Optimization Techniques.

	Advantages	Disadvantages
L-BFGS (iterative)	• Fast convergence • Converges to a stationary optimal	• Local optimization • Scales poorly to large data sets • Requires function gradient • Single-objective only
GA (heuristic)	• Global optimization • Natural to implement for discrete data • Easily extended to multi-objective optimization • Only uses function values (no gradients)	• "Exact" convergence is not guaranteed • Requires adaptation to work with real-valued data

2.4.2 Advanced RSM Approaches

The traditional RSM approach iteratively samples the design space, fits the metamodel to the samples, and repeats this process until the metamodel achieves sufficient accuracy. As more samples are added to the process, the metamodel error will eventually converge to an average error value. Once converged to an average error value, additional sampling may not add meaningful improvements to the average predictability of the metamodel. As such, the iterative approach can be more efficient than initially sampling the entire domain with a high sample density. The iterative RSM approach is also more efficient than directly optimizing on the design space without a metamodel [23], [118], [158] . However, the iterative process does not use information from previous iterations, either about the metamodel or about the current optimal solution, to guide subsequent iterations. This represents a significant inefficiency in the traditional RSM that more intelligent RSM approaches can exploit. There are two main approaches for enhancing the traditional RSM: using metamodel information and using optimization information in intelligent iteration schemes.

Enhanced RSM approaches that utilize metamodel information typically evaluate the metamodel performance (i.e., error) in different regions of the design space. A survey of various metamodel-based enhancements is presented in Allmendinger et al. [159]. The key idea is that the low metamodel accuracy is attributed to relatively low sample density to capture the correct functionality of the metamodel. In subsequent iterations, samples are generated in the regions that most need additional accuracy. Without using the information about metamodel error in the design domain, the process will likely continue to

sample regions where the metamodel accuracy already has sufficient accuracy, adding little additional information.

However, the ultimate goal of structural optimization is to find an optimal solution. Although higher metamodel accuracy is desired, this can add additional samples in sub-optimal regions of objective performance. An alternative enhanced RSM approach is to perform the optimization operation on every iteration. This makes a critical assumption that the optimization operation has a relatively low computational cost compared to the metamodel fitting or data generation step. This approach uses the information about the current optimal solution to focus on the surrounding region of the optimum. The Successive Response Surface Methodology (Stander et al. [158]) and Adaptive Surrogate-Assisted Response Surface Methodology (ASA-RSM) (Stander 2013 [23]) methods utilize this approach for single-objective and multi-objective optimization problems, respectively. It should be noted that the multi-objective ASA-RSM approach degenerates to the single-objective SRSM approach for optimization problems with a single objective function. The ASA-RSM approach is discussed in the following section.

2.4.2.1   Adaptive Surrogate-Assisted RSM

The flowchart of the ASA-RSM is shown in Figure 2.33. It follows a very similar process path as the traditional RSM (Figure 2.24). However, the ASA-RSM approach includes information about the optimal solution in the stopping criteria. More importantly, the ASA-RSM includes domain reduction around a domain of interest (DOI) to narrow the search to the region around the Pareto front. This is performed with a Pareto Domain Reduction (PDR) scheme that is further described in Section 2.4.2.1.1. The differences between the ASA-RSM and the traditional RSM are:

- **Sampling Points in Domain:** In ASA-RSM, new samples are only selected within the current DOI.
- **Calibrate Metamodel:** All points within the global domain are used to calibrate the metamodel.
- **Optimize on Metamodel/Compute Pareto front:** In ASA-RSM, optimization is done at the end of each iteration. This happens inside the iterative loop and is performed before evaluating termination conditions. Optimization is still performed on the entire domain if the metamodel guides the solution into a region outside of the previous optimum.
- **Evaluate stopping criteria:** The metamodel error criterion from the traditional RSM is used in ASA-RSM, but it is paired (through an AND operation) to convergence the optimal set. This has the key advantage of preventing the process from terminating when the metamodel has converged while the optimal set is still converging and vice-versa. The change in the optimal set between one iteration and the next is calculated as a normalized distance between Pareto fronts and compared to a threshold

$$d_{k \leftrightarrow k+1} = \frac{\sum_{i=1}^{n(\mathbb{Y}^k)} \min\left(\sqrt{\sum_j \left(\frac{\mathbb{Y}_{ij}^{k+1} - \mathbb{Y}_{ij}^k}{\overline{\overline{\mathbb{Y}}}_j}\right)^2}\right) + \sum_{i=1}^{n(\mathbb{Y}^{k+1})} \min\left(\sqrt{\sum_j \left(\frac{\mathbb{Y}_{ij}^{k+1} - \mathbb{Y}_{ij}^k}{\overline{\overline{\mathbb{Y}}}_j}\right)^2}\right)}{n(\mathbb{Y}^k) + n(\mathbb{Y}^{k+1})} \tag{2.87}$$

where $\mathbb{Y}_{ij}^k$ and $\mathbb{Y}_{ij}^{k+1}$ are the Pareto fronts with $n(\mathbb{Y}^k)$ and $n(\mathbb{Y}^{k+1})$ points from iteration k and $k+1$, respectively. Each distance is normalized by the range of the maximum and minimum values of each attribute $\overline{\overline{\mathbb{Y}}}_j = \max(\mathbb{Y}_j) - \min(\mathbb{Y}_j)$. The symmetric operation accounts for the different number of solutions for each Pareto front.

- **Update DOI Around Pareto Front:** The PDR scheme is used to update and shrink the DOI around the Pareto front in ASA-RSM.
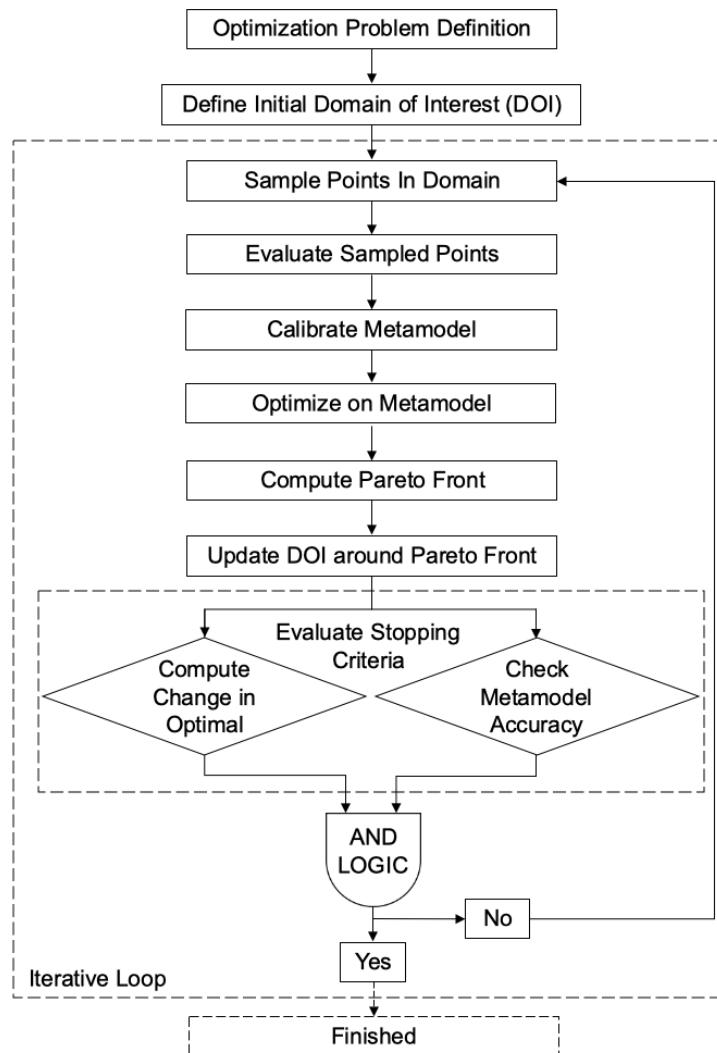
Figure 2.33: Flowchart of the Adaptive Surrogate-Assisted Response Surface Methodology.

2.4.2.1.1 Pareto Domain Reduction (PDR) Scheme

The PDR operates by selecting a set of kernel points from the current Pareto front and creating a domain around each one. The initial size of the domain is equal to the full range of the design variable values in each dimension. The union of these domains forms the DOI, which is approximately the optimal region of the design space. With each iteration, the subspace centers and reduces in size on each successive optimum front. Figure 2.35 presents a schematic of the PDR scheme. Three parameters control the rate of domain reduction: η that defines the zooming, γ_{pan} that controls panning, and γ_{osc} that controls the oscillation of the domain. A relaxation term, β, may be introduced as well.
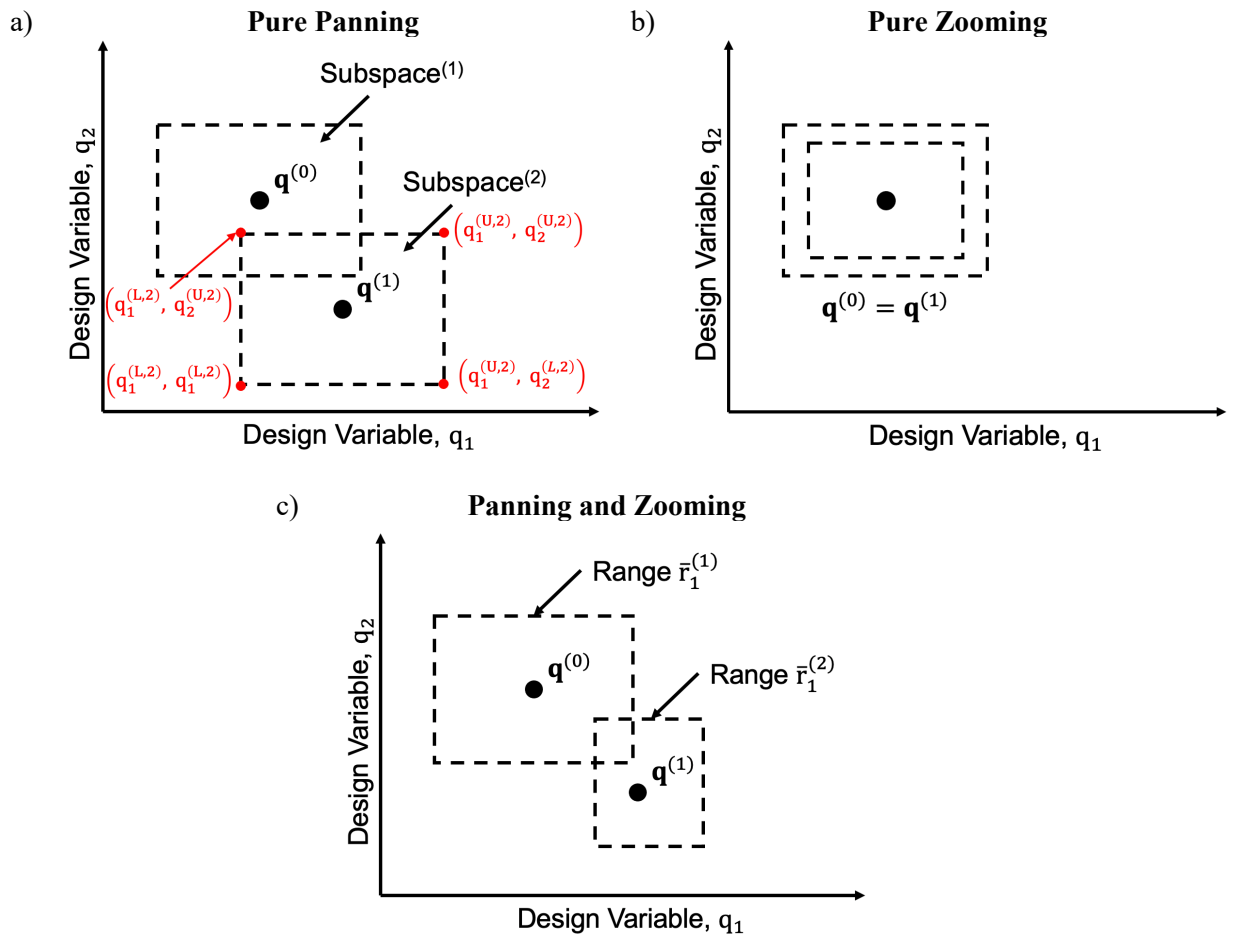
Figure 2.34: Subregion movements showing a) Pure Panning, b) Pure Zooming, and c) Panning and Zooming (adapted from Stander and Craig [158]).

The upper and lower bounds $\left(\mathbf{q}^{(U,k+1)}, \mathbf{q}^{(L,k+1)}\right)$ that govern the range $\bar{\mathbf{r}}^{(k+1)}$ of each design parameter $\mathbf{q}^{(k)}$ for the next Iteration $k+1$ are defined as

$$\mathbf{q}^{(U,k+1)} = \mathbf{q}^{(k)} + 0.5\bar{\mathbf{r}}^{(k+1)} \text{ and } \mathbf{q}^{(L,k+1)} = \mathbf{q}^{(k)} - 0.5\bar{\mathbf{r}}^{(k+1)} \tag{2.88}$$

The range $\bar{\mathbf{r}}^{(k+1)}$ uses the relaxation parameter, β, to control the rate of domain reduction, such that

$$\bar{\mathbf{r}}^{(k+1)} = \beta\mathbf{r}^{(k+1)} + (1-\beta)\mathbf{r}^{(k)} \tag{2.89}$$

where $\mathbf{r}^{(k)}$ is the range from the current iteration, and $\mathbf{r}^{(k+1)}$ is the instantaneous range. $\beta = 0$ corresponds to no change in the domain, while $\beta = 1$ utilizes the full magnitude of the reduction scheme. The parameter range dynamically changes with each iteration, such that

$$\mathbf{r}^{(k+1)} = \lambda^{(k)}\mathbf{r}^{(k)} \tag{2.90}$$

where $\lambda^{(k)}$ is the contraction rate of the design parameters. The contraction rate is defined as

$$\lambda^{(k)} = \eta + |\mathbf{d}^{(k)}|(\bar{\gamma}^{(k)} - \eta) \tag{2.91}$$

where η is a zooming constant, $\bar{\gamma}^{(k)}$ is the adaptive contraction parameter, and $\mathbf{d}^{(k)}$ is the direction of movement. For a single domain, the direction of movement is computed as the normalized difference between the location of the previous solution and the location of the current solution

$$\mathbf{d}^{(k)} = \frac{2\Delta\mathbf{q}^{(k)}}{\mathbf{r}^{(k)}}; \quad \Delta\mathbf{q}^{(k)} = \mathbf{q}^{(k)} - \mathbf{q}^{(k-1)}; \quad \mathbf{d}^{(k)} \in [-1; 1] \tag{2.92}$$

For the multi-objective form, the average position of all points on the Pareto front is used as the location of the solution. To account for oscillation about a region, an oscillation indicator $c_i^{(k)}$ is calculated from the directional movement at iteration k as

$$\mathbf{c}^{(k)} = \mathbf{d}^{(k)}\mathbf{d}^{(k-1)} \tag{2.93}$$

The oscillation indictor is normalized as $\hat{\mathbf{c}}^{(k)}$

$$\hat{\mathbf{c}}^{(k)} = \sqrt{|\mathbf{c}^{(k)}|}\,\text{sign}(\mathbf{c}^{(k)}) \tag{2.94}$$

Now, the current contraction parameter $\gamma_i^{(k)}$ is computed as

$$\gamma^{(k)} = \frac{1}{2}\gamma_{\text{pan}}(1 + \hat{\mathbf{c}}^{(k)}) + \frac{1}{2}\gamma_{\text{osc}}(1 - \hat{\mathbf{c}}^{(k)}) \tag{2.95}$$

where γ_{pan} represents the panning case, and γ_{osc} represents shrinkage to dampen oscillations. For a purely oscillating case, the contraction parameter will equal γ_{osc}, and for a purely panning case, the contraction parameter will equal γ_{pan}.
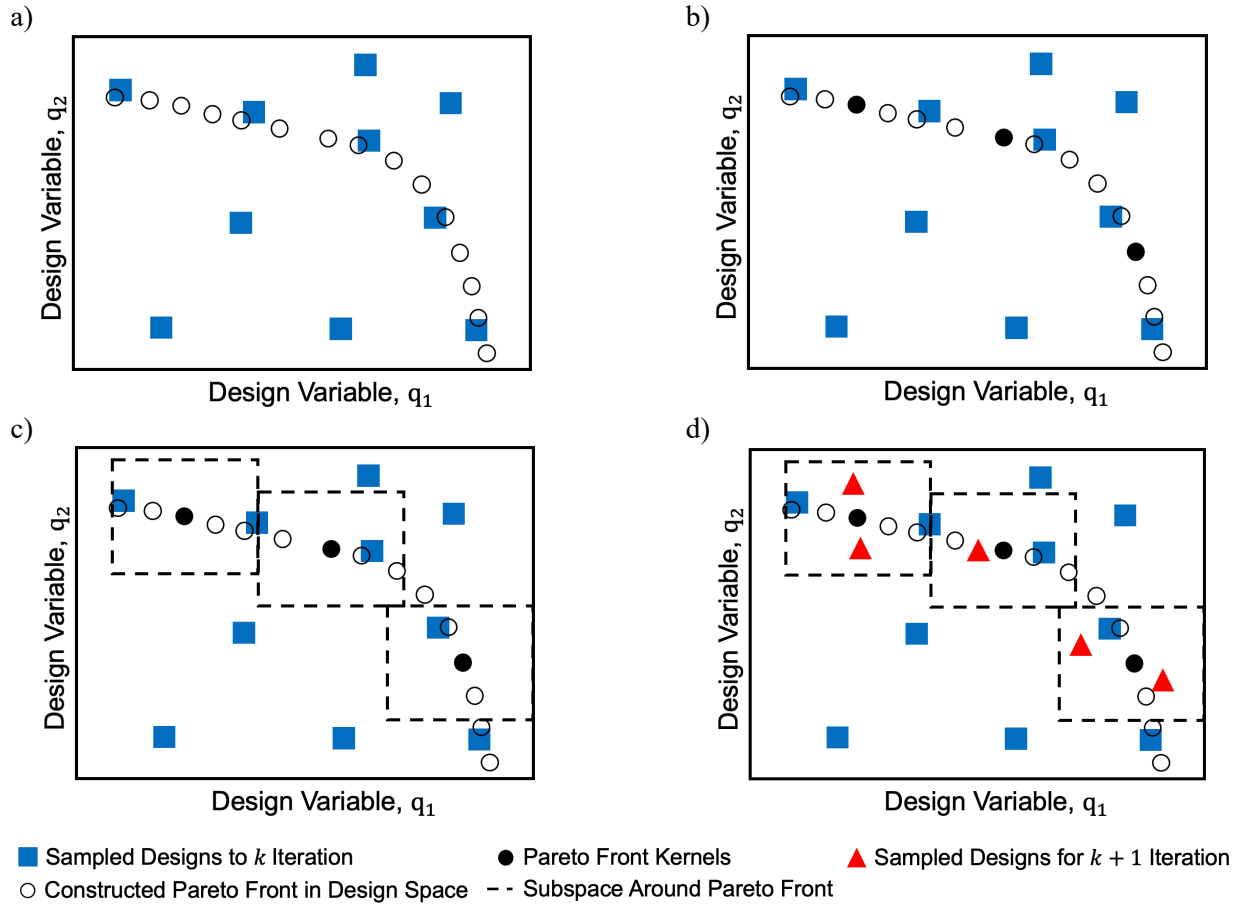
Figure 2.35: Pareto Domain Reduction Schematic. a) Sampled Design Space at Iteration k with Pareto Front, b) Sampling of Pareto Kernels Points, c) Construction of Subspace around Pareto Kernel Points, and d) Sampling Subspace for Iteration $k + 1$.

2.5 Application of Design Optimization in Structural Crashworthiness

As mentioned above, the response surface methodology by Roux et al. [15] is a popular optimization strategy commonly employed in structural lightweighting and crashworthiness applications. In the initial work of Roux et al. [15], the RSM approach was used to perform design optimization of simple truss element structures. Roux et al. [15] investigated different sampling techniques (factorial and D-optimal), quadratic and reciprocal quadratic metamodels, and used Sequential Linear Programming to perform the optimization of the metamodel. They found that bias error in the metamodel cannot be eliminated simply by fitting to more experimental points, but rather that the strongest determinant of accuracy is the size of the domain. Stander and Craig [158] later introduced the domain reduction scheme to address this deficiency in simplified vehicle crash models, material identification, and head impact applications. As smaller domains are considered, the metamodel approaches an approximate linear

functionality with good predictability. Conversely, it can be expected that a higher-order metamodel will accurately fit a larger domain.

Since these pioneering works, RSM has become a standard approach used by many scientists and engineers in the literature (e.g. [5], [6], [18]–[22], [24], [25], [116], [117], [138], [7], [160]–[168], [9]–[14], [17]). Baroutaji et al. [169] has presented a thorough literature review on the application of RSM in structural applications; this section will provide a brief overview of the common themes. The RSM has been applied by many authors to different crashworthiness optimization problems, with a variety of design variables, objectives, and different sampling (e.g., [10], [17], [18], [170]), metamodelling (e.g., [5]–[7], [9], [24], [116], [171]), and optimization techniques (e.g., [7], [172], [173]). Shape parameters (e.g. [10], [20], [22]) and wall thicknesses are common design variables, and many studies consider extensions such as foam-filled tubes (e.g.[5], [14]), tapered tubes (e.g. [7], [9], [14], [17], [19], [160]), and windowed tubes (e.g. [162], [167]).

Several structural optimization studies have been presented on the use of multi-objective optimization in identifying Pareto fronts for design trade-offs [17], [107], [174]. A common challenge when performing structural optimization is the management of the conflicting objectives, such as energy absorption, crushing force, peak crush force, crush efficiency, and mass [9], [11], [12], [17], [22], [160], [165], [166]. Another challenge is the introduction of redundant optimization objectives that create unnecessary complications. This results from heavy reliance on treating metamodels as a "black-box" without intuition that is guided from mechanics principles (i.e., crush mechanics). This challenge was addressed by Kohar et al. [109] by optimizing for maximum crush efficiency instead of minimum peak force. An important advantage of this approach is that it can be shown that SEA and crush efficiency are analytically proportional to each other. A previous work by Kohar et al. [109] showed that peak force is proportional to the cross-sectional area (A) of the tube. This allows crush efficiency and SEA to be written as

$$\eta_{crush} = \frac{F_{mean}}{F_{peak}} \propto \frac{F_{mean}}{A} \tag{2.96}$$

$$SEA = \frac{F_{mean}\delta}{Mass} = \frac{F_{mean}\delta}{A * l} \tag{2.97}$$

Equations 2.96 and 2.97 can be rearranged to give

$$SEA \propto \frac{\delta}{l}\eta_{crush} \tag{2.98}$$

which shows that crush efficiency and SEA are proportional, and only a single-objective optimization needs to be performed on either objective to achieve a simultaneous optimization of both. However, this study was limited only to axial loading conditions.

Various studies focus on the design optimization of lightweighting subjected to various loading conditions, such as oblique impact [5], [21], [22]. Baroutaji et al. [175] utilized an RSM-based multi-objective optimization approach to analyze the geometric parameters of circular tubes subjected to quasi-static lateral loading. Tanlak [20] considered a shape optimization problem using a complete multi-objective optimization approach to investigate the design of crush rails impacted at a 10° angle for maximal energy absorption and minimal peak force. Ying et al. [6] performed a multiobjective crashworthiness optimization of thin-walled structures with functionally graded strength under oblique impact loading. Although these works mentioned above show good performance in satisfying their specific optimization problem, many of these works perform the optimization step "out-of-loop".

2.6   Deficiency in Literature

The widespread use of the RSM approach in crashworthiness research has enabled a wide variety of optimization studies to be performed. Although recent works have increasingly begun to consider oblique impact conditions and multi-objective optimization, the literature is still limited in the area of multi-objective optimization across multiple impact angles. This is a critical research area because most real-world crashes will include some element of oblique impact. There is a need to establish better the degree to which axial crush performance and oblique crush performance correlate. This will highlight the relative importance of further oblique crush research, such as experimental testing and complete multi-objective optimization studies.

Next, the traditional form of the RSM approach that performs optimization after reaching sufficient metamodel accuracy remains the dominant technique. Only a few works consider the optimization process "in-the-loop" of the RSM (e.g. [5], [11], [24], [25], [163], [168]), with particular applications to oblique loading. Qi et al. [7] performed a successive multi-objective optimization study of tapered square tubes subjected to various oblique loading conditions. Their study used polynomial response surfaces with multi-objective particle swarm optimization (MOPSO) to conduct their analysis. The optimization operation was conducted after each metamodel sampling, fitting, and iteration. However, the next samples were generated using a full-factorial design of experiments that populated the entire domain. Acar et al. [9] performed a multi-objective optimization study of tapered circular tubes with various initiator designs subjected to only axial crush. Various metamodelling schemes were explored throughout the study, and the optimization operation was incorporated into the iteration scheme. Similarly, new samples were generated using either

a full-factorial design of experiments or Latin-hypercube sampling. This can become quite computationally expensive for large numbers of design parameters with slow convergence. This approach still decouples the optimization process from assisting in any future sampling of the domain.

However, the usage of the traditional RSM approach still dominates despite the development of powerful advanced RSM techniques, such as the ASA-RSM approach proposed by Stander [23] as discussed in Section 2.4.2. Stander [23] demonstrated the efficiency of ASA-RSM for an example in designing a vehicle for noise, vibration, and harshness (NVH). Although good performance is achieved, the multi-objective optimization results were not compared to the "true" Pareto front. Many of the works mentioned above never compare their predicted multi-objective optimization solutions, such as the generated Pareto front, with the true solution of the optimization problem. Yet, this ASA-RSM approach shows significant potential in multi-objective optimization of structural crashworthiness applications, such as axial and oblique crush. Together, these deficiencies highlight the need for highly-intelligent response surface methods to be utilized in crashworthiness research, allowing larger and more accurate multi-objective studies to be performed.

3 SCOPE AND OBJECTIVES

The scope of this thesis is to investigate the multi-objective optimization process of a multi-cellular extruded aluminum crush rail under axial and oblique impact. The optimization process will be evaluated to determine the "true" Pareto front and the computational cost. Finite element models of the Baseline and UWR4 extruded profiles that were presented in Kohar et al. [24]–[26] are developed, validated against dynamic axial crush experiments, and extended to simulate oblique impact conditions. It should be reiterated that the Baseline and UWR4 profiles presented in Kohar et al. [24]–[26] were initially developed for a single (axial) loading condition. Therefore, this study will evaluate the UWR4 profile's sensitivity to oblique impact loading compared to the Baseline profile. A simplified FE model of the UWR4 that is computationally efficient is created and used to perform a parametric study that exhaustively searches the entire design space. The true solution (i.e., true Pareto front) to the multi-objective optimization problem is determined. Next, the Response Surface Method (RSM) optimization framework is developed and used to analyze the same optimization problem. The traditional RSM configuration used in the crashworthiness literature is performed alongside the Adaptive-Surrogate-Assisted (ASA-RSM) method proposed by Stander [23] to compare the performance of the two methods.

3.1 Objectives

The objectives of the current research are to:

1. Develop, validate, and evaluate the energy absorption characteristics of the UWR4 and Baseline profile for various oblique loading conditions;
2. Perform an exhaustive parametric study of the UWR4 design space to evaluate the design's sensitivity to various energy absorption metrics. This will also evaluate the suitability of this application as a multi-objective optimization problem and identify the "true" Pareto front to the prescribed criteria and constraints;
3. Implement and evaluate the ability of the traditional RSM approach to achieve the "true" Pareto front. This will serve as the baseline for evaluating the ASA-RSM approach;
4. Implement, evaluate and compare the ASA-RSM method with the traditional RSM approach.

3.2 Limitations of the Current Work

This work utilizes FE models to perform the parametric and optimization studies for the various loading conditions. It should be noted that no experimental data is available for the oblique impact response of the UWR4 and Baseline. However, it is assumed that the FE models can accurately capture any loading condition if the model can well capture the axial loading condition where experimental data is available.

Next, it is assumed that the oblique crush boundary conditions accurately represent a dynamic oblique impact, and the results of the model are representative of real-world loading conditions. It is also assumed that the simplified model represents the crushing process sufficiently accurately for the trends in the force-displacement responses to be correctly identified. Although Kohar et al. [25][109] showed that solid elements provide the highest accuracy, it is assumed that the shell model assumptions hold valid (i.e. plane stress, linear through-thickness strain, the in-plane gradient of through-thickness displacement is small, and small rotations), and that the contact and boundary conditions sufficiently represent the physics of the problem. In particular, the friction model in the contacts, the damping of the impact, and the stress wave propagation through the bodies are all correct.

The material properties have been carefully tested and characterized by previous research efforts [24], [27]. This is important because the manufacturing process of the aluminum extrusions introduces significant anisotropy in the material. However, the shape of the extrusion dies, the flow of the material, and the resultant material properties (i.e., yield strength, failure and fracture), would vary as changes are made to the shape of the cross-section. In this work, this variance is neglected and it is assumed that all designs would have equal material properties. During dynamic impact, adiabatic heating can be generated locally by the material from the conversion of plastic work ($W^P = \chi \boldsymbol{\sigma} : \boldsymbol{\varepsilon}^P$) to heat. Kohar et al. [176] showed that a coupled thermodynamic-mechanical model could impact the dynamic crush response of advanced high strength steel structures. Williams et al. [95] incorporated a thermal model into the constitutive model of AA5754-O to simulate the crush response aluminum square tubes. However, it is assumed that the strain-rate sensitivity model used in this work implicitly captures the thermal effects in the stress-strain response. Therefore, a fully coupled thermomechanical formulation is not used in this study.

Finally, the optimization study is limited to three design variables (shape parameters) and four objective functions encompassing two impact angles. A more comprehensive study would include more design variables (e.g. wall thicknesses, functionally graded strength/thickness, material properties), and more objective functions across more impact angles (e.g. critical angle, energy absorption for 10° and 30°).

4 FINITE ELEMENT MODELLING

This chapter presents the finite element (FE) modelling approach that is employed in this work. The non-linear explicit dynamic formulation of the commercial FE software, LS-Dyna [62], is used throughout this work to simulate the axial and oblique crushing response of lightweight aluminum crush rails. FE models are constructed to follow the experimental study presented in Kohar et al. [24], [25] and Zhumagulov [96] for the axial crushing of lightweight aluminum extrusions. These experimental studies report the axial crush response of two designs of a lightweight aluminum extrusions, known as the Baseline and UWR4 profiles, which were crushed using a linear sled apparatus. Details about this experimental setup, FE model construction, and model correlation are presented in this chapter. Unfortunately, experimental oblique impact crushing was not performed for these aluminum extrusions. Nevertheless, a synthetic oblique crush experiment is designed with finite elements to predict the response during oblique crush. Details about the FE model construction for oblique loading are also presented. Finally, details about a simplified FE model used for a parametric and optimization study are also presented and discussed.

4.1 FE Modelling of Axial Crush

4.1.1 Experimental Setup of Dynamic Axial Crush

Figure 4.1 presents the cross-section profiles of the two aluminum extrusions, known as the Baseline and UWR4, that will be studied in this work [24]. Geometric properties (mass, length, second moment of area) of each profile are presented in Table 4.1. These extrusions were manufactured from commercially available aluminum alloy AA6063-T6 and had an initial uncrushed length of 525mm. These aluminum extrusions were individually crushed using a sled-track apparatus at the University of Waterloo. Figure 4.2 presents a schematic of the linear sled apparatus setup that was used for axial crushing. The mass and initial speed of the sled was 855kg and 8m/s, respectively. Steel plates and bosses are clamped with bolts on each end of the crush rail. The boss on the free and fixed end is 19mm and 38mm in height, respectively. Aluminum honeycomb blocks were used to dissipate excess sled energy; this provided an uninterrupted crush length of 125mm. A 12.7mm thick plywood sheet was attached to the free end to provide some damping against structural noise from the impact. Piezoelectric load cells on the wall were used to record the crushing force response. No crush initiators were used in these experiments.
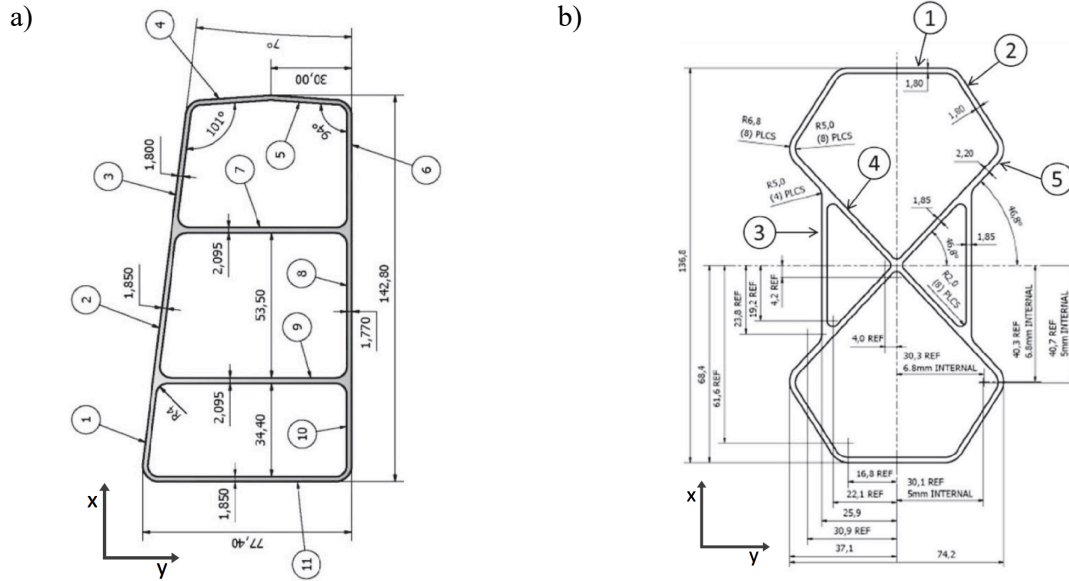
Figure 4.1: Cross Section Geometry of a) Baseline and b) UWR4 Aluminum Extrusion Profiles [24].

Table 4.1: Geometric Properties of Baseline and UWR4 Profile.

	Mass [kg]	Length [mm]	Second Moment of Area I_{xx} (10^6) [mm^4]	Second Moment of Area I_{yy} (10^5) [mm^4]
Baseline	1.48	525	2.166	7.974
UWR4	1.40	525	1.586	5.219
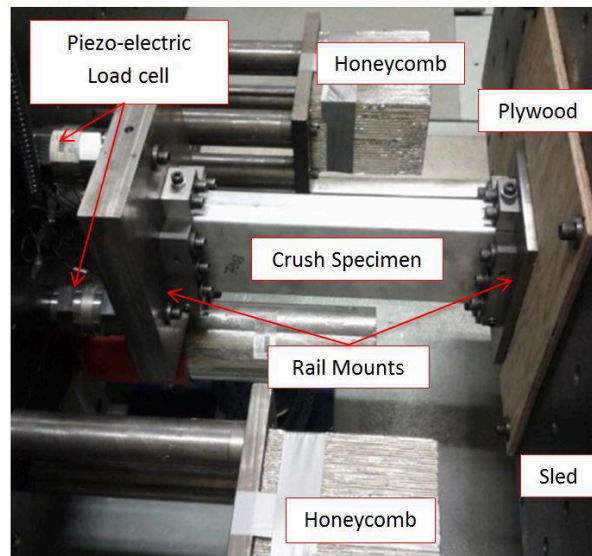
Figure 4.2: Schematic of Linear Sled Apparatus Experimental Setup [27].

4.1.2 Detailed FE Model Construction for Axial Crush

4.1.2.1 Details for Geometry Setup of Axial Crush

Figure 4.3 presents a schematic of the FE model construction of the Baseline and UWR4 axial crush setup. Each FE model consists of the crush rail, bosses and plates attached to each end of the crush rail, and the linear impacting sled mass. The impacting mass (used to simulate the effect of a crash sled) is a large rectangular mass and begins in contact with the free-side plate. A detail for the bosses used for the free end fixture in the FE model, which is similar to the boss on the fixed end, is presented in Figure 4.4. This shows that the effect of the bolts that clamp and retain the axial crush rail is captured in the model. However, no preloading force was applied to these components. The mesh was created using the commercial software Altair Hyperworks Hypermesh.
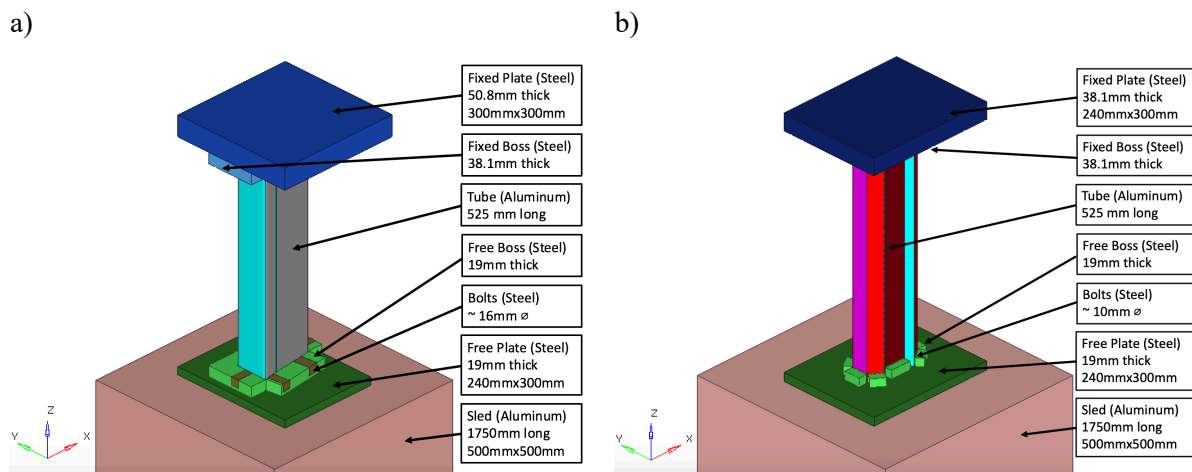
Figure 4.3: Detailed FE Model of a) Baseline and b) UWR4 Crush Rails.
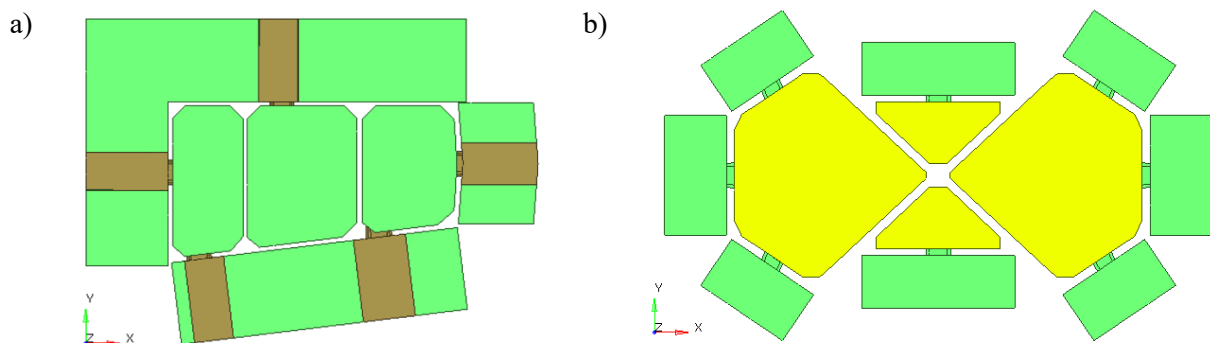
Figure 4.4: Axial View of a) Baseline and b) UWR4 Boss FE Model Detail.

4.1.2.2 Mesh Information for Detailed FE Models of Axial Crush

The models of the Baseline and UWR4 profiles are presented in Figure 4.5, with only one-quarter of the mesh of the UWR4 shown for visual clarity. All simulations of the UWR4 require a full model to capture the crushing folds that cross the symmetry plane and interact with each other. Shell elements are used to model the rails. As described in Section 2.3.1.3, shells use the theory of plates to reduce the dimensionality of the elements while introducing additional (rotational) degrees of freedom to the nodes. Unless a very dense solid element mesh is used, shell elements capture bending behaviour much more accurately than solid elements. As a result, these shell elements can provide a computationally efficient option for analyzing large deformations in thin-walled structures. However, the assumption of negligible through-thickness stresses can lead to errors in the energy absorption response due to complex deformation patterns that can arise during crush [109]. Shell elements require additional computational functionality to compensate for the lack of through-thickness complexity, such as thickness update, hourglass suppression, and warping stiffness (see Belytschko, Wong, and Chiang [177]). All shell elements in this work are 4-node quadrilaterals using the Belytschko-Tsay (*SECTION_SHELL *ELFORM=2) shell model [178] with a velocity-strain formulation and co-rotational coordinates. Each section of the crush rail uses its own section identification (*SECTION_SHELL) to capture the thickness variation in the extrusion. Each FE model uses approximately 1mm x 1mm elements with 3 integration points through the thickness. Options are enabled to update the shell thicknesses based on the calculated through-thickness strain and full projection schemes for warping stiffness.

a)   b)
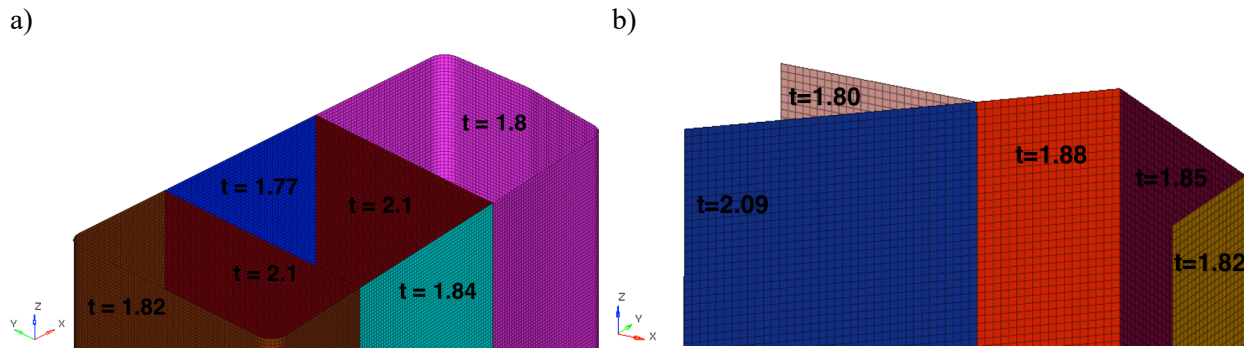
Figure 4.5: a) Baseline and b) UWR4 Mesh.

Figure 4.6 presents the Baseline and UWR4 FE models with all other components in the simulation. The remaining parts (bosses, plates, bolts, and impactor) utilize a much coarser mesh for improved computational efficiency. Solid elements are used exclusively for these components. The element sizes are approximately 5mm, 75mm, and 8mm for the bosses, impactor, and plates respectively.
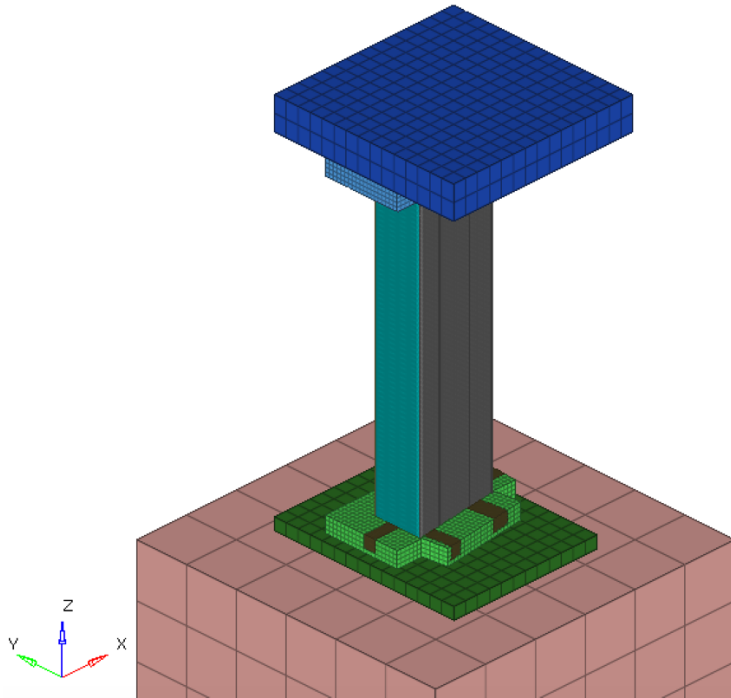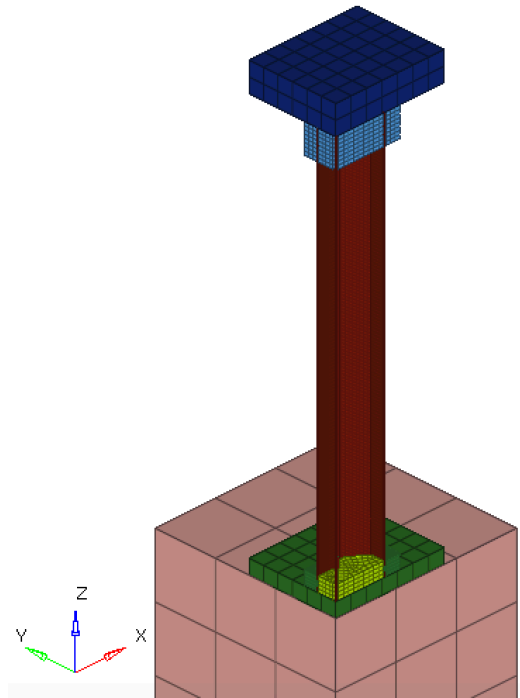
Figure 4.6: Complete Mesh of Detail of a) Baseline and b) UWR4 Models.

4.1.2.3 Material Modelling and Properties

The bosses, plates, and impacting mass are assumed to have small deformations far below the yielding of their material. The components are assumed to have an isotropic linear elastic material behaviour (*MAT_002 in LS-Dyna). Table 4.2 presents the elastic material properties used in the simulations. The properties of the bosses and plates are set to typical values for steel, while the impacting mass utilizes the material properties of aluminum. The density of the impactor is scaled to create a mass of 855kg.

Table 4.2: Elastic Properties of Bosses, Plates and Impacting Mass.

	Bosses & Plates	**Impacting Mass**
Density [g/mm³]	7.80×10^{-3}	1.92×10^{-3}
E [MPa]	200 000	69 000
ν	0.3	0.3

The aluminum extrusion crush rail requires an advanced material model that can account for severe plastic deformations and high-strain rates generated during axial crush. Kohar et al. [24] performed characterization of the aluminum alloy AA6063-T6 used in their experimental study. Figure 4.7 presents the true stress-true strain response for AA6063-T6 for different strain-rates that were obtained from Kohar

71

et al. [24]. In a later study, Kohar et al. [25] generated the Voce-hardening and Cowper-Symonds parameters to describe the response of AA6063-T6. Table 4.3 presents the material constants for the Voce-hardening and Cowper-Symonds model for AA6063-T6 from Kohar et al. [25] that will be used in this study.
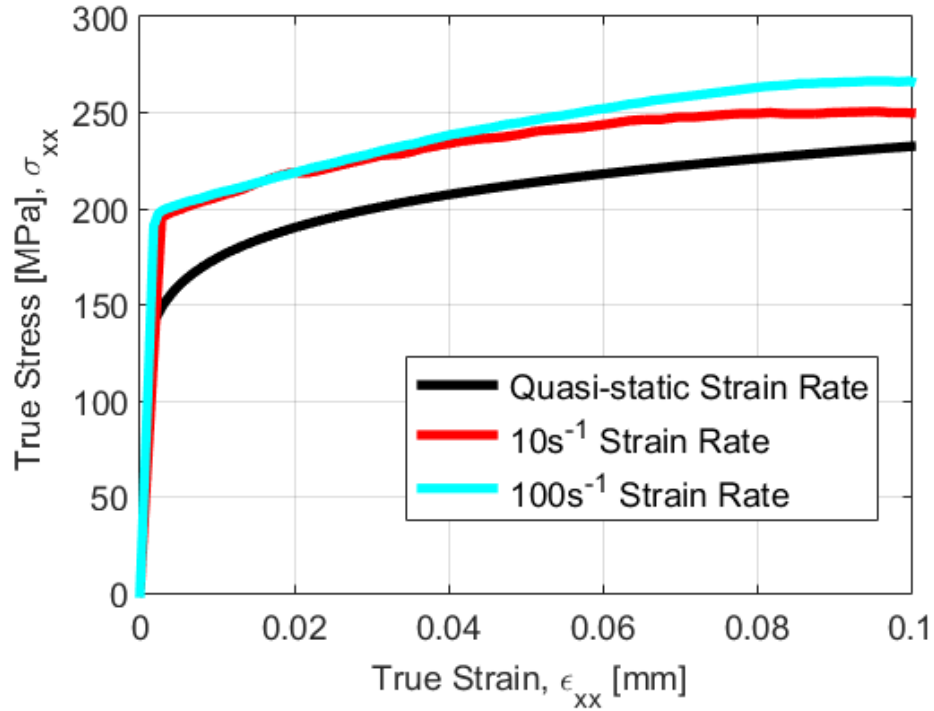
Figure 4.7: True Stress-True Strain Response for AA6063-T6 at Different Strain Rates [24].

Table 4.3: Flow stress hardening parameters for aluminum alloy AA6063-T6 [25].

σ_y [MPa]	σ_{UTS} [MPa]	D	M [s^{-1}]	q
180	235	20	24.6×10^{-9}	8.88

Since the aluminum crush rails are fabricated via the extrusion process, large manufacture-induced plastic anisotropy is present in the material that needs to be accounted for in the model. Kohar et al. [25] showed that utilizing the Yld2004-18p anisotropic yield function by Barlat et al. [90] produced better predictions for the force and energy-displacement responses of the Baseline profile. Following suit, this current work will employ the Yld2004-18p anisotropic yield function to capture the plastic anisotropic behaviour of the extruded aluminum alloy AA6063-T6. The Yld2004-18p constitutive model is implemented as a user-defined material subroutine (UMAT) within LS-Dyna (*MAT_USER_DEFINED_MATERIAL_MODEL) that utilizes the Voce-hardening and Cowper-Symonds rate sensitivity model. The reader is referred to Kohar et al. [78] for details about this implementation. The Yld2004-18p parameters obtained by Kohar et al. [25] are used in this work and are

72

presented in Table 4.4. The resulting yield surfaces are plotted in Figure 4.8. Since the Yld2004-18p yield function is anisotropic, a set of coordinates that defines the material directions must be declared. For shell elements, this is accomplished by defining the extrusion direction (AOPT=2 option in LS-Dyna) along the unit normal in the z-direction (Figure 4.6). LS-Dyna then internally uses the node numbering to determine the direction of the normal (ND) for shell elements to compute the direction of the transverse direction (TD). Invariant node numbering (*CONTROL_ACCURACY) is used to maintain a consistent element coordinate axis to use an anisotropic functions with large deformation.

Table 4.4: Yld2004-18p Parameters Used for Aluminum Alloy AA6063-T6 ($m = 8$) [25].

	c_{12}	c_{13}	c_{21}	c_{23}	c_{31}	c_{32}	c_{44}	c_{55}	c_{66}
c'	5.30	4.54	-3.68	1.66	-2.48	1.03	0.43	0.69	0.69
c''	3.79	4.20	-4.80	-0.15	-3.76	-0.57	-1.10	0.86	0.87

a)   b)
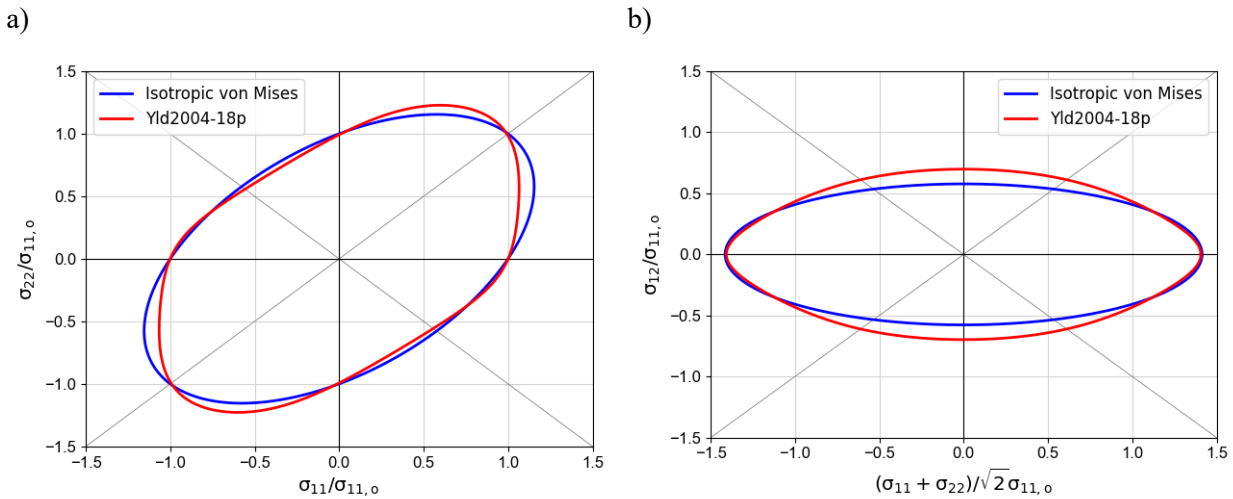
Figure 4.8: Yield surfaces for Aluminum Alloy AA6063-T6, shown in the a) $\sigma_{12} = 0$ plane and b) $\sigma_{11} = \sigma_{22}$ plane.

4.1.2.4 Boundary Conditions for Detailed FE Models of Axial Crush

There are three sets of boundary conditions applied: a fixed set of nodes, the initial velocity of the impactor, and the constrained motion of the impactor. Figure 4.9 presents the fixed sets of nodes that mimic the attachment to the rigid wall. The impactor mass has an initial z-direction velocity of 8m/s. All nodes of the mass impactor are constrained to allow motion in the z-direction only ($U_x = U_y = 0$).

73
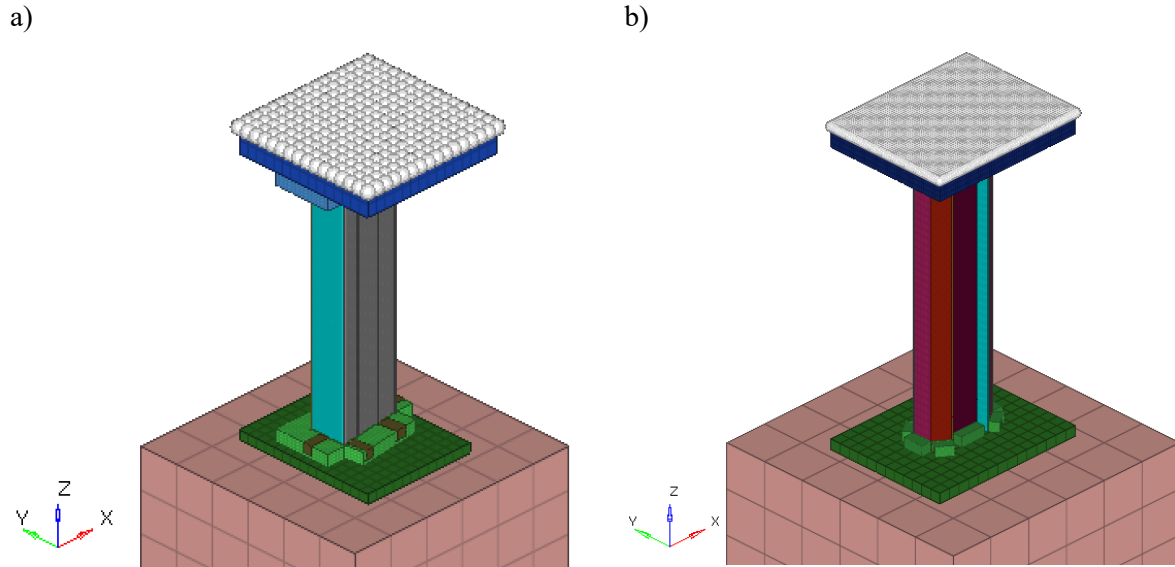
Figure 4.9: Fixed Nodes on the a) Baseline and b) UWR4 FE Models.

4.1.2.5 Defining Contact for Detail FE Models of Axial Crush

Penalty-based contact formulations are used to capture the interaction of the different components. The following interfaces are defined:

1) Aluminum Rail Self-Contact
   a. FS = 1.04, FD = 1, VDC = 0
   b. LS-Dyna keyword *CONTACT_AUTOMATIC_SINGLE_SURFACE
2) Aluminum Rail to Bosses and Plates
   a. FS = 0.45, FD = 0.4, VDC = 0
   b. Soft = 2 segment-based formulation
   c. LS-Dyna keyword *CONTACT_AUTOMATIC_SURFACE_TO_SURFACE
3) Impactor to Free-Side Plate
   a. FS = 0.45, FD = 0.4, VDC = 0.15
   b. LS-Dyna keyword *CONTACT_AUTOMATIC_SURFACE_TO_SURFACE
4) Tied Contact between Boss, Bolts, and Plate (on each side)
   a. LS-Dyna keyword *CONTACT_TIED_SURFACE_TO_SURFACE

The friction values were obtained from Kohar et al. [24], [25], [109]. The decay value is DC=1 for all cases. The viscous damping coefficient for contact, VDC, is equal to zero except at the interface of the plate and impactor where experimentally a wooden board is placed to provide some damping against the metallic ringing.

4.1.3 Simulation Results of Detailed FE Model for Axial Crush

Table 4.5 presents the computational resources required for each FE simulation. Each simulation utilized a high performance computing cluster consisting of 2.70 GHz Intel Xeon E5-2680 processors. The number of cores allocated to each simulation was optimized to minimize inter-processor communication.

Table 4.5: Computational Time Required for FE Models of Baseline and UWR4 Profile.

	Axial Crush			Oblique Crush		
	num. cpus	Time [Hrs]	Core Hours # cpus × Time [Hrs]	num. cpus	Time [Hrs]	Core Hours # cpus × Time [Hrs]
Baseline	64	14.0	896	64	10.0	640
UWR4	72	16.3	1174	64	16.4	1050

4.1.3.1 Verification of FE Model Setup

Before discussing the results of the FE models, several checks are performed to determine the quality of the analysis by examining the energy balance. There is an initial velocity applied to the impact but no external forces, such that the total energy in the system must remain constant at any moment. Initially, all energy in the system is kinetic. As time progresses, the majority of the kinetic energy should be absorbed internally within the crush rail. The amount of energy generated from friction (known as sliding energy) and the hourglass energy should be small compared to the internal energy. If the results deviate substantially from any of these expectations, it is a signal that the FE models are poorly designed. Figure 4.10 shows a composition plot of the different energy components for the axial crush simulations of the Baseline and UWR4 profiles. The energy balance of the models meets these expectations; thus, the results can be used and compared with experiments.
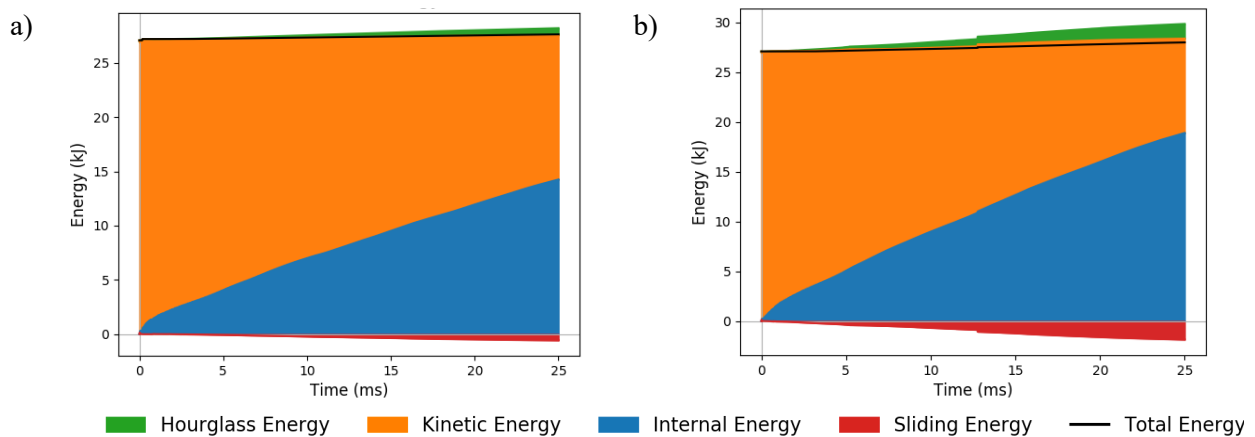
Figure 4.10: FE Model Energy Balance for a) Baseline and b) UWR4 Simulations.

4.1.3.2 Comparison of Detailed FE Simulation Results with Experiments for Axial Crush

Figure 4.11 presents the deformed structures of the Baseline and UWR4 profile, respectively. Each FE model appears to capture the crush modes observed in experiments. Figure 4.12 compares the experimental and simulated mean crush and energy absorption response of the Baseline and UWR4 profiles. The experimental data presented in Kohar et al. [24] was filtered using an SAE CFC 180 filter [179] and reported for a crush distance of 125mm. Since all crush experiments are measured at a crush distance of 125mm, measurements of crush efficiency, energy absorbed, or specific energy absorbed may be directly calculated using only the mean crush and peak force. In other words, a good correlation between the mean crush and peak crush force will be a good indicator in the correlation between crush efficiency, energy absorbed, and specific crush efficiency. All simulations in this study were filtered using the SAE CFC 180 filter and measured at 125mm to ensure a proper comparison. The simulated force-response was obtained by measuring the reaction forces of the fixed nodes of the bottom boss (Figure 4.9). A summary of the simulated and experimental mean crush force, peak crush force, and crush efficiency for the Baseline and UWR4 profile are presented in Table 4.6.

a) Baseline Experiment   b) Baseline FE Model   c) UWR4 Experiment   d) UWR4 FE Model
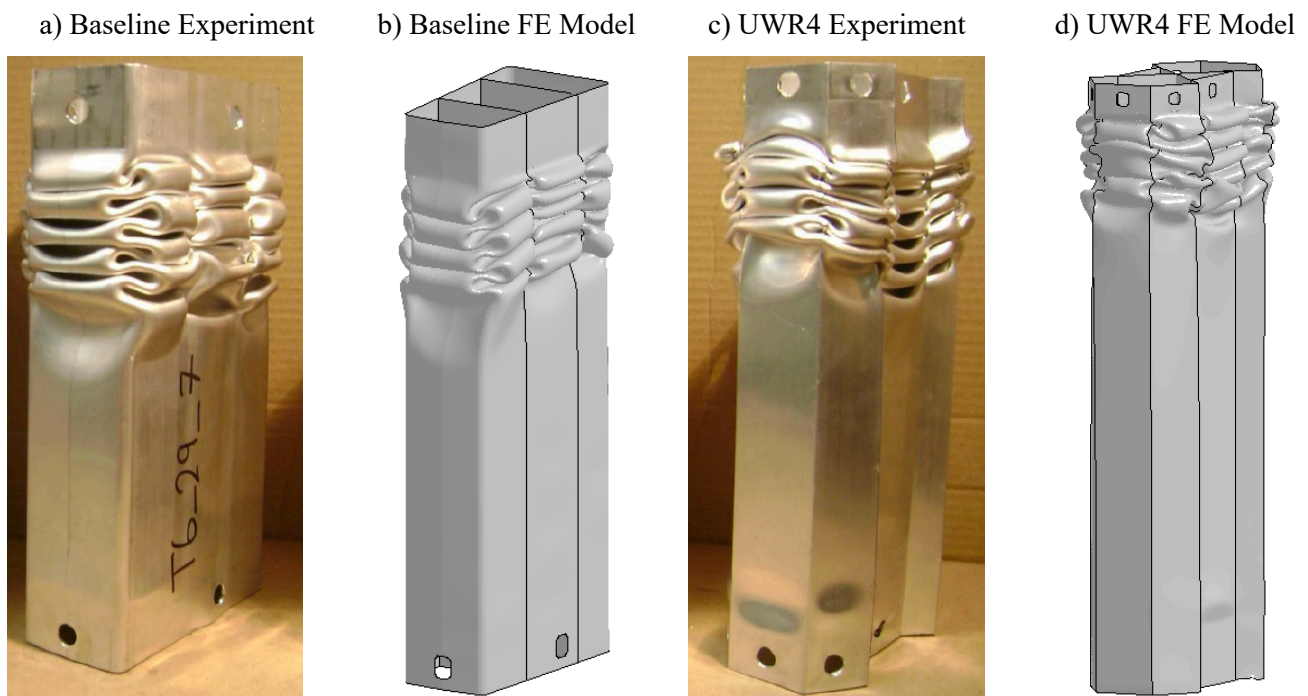
Figure 4.11: Images of the Experimental [24] and Simulated Deformed Shape of the Baseline and UWR4 Profiles.
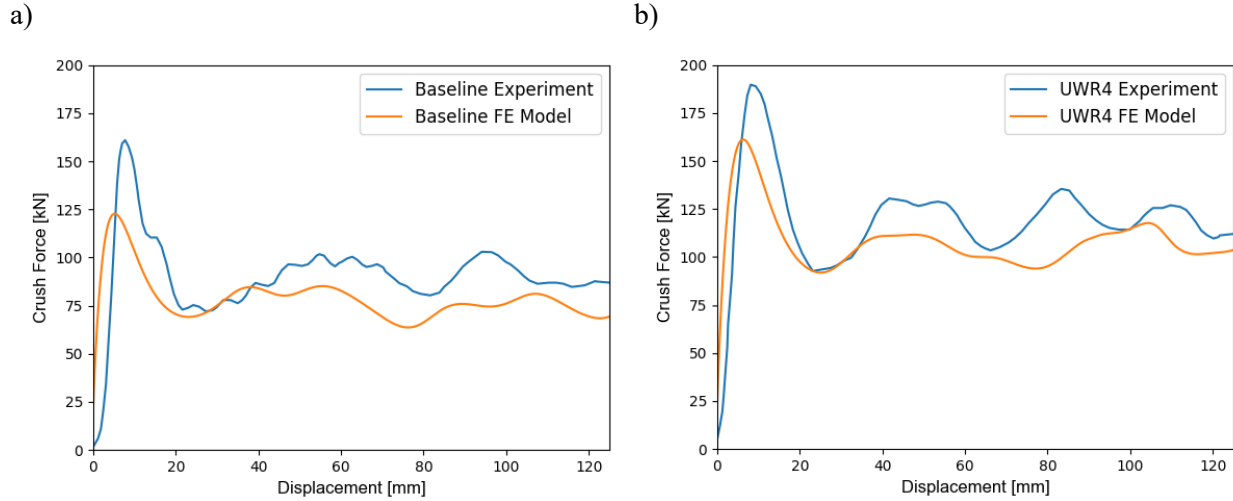
Figure 4.12: Comparison of Experimental [25] and Simulated Crush Force Response of a) Baseline and b) UWR4.

Table 4.6: Experimental and Simulated Results and Error for Mean Crush Force and Peak Crush Force.

	Detailed Baseline Model			Detailed UWR4 Model		
	F_{mean}^{axial} [kN]	F_{peak}^{axial} [kN]	η^{axial}	F_{mean}^{axial} [kN]	F_{peak}^{axial} [kN]	η^{axial}
Experiment	90.6	160.9	0.56	119.5	189.7	0.63
Detailed FE Model	79.1	122.7	0.65	108.4	161.2	0.67
Δϵ Exp. to FE Model (%)	-12.7	-23.7	+8.2	-9.3	-15.0	+4.2

The FE model of the Baseline profile predicted a mean and peak crush force of 79.1kN and 122.7kN respectively; The difference in prediction error with respect to the experimental response was -12.7% and -23.7%. The UWR4 FE model predicted a mean crush force of 108.4kN and a peak crush force of 161.2kN. The model prediction error for the mean crush and peak force was -9.3% and -15.0%, respectively. Note that the reported experimental values were an average of three repeats of each crush test. The mean crush and peak force varied by up to 1% and 6.9%, respectively, for the Baseline profile and by 4.1% and 2.3% for the UWR4 profile [27]. The FE models consistently underpredicted the mean crush force response by approximately 10-12%. This difference is caused by the inability of the shell element models to accurately capture multi-axial stress states through the thickness of the deformed section [108], [109]. Yet, the simulation can capture the trends observed in the force-displacement response, the resulting deformation behaviour for both profiles, and indicate that the UWR4 outperforms the Baseline profile in axial crush. Overall, it is concluded that both the FE models developed in this work are valid; it is assumed that these models may be used to perform meaningful studies for different loading scenarios and design optimization.

4.2   FE Modelling of Oblique Crush

The UWR4 profile was originally developed and proven superior in axial crush performance compared to the Baseline profile [24]. Since experiments and simulations of oblique impact simulation were not considered in these previous works [24], [25], the Baseline profile may outperform the UWR4 under oblique impact loading. This section details the FE model construction to evaluate the Baseline and UWR4 profile performance subjected to oblique impact loading.

4.2.1   Detailed FE Model Construction for Axial Crush

Figure 4.13 presents the FE models for the oblique impact loading of the Baseline and UWR4 profiles. These oblique impact FE models utilize the same construction methodology presented in the axial crush studies (Section 4.1.2). Oblique loading is generated by rotating the entire crush assembly by an angle, θ, about one edge of the free plate. The impacting body (used to simulate the effect of a crash sled) is modified to incorporate 35.0mm raised edges to arrest lateral motion of the crush rail during oblique loading. Similar boundary conditions for constraining the structure (Section 0) and applying contact (Section 4.1.2.5) were used in this study. Using a similar FE model construction, a similar computational time was required to complete the oblique crush simulations as the axial crush models. All simulations in this study were filtered using the SAE CFC 180 filter and measured at 125mm.

a)   b)
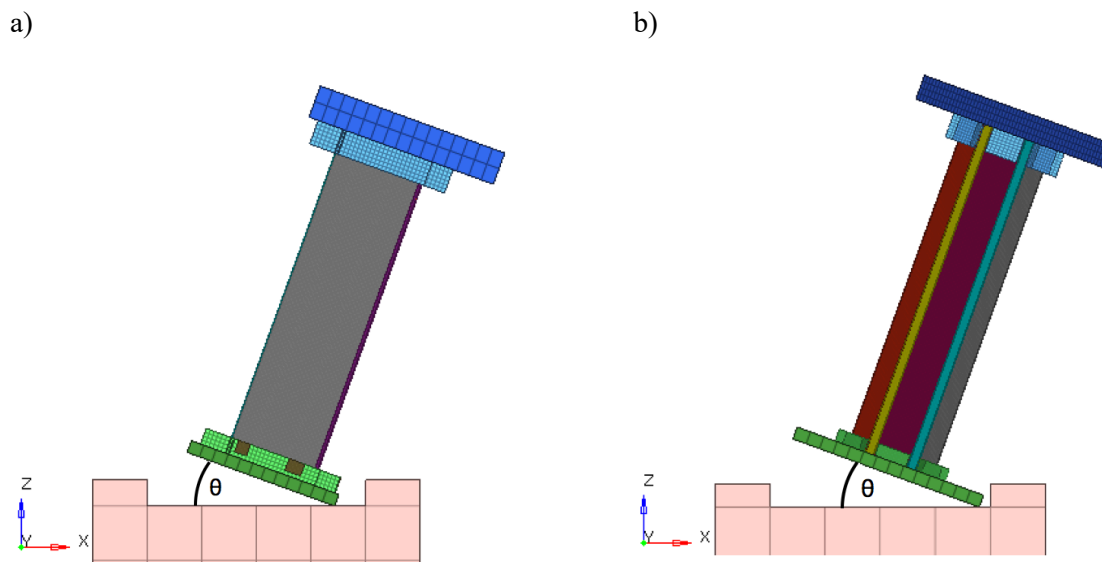
Figure 4.13: Rotated Detail Models of a) Baseline and b) UWR4 Profiles for Oblique Impact Loading.

4.2.2 Simulation Results of Detailed FE Model for Oblique Crush

4.2.2.1 Verification of FE Model Setup

The importance of checking the simulation energy balance was discussed in Section 4.1.3.1. The total energy should remain roughly constant, the internal energy should increase, the kinetic energy should decrease, the ratio of hourglass energy to internal energy should be low, and a small amount of sliding energy will appear as the simulation progresses. Figure 4.14 shows the energy balance for the Baseline and UWR4 profiles. The total energy increases slightly as the simulation progresses because some external forces are applied by the hourglass control algorithm to arrest the hourglass deformation modes, which adds a small amount of spurious hourglass energy to the simulation. Despite this, the total increase in energy is well within normal expectations.

a)   b)
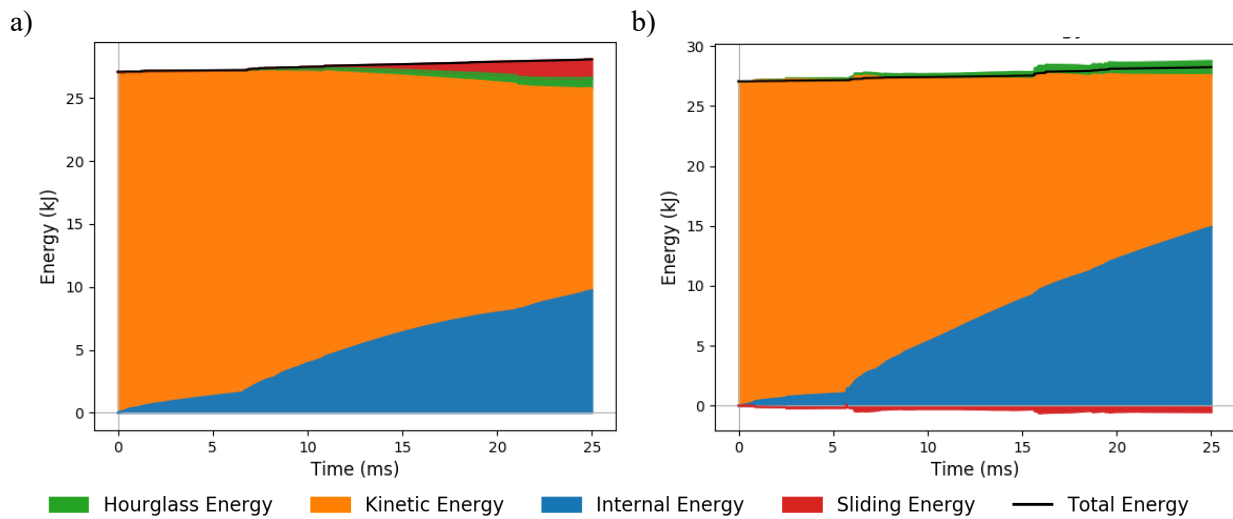
Figure 4.14: FE Model Energy Balance for a) Baseline and b) UWR4 Simulations.

4.2.2.2 Simulation Results of Detailed FE Model for Oblique Crush at 20° Angle

Figure 4.15 presents the deformation response correlated with the Baseline and UWR4 profile force-displacement response subjected to oblique impact loading at an initial angle of 20°. This angle was selected because it is an approximate representation of the kinematic rotation that a crush rail is likely to experience in a full-vehicle collision. The deformation stages of the oblique impact loading follow an initial elastic loading as the crush rail begins to bend and rotate. Once the rotation is complete, the structure stiffens and generates a second peak crush force that transitions into progressive folding. Table 4.7 summarizes the mean crush and peak crush force of the Baseline and UWR4 profiles. The simulation of the Baseline profile predicted a mean crush force and peak crush force of 55.7kN and 91.1kN, respectively. The UWR4 was predicted to have a mean crush force and peak crush force of 73.5kN and 109.8kN, respectively.

Figure 4.16 presents a direct comparison between the UWR4 and the Baseline profile in an oblique crush. The UWR4 has a higher initial peak crush force than the Baseline profile. However, despite generally having lower axial crush performance, the performance in energy absorption of the Baseline is greater than the UWR4 for a portion of the early crushing process, and after ~50mm of oblique crush, the mean crush response is similar to the UWR4. This difference can be attributed to the differences in area moment of inertia. The Baseline profile has a larger area moment of inertia that lends itself to higher resistance in the bending and rotation during the oblique crush between the first and second peaks. Yet, the absolute performance of the UWR4 over a crush distance greater than ~50mm is predicted to be superior to the Baseline profile in an oblique crush. After the first fold forms, the progressive folding begins, and the force response of the UWR4 dominates the Baseline profile. However, it is recommended that this result be verified experimentally.
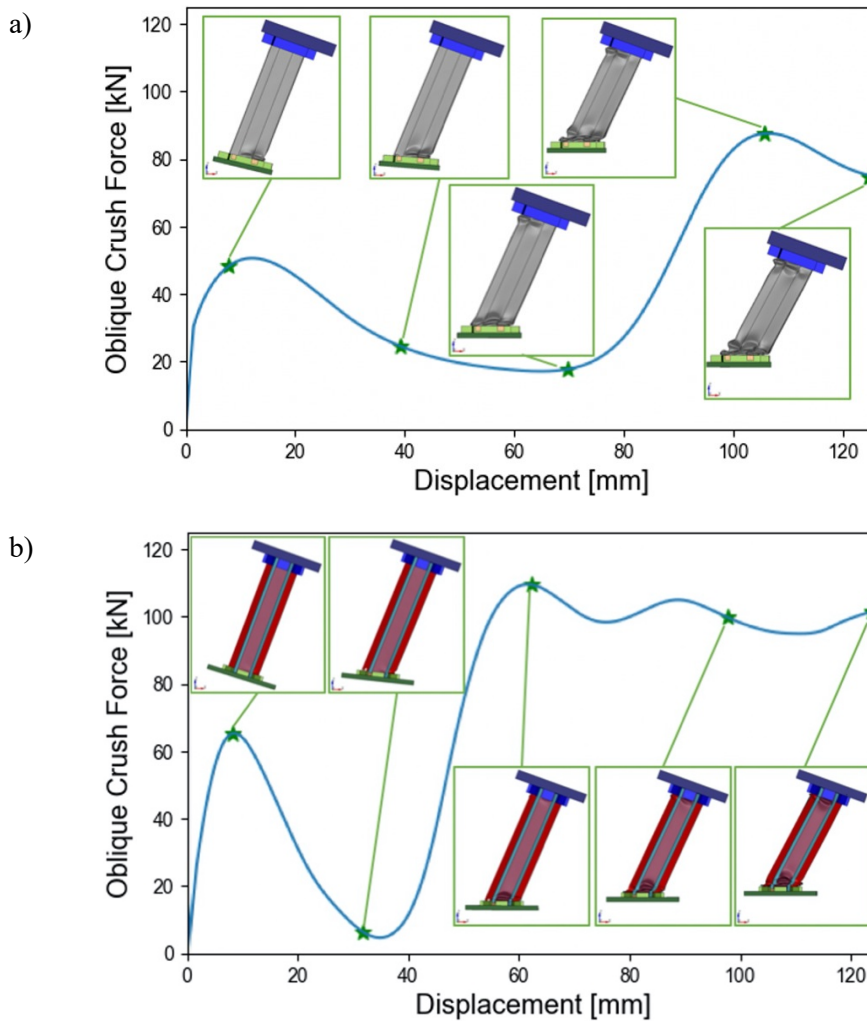
Figure 4.15: Correlated Deformation and Force-Displacement Response of a) Baseline and b) UWR4 Subjected to Oblique Impact Loading.

Table 4.7: Comparison of energy absorption metrics for detailed Baseline and UWR4 FE model in oblique crush.

Detailed Baseline Model					Detailed UWR4 Model				
$F_{mean}^{oblique}$ [kN]	$F_{peak}^{oblique}$ [kN]	$\eta^{oblique}$	λ_{mean}	λ_{peak}	$F_{mean}^{oblique}$ [kN]	$F_{peak}^{oblique}$ [kN]	$\eta^{oblique}$	λ_{mean}	λ_{peak}
55.7	91.1	0.61	0.70	0.74	73.5	109.8	0.67	0.68	0.68

a)

b)
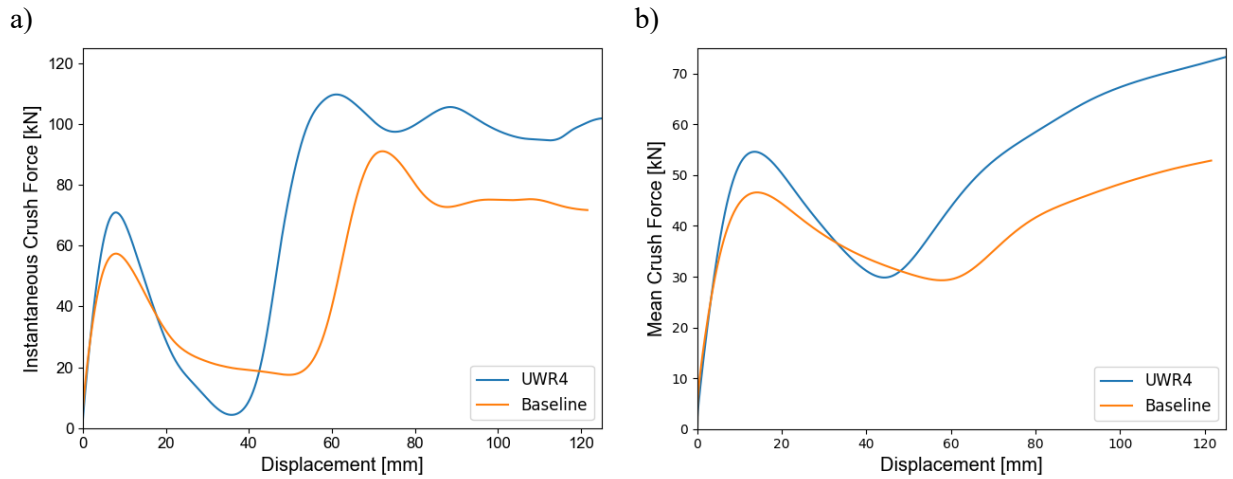
Figure 4.16: Oblique Crush Response Showing a) Instantaneous Crush Force and b) Mean Crush Force for UWR4 vs. Baseline.

4.2.2.3   Simulation Results of Detailed FE Model for Oblique Crush at Various Angles

A critical factor when considering the responses of crush rail impacts is the deformation mode. By considering oblique crush and axial crush, the present work will be able to offer greater insight into the performance of the profiles considered. Some works (e.g. [20], [35], [49], [170], [180]–[182]) consider only a single oblique impact angle and others consider multiple impact angles (e.g. refs [5]–[7], [34], [37], [46], [172], [173], [183], [184]). The additional insight gained from the additional oblique angles is often minimal unless the additional oblique angles offer new deformation modes to study. In the present work, only a single oblique angle will be used in the detailed study. This will allow the axial and oblique deformation modes to be studied in-depth without an undue increase in computational cost and complexity.

Figures 4.17 show the deformed mesh for various impact angles between 0° and 25°, confirming that there is no change in global deformation mode among the oblique impacts. Furthermore, Figure 4.18 shows the mean and peak force for the UWR4 profile for various impact angles between 0° and 25°. The mean force follows a smooth trend of decreasing as the impact angle increases. In the detailed study of the UWR4 profile, an oblique angle of 20° will be studied in addition to axial impact. In the full-vehicle crash models studied by Fender et al. [185] and Gu et al. [186], there is some rotation and limited translation of

the impacted end of the crush rails. The 20° angle was identified as having the rotation and crushing combination, which is most similar to the results seen in full-vehicle FE models.
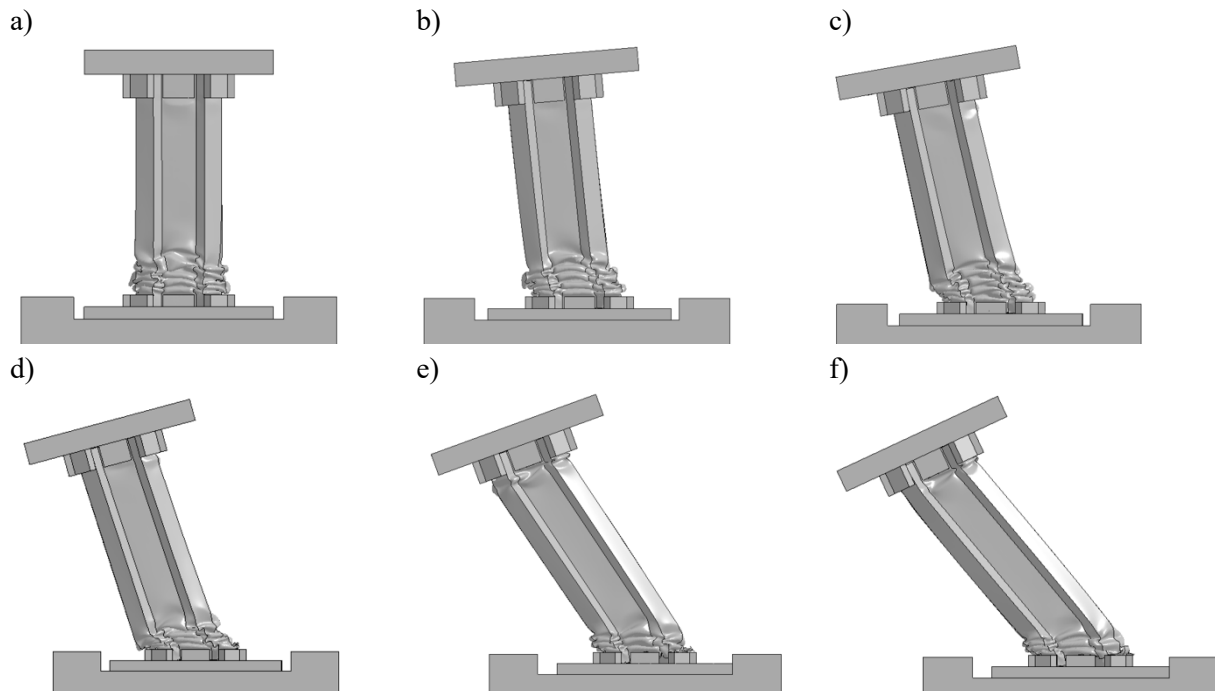
Figure 4.17: Deformed Shape of UWR4 FE Model After 125mm of Simulated Crush with Impact Angle of a) 0°, b) 5°, c) 10°, d) 15°, e) 20°, f) 25°.
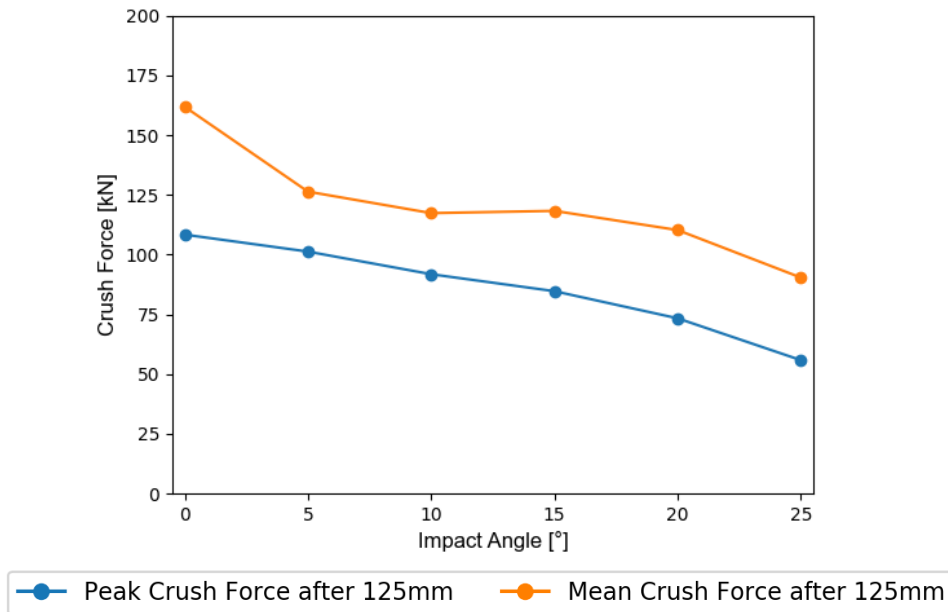
Figure 4.18: FE Model Results for UWR4 with Different Oblique Impact Angles.

4.2.3 Comparison of Axial and Oblique Performance

Figure 4.19 presents a comparison of the oblique crush response at 20° and the axial crush performance of the Baseline and UWR4 profiles. Global buckling *did not* occur, and as a result, the deformation mechanism transitions to progressive buckling in the oblique crush after the initial stage of rotation was completed. Once the profile transitioned to the progressive buckling mode, the oblique crush response returned to a level similar to the axial crush response. In general, the peak force and mean crush force for oblique crush are significantly lower than the axial crush response for both profiles.

A summary of the mean crush and peak crush force for each loading scenario of each profile is available in Table 4.6 and Table 4.7. Table 4.7 also presents the oblique impact coefficients for each profile. The Baseline profile had oblique impact coefficients of 0.70 and 0.74 for mean and peak force, respectively. The UWR4 had smaller oblique impact coefficients of 0.68 for both mean and peak crush force. Yet, the absolute performance of the UWR4 is superior to the Baseline profile for both loadings. Again, it should be emphasized that the UWR4 was originally developed for higher axial crush performance. This result highlights that an improvement in the axial crush response can lead to an improvement in the oblique crush response because of fundamental improvement in the progressive crush absorption mechanism. However, the better relative performance between axial and oblique loading (i.e. the larger oblique impact coefficient) of the Baseline compared to the UWR4 is an indicator of a trade-off between oblique and axial crush performance attributed to the cross-section profile. Thus, a multi-objective optimization study is required to investigate the sensitivity of this trade-off. Due to its higher absolute performance, the UWR4 will be the focus for the remainder of this work.

a)

b)
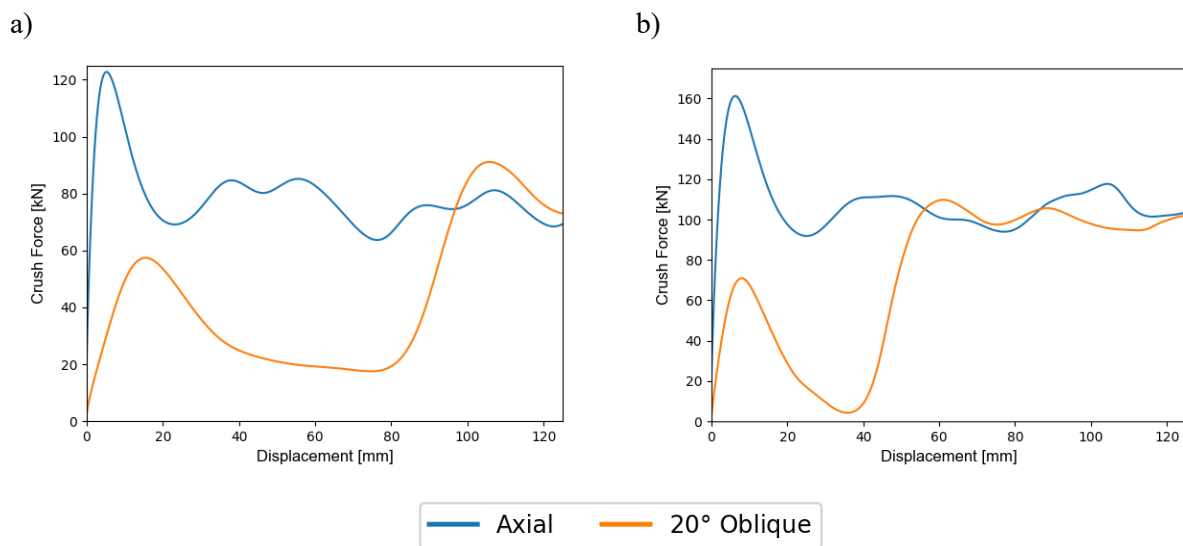
Figure 4.19: Oblique vs. Axial Force-Displacement Curves for a) Baseline and b) UWR4.

4.3　Simplified Finite Element Modelling of UWR4

In the previous section, detailed FE models were constructed to be as accurate as possible. However, an exhaustive parametric and optimization study will be performed to explore the trade-offs between the oblique and axial crush response of the UWR4. As such, the detailed FE models will be too computationally expensive to accomplish this objective. Following the strategy presented in Kohar et al. [25], a simplified FE model of the UWR4 is constructed that efficiently captures the general trends in energy absorption and deformation. This simplified FE methodology will be used for the parametric and optimization studies. The following section details the aspects of the simplified FE model of the UWR4 model.

4.3.1　Construction of Simplified FE Model

4.3.1.1　Simplifications in Geometry and Material Modelling

Figure 4.20 presents a schematic of the simplified FE model for axial and oblique crush. The first simplification is that the plates and impactors move with rigid body motion. This simplification assumes that:

- The influence of the elastic wave propagation through the bosses and impacting bodies on the crush response is negligible;
- Any deformation developed in the clamped section of the crush rail is negligible.

These components are modelled using a rigid material model (*MAT_020 in LS-Dyna). This excludes these elements from stress/strain calculations; these elements will also not affect the time step size. Only the top row of elements in the impactor is retained, and the density is increased to maintain mass. Next, the material clamped in the boss can be considered as a single rigid body affixed to the end of the rail. The bosses, plates, and sections of the crush rail that extend into the bosses have all been replaced by a rectangular plate on each end. This reduces the expense of the contact algorithm, which scales with the number of elements involved in contact. This means the actual length of the crush rail, which is modelled is decreased by the total length of the bosses. The bottom end of the crush rail is meshed contiguously with the bottom plate to create one body. The density of the bottom plate is modified to maintain the original mass of the section and components. The top plate (blue) is 200mm x 200mm and the bottom plate (green) is 205mm x 144mm. Again, all simulations of the simplified UWR4 FE model require a full model to capture the crushing folds that cross the symmetry plane and interact with each other.
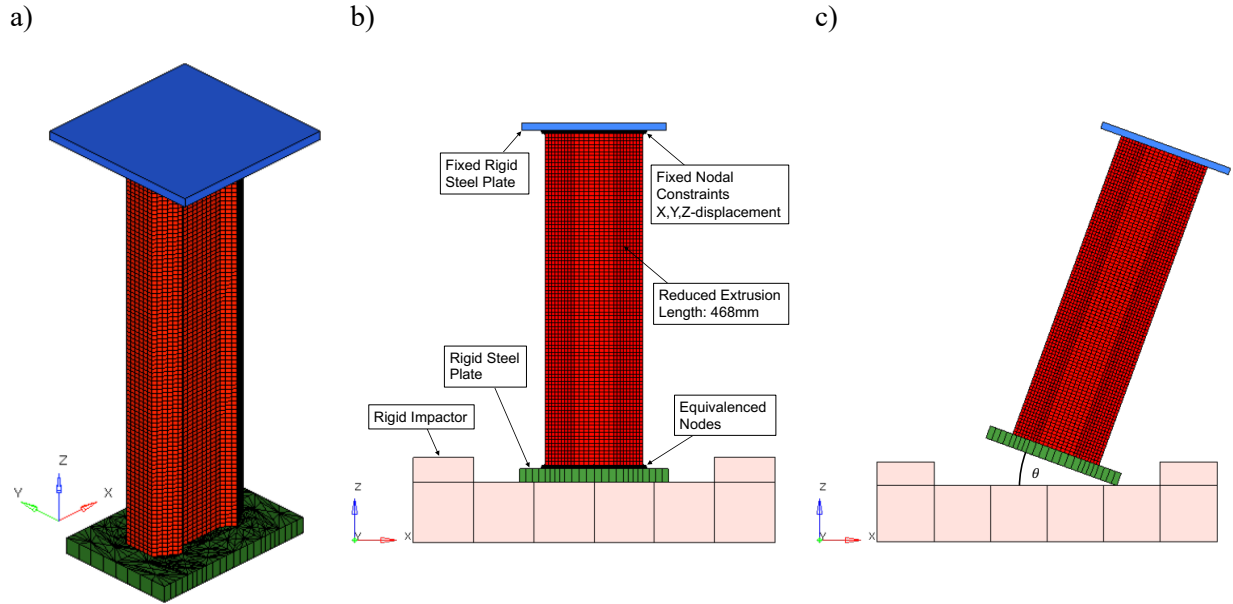
Figure 4.20: Schematic of Simplified Model Boundary Conditions for Axial and Oblique Crush.

4.3.1.2 Simplifications in Mesh

A significant portion of the computational cost is associated with calculating stress in the elements in the crush rail. This is further compounded by the time step dependence on the mesh size and the number of elements involved in contact. For these reasons, the simplified FE mesh of the crush rail used 4-node quadrilateral Belytschko-Tsay (*SECTION_SHELL *ELFORM=2) elements with a mesh size of 5mm x 5mm with 3 through-thickness integration points. This increase in mesh size is consistent with element sizes used in the literature (e.g. [14], [16], [17], [25], [45], [49], [187]–[190]).

The plate mesh is also simplified with a single layer of extruded triangular (pentahedral) elements. Figure 4.21 presents a schematic of the simplified plate mesh with the outline of the crush rail highlighting how the plate mesh connects to the crush rail mesh. The plate was meshed to remain in continuous connection with the crush rail. Since it connects to the shell element of the crush rail, solid elements with rotational degrees of freedom are used (*SECTION_SOLID *ELFORM=3 in LS-Dyna). Since the plate utilizes a rigid material formulation, the mesh quality in the plate is a minor issue. Every sample in the parametric study will require its own plate mesh; a triangular mesh was chosen to facilitate the generation of these meshes.
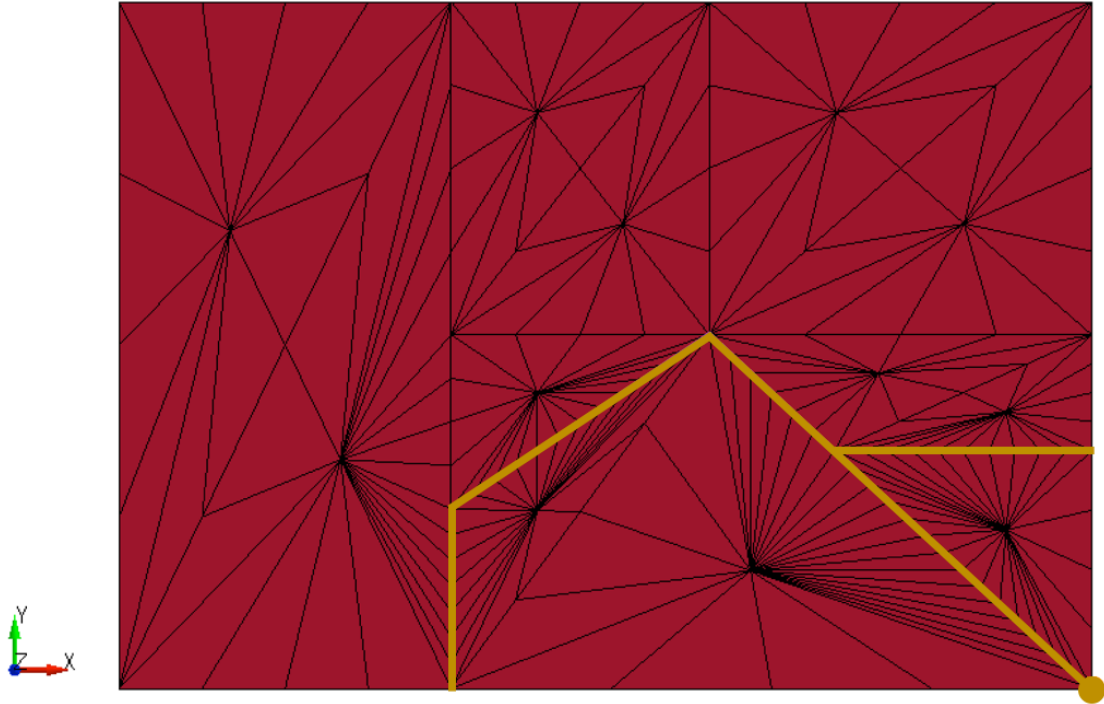
Figure 4.21: Quarter of the End Plate for Simplified FE Model.

4.3.1.3 Simplifications in Boundary Conditions and Contact

The boundary conditions of the simplified FE model follow a similar construction to the detailed FE model. However, the top plate nodes (green) are fixed in space to serve as a surface for contact. Self-contact with the same parameters is applied to the crush rail/bottom plate assembly. One-way contact is applied between the crush rail (slave) and top plate (master) and between the bottom plate (slave) and impactor (master). Defining the slave/master relationship for the finer/coarser meshes in this manner minimizes errors in contact definition.

4.3.2 Analysis of the Simplified FE Model

4.3.2.1 Verification of Simplified FE Model Setup

In Section 4.1.3.1, the importance of checking the energy balance of the simulations was discussed. Figure 4.22 shows the energy balance for the simplified model in both axial and oblique impacts. This result shows that the total energy is not significantly changing in these simplified FE models. There is a negligible amount of hourglass energy and appears to have better energy control than the detailed models discussed in Sections 4.1.3.1 and 4.2.2.1. The reason for this can be determined by inspecting the distribution of hourglass energy in the meshes, as in Figure 4.23. It can be seen that significant hourglassing occurs in and around the sections of the crush rail that the bosses clamp. The simplified model assumes this material is

86

rigid, which prevents hourglassing. Overall, the simplified model is verified to be free of numerical instabilities or anomalies.

a)   b)
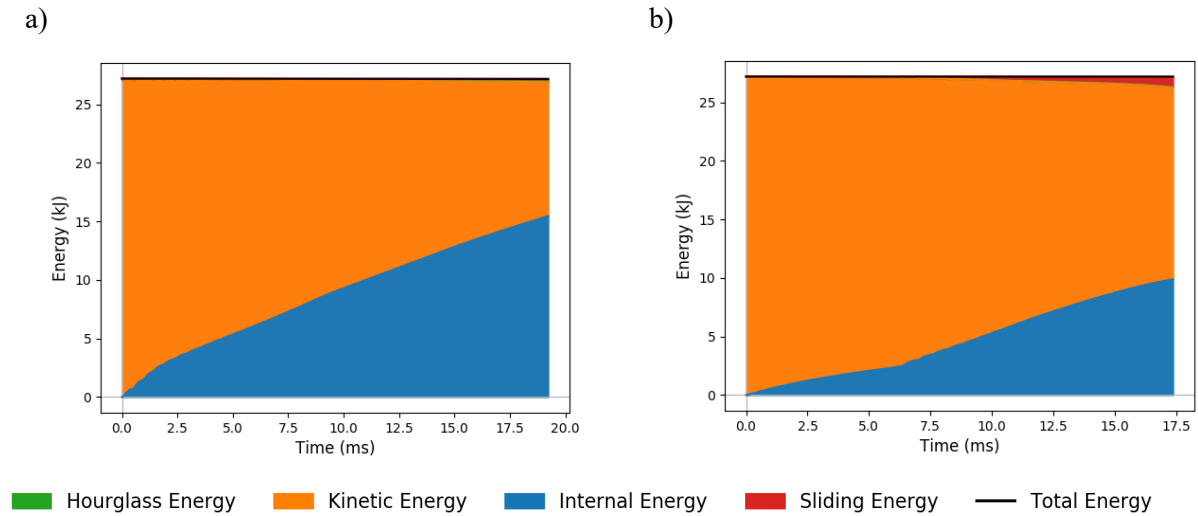
Figure 4.22: Energy Balance For Simplified a) Axial and b) 20° Oblique FE Models.

a)   b)
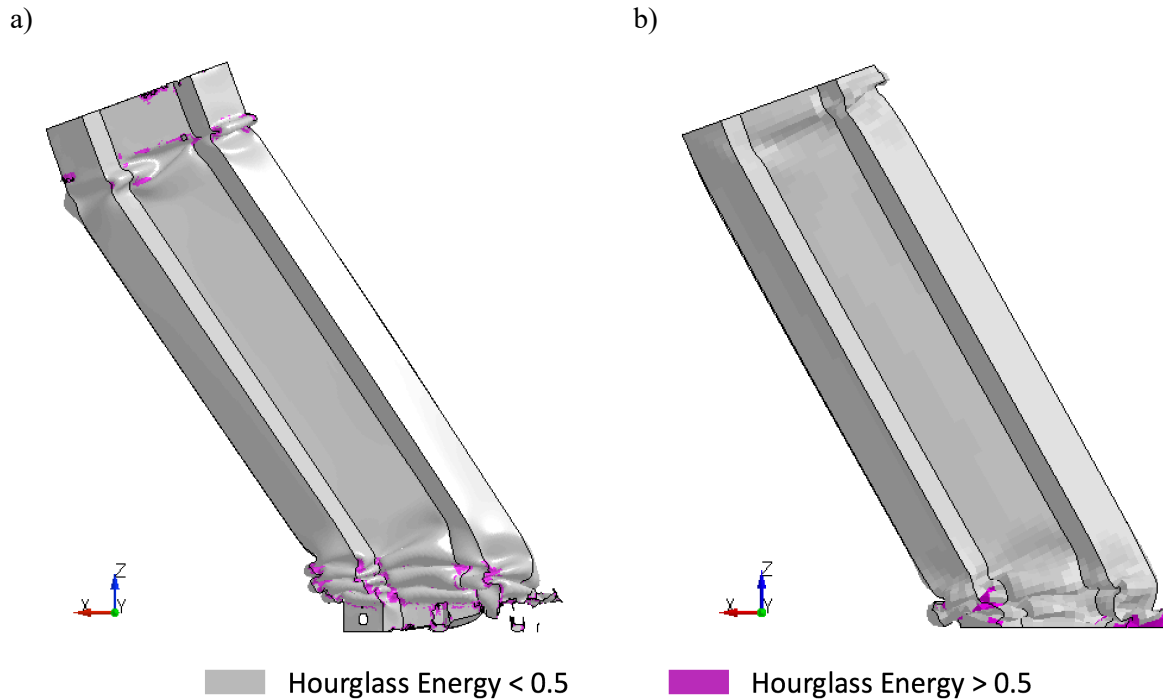
Figure 4.23: Hourglass Energy in UWR4 20° Impact, a) Detailed Model, and b) Simplified Model.

4.3.2.2   Comparison of Simplified FE Model with Detailed FE Model

Table 4.8 presents the computational resources required for each FE simulation. The simplified FE model is ~700x more computationally efficient than the detailed FE models.

Table 4.8: Computational Time Required for the Detailed and Simplified UWR4 Models.

	Axial Crush			Oblique Crush		
	# cpus	Time [Hrs]	Core Hours # cpus × Time [Hrs]	# cpus	Time [Hrs]	Core Hours # cpus × Time [Hrs]
UWR4 – Detailed	72	16.3	1173.6	64	16.4	1049.6
UWR4 – Simplified	8	0.216	1.73	8	0.183	1.46

Figure 4.24 and Table 4.9 present a comparison of the experimental result for the UWR4 with the two FE modelling techniques. The simplified model tends to over-predict the peak crush (+4.1%) and mean crush force (+2.5%) for both loading conditions. This is caused by the reduction in the length of the crush rail and constraining the plates to the crush rail. However, the simplified model captures similar crush behaviours and the trends observed in force-displacement response as the detailed models. Overall, the construction of the simplified is suitable for use in the parametric and optimization studies.
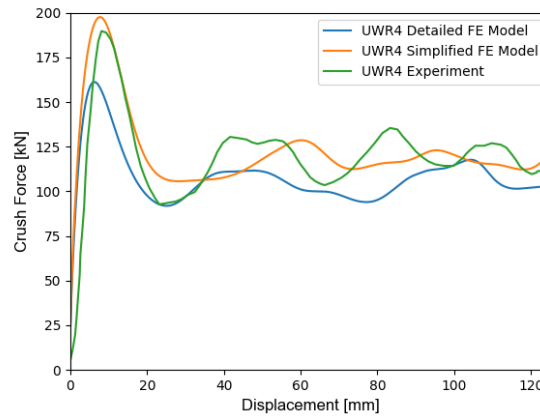
Figure 4.24: Comparison of Crush Force Response of UWR4 Experiment, UWR4 Detailed FE, and UWR4 Simplified FE.

Table 4.9: Comparison of energy absorption metrics for simplified UWR4 FE model for axial and oblique crush.

	Axial Crushing			Oblique Crushing				
	F_{mean}^{axial} [kN]	F_{peak}^{axial} [kN]	η^{axial}	$F_{mean}^{oblique}$ [kN]	$F_{peak}^{oblique}$ [kN]	$\eta^{oblique}$	λ_{mean}	λ_{peak}
Simplified FE Model	122.5	197.5	0.62	85.2	118.5	0.72	0.69	0.60
Δϵ Detailed to Simplified Model (%)	+13.0	+22.5	-4.2	-15.9	+7.9	+5.0	+1.7	+2.1
Δϵ Exp. to Simplified Model (%)	+2.5	+4.1	-1.0	--	--		--	--

5   PARAMETRIC STUDY

As discussed in Section 4.2.2.2, there was a trade-off between the relative axial and oblique crush performance for the UWR4 profile associated with geometry. This section presents a parametric study that varies geometric features of the UWR4 profile's cross-section to explore the trade-off in energy absorption characteristics. This parametric study will explore trends regarding the axial and oblique mean force, axial and oblique crush efficiency, and the oblique impact coefficient. A full factorial design of experiments was used to exhaust the domain of interest based on the geometry's defined parameters. Although a full factorial design of experiments is computationally expensive, it will truly identify optimal configurations based on the domain of interest, sample resolution, and constraints for performance. It will also establish a benchmark for comparing intelligent sampling and optimization schemes, such as the response surface methodology, in determining optimal configurations.

5.1   Setup of Parametric Study

Figure 5.1 presents a schematic of the parametric design space. The cross-section was parameterized using six geometric points (labelled A to F in Figure 5.1) while maintaining quarter-symmetry. Table 5.1 summarizes the geometric constraints used for the shape-morphing parametric study. Point D was defined as the point of quarter-symmetry for the geometry. The x-coordinate of Point A and z-coordinate of Point F remained at 0.00 to enforce quarter symmetry. The z-coordinate of Point A and the x-coordinate of Point C were fixed to ensure that each design had a similar packaging envelope [24]. A constraint was imposed on Point B, such that segment AB was parallel to the x-axis (constant z-coordinate). Similarly, the x-coordinate of Point E was constrained to enforce that segment EF remained parallel to the z-axis. An additional constraint was imposed to enforce that segment DE and EF remained colinear. These constraints are imposed on the study to promote lightweight designs that are extrudable [24]. As a result, three points (Points B, C, F) have their position varied by some amount, q_i, from their initial positions in their direction of freedom. The parameters varied according to $q_1 \in [-15, 10]$ with $\Delta q_1 = 1$, $q_2 \in [-30, 25]$ with $\Delta q_2 = 2.5$, and $q_3 \in [-10, 5]$ with $\Delta q_3 = 1$, where $\mathbf{q}$ are in units of millimetres. Figure 5.1 also shows the $\mathbf{q} = 0.0$ base case and the extreme values of the design space. These are the designs that have various combinations of the maximum/minimum values of the parameters. Each design enforced a uniform wall thickness throughout the profile. This wall thickness was calculated for each profile such that all profiles have the same mass as the original UWR4 profile (1.4kg). Each geometry was simulated for impact angles of 0 and 20 degrees using the simplified FE modelling approach outlined in Section 4. A full factorial design of experiments was used to generate a total of 9,568 unique designs. This required a total of 19,136 finite element simulations to be performed that utilized 30,522 core-hours (average of 3.19 core-

hours per design). The axial mean force, axial peak force, axial crush efficiency, oblique mean force, oblique peak force, oblique crush efficiency, and oblique impact coefficient were calculated for all profiles in the study.
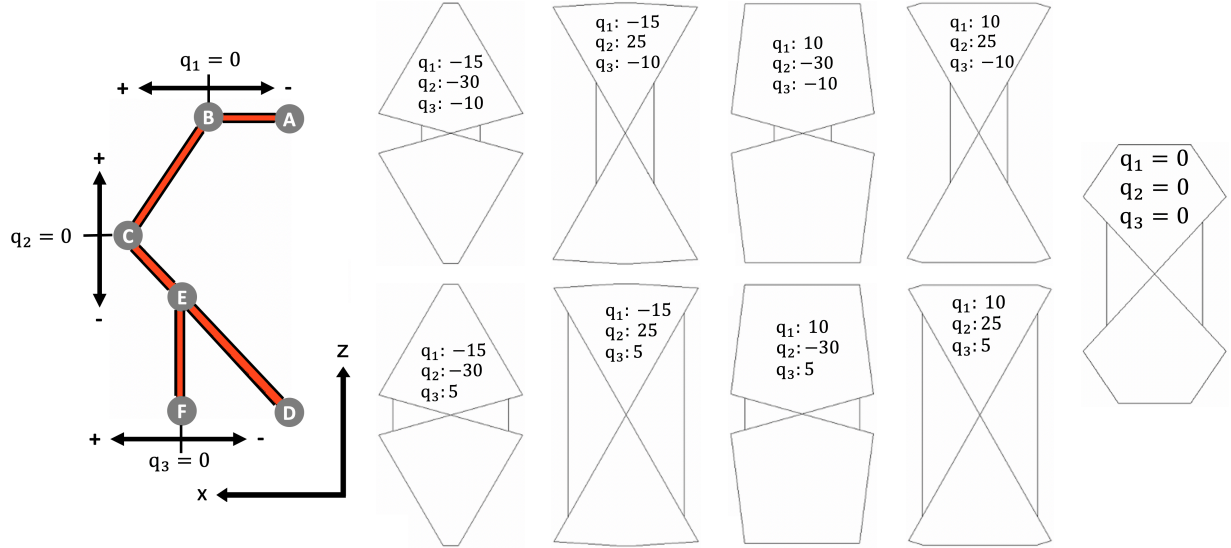
Figure 5.1: Parametric Design Space.

Table 5.1: Constraints in Parameterizing the UWR4 Geometry.

Point	X-Coordinate [mm]	Z-Coordinate [mm]
$A(x, z)$	0.000	67.500
$B(x, z)$	$18.880 + q_1$	67.500
$C(x, z)$	37.100	$20.350 + q_2$
$D(x, z)$	0.000	0.000
$E(x, z)$	$24.975 + q_3$	$\left(\dfrac{20.350 + q_2}{37.100}\right)(24.975 + q_3)$
$F(x, z)$	$24.975 + q_3$	0.000

5.2   Analysis of Parametric Study

Figure 5.2 presents a scatter plot of the simulation results of the axial and oblique mean force, axial and oblique crush efficiency, and the oblique impact coefficient with respect to each design variable, q_i. The energy absorption characteristics of the UWR4 profile are also presented for reference. Since the data is multi-dimensional, the plots are coloured by point density using a Gaussian kernel density estimator (Silverman [191]). This representation helps provide insight into the relationship between energy absorption characteristics and design variables. The high-density regions within the point clouds show distinct trends

90

in the relationships between the objectives and the design variables. It should be noted that the performance of the baseline value of $\mathbf{q} = 0$ generally lies within the regions of the highest density for energy absorption. There is still significant variance in all objectives, which indicates that there is potential for improving performance. Yet, no single parameter alone correlates to improved performance, and there is no single point that is optimal for all objectives.

Figure 5.3 presents the correlation between the oblique mean force, axial crush efficiency, and oblique impact coefficient with respect to the axial mean force using the Gaussian kernel density function for the parametric study. The oblique mean force follows an approximately linear relationship with respect to the axial mean force, with some variation along with an increase in axial mean force. This deviation from this linear result is a higher-order secondary effect of the geometry that contributes to the enhancement or reduction of the oblique mean force. The axial mean force generally follows an approximate linear relationship with respect to the axial crush efficiency, as observed in Kohar et al. [109]. This result is generated by the cross-sectional area remaining constant through the constraint on the length and mass of the crush rail. A similar amount of variation in the crush efficiency is observed with an increase in the axial mean force, representing an opportunity for optimization. However, a large cluster of samples with high crush efficiency and low axial mean force deviated from this linear relationship; these were samples that had unusually low peak force due to a geometrical interaction between sections. Yet, the axial crush efficiency in this region of low axial mean force can be comparable to samples with a high mean crush force and cannot be uniquely distinguished. It should be noted that this cluster of low axial mean force is generally lower than the baseline configuration ($\mathbf{q} = 0$). The oblique impact coefficient broadly follows the trend of remaining relatively constant at a value of 0.6936. This results from the relatively linear relationship between axial and oblique mean force, where the oblique impact coefficient is the proportionality factor between these two measurements. The outlying group of large values of the oblique impact coefficient again represent structures where global buckling was present in the axial crush simulations. This poses an interesting challenge for evaluating designs with respect to oblique impact coefficient. Although a higher oblique impact coefficient can be an indicator for less sensitivity to oblique loading, it can also indicate a tendency for global buckling. Further analysis using an intelligent optimization strategy can give insight into the trade-off of these conflicting performance objectives.
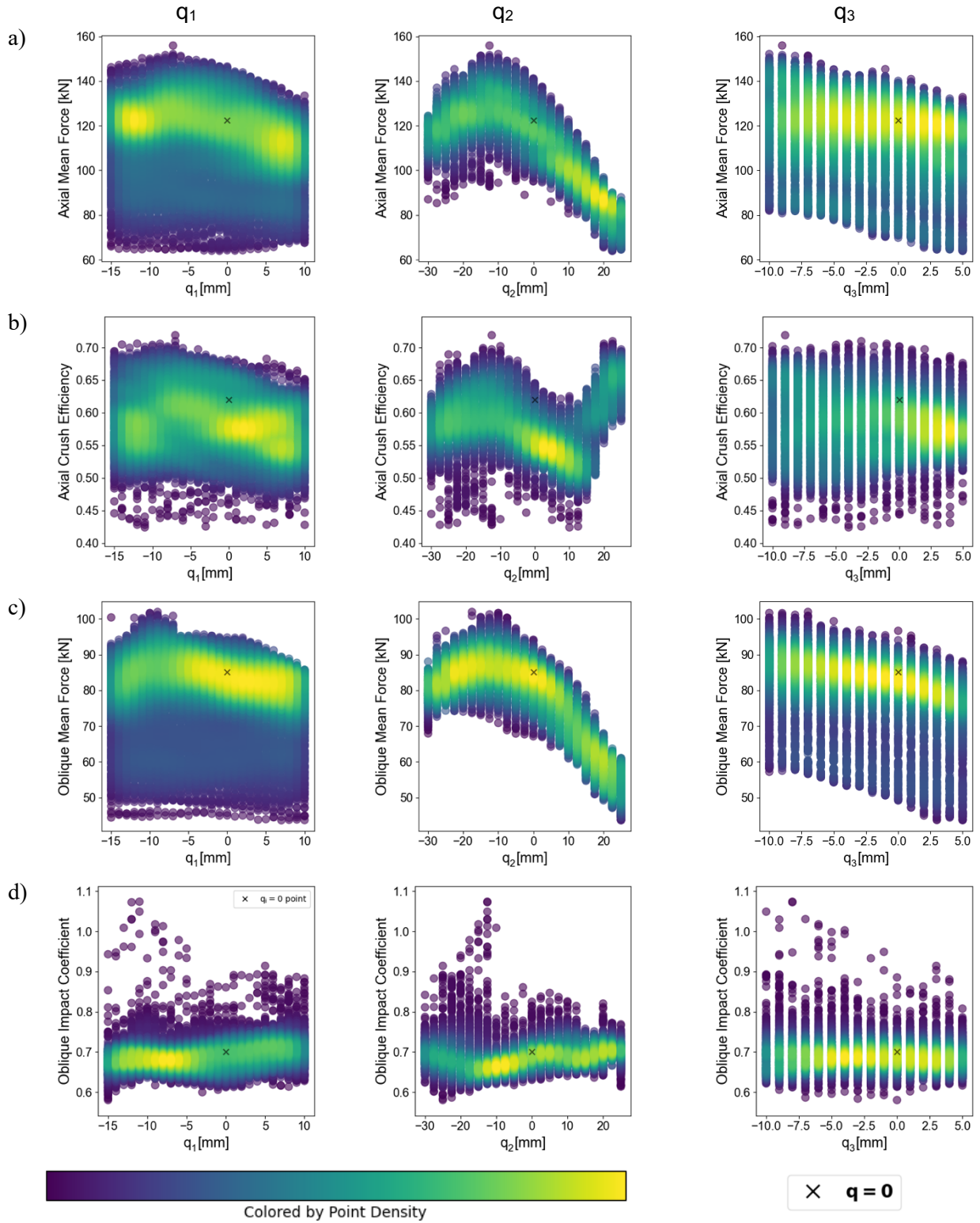
Figure 5.2: a) Axial Mean Force, b) Axial Crush Efficiency, c) Oblique Mean Force, and d) Oblique Impact Coefficient vs. the Design Parameters q.
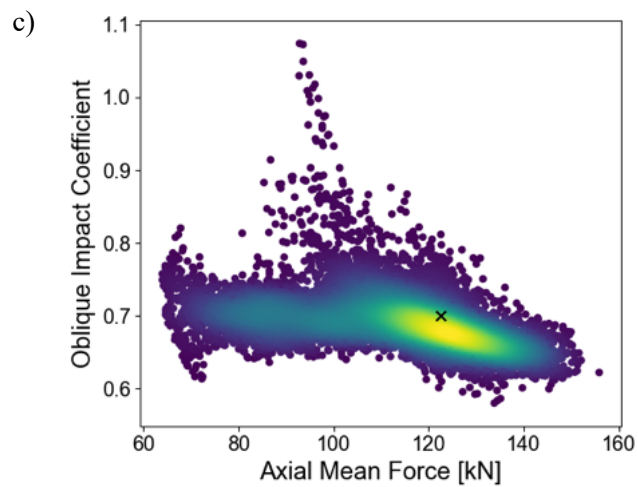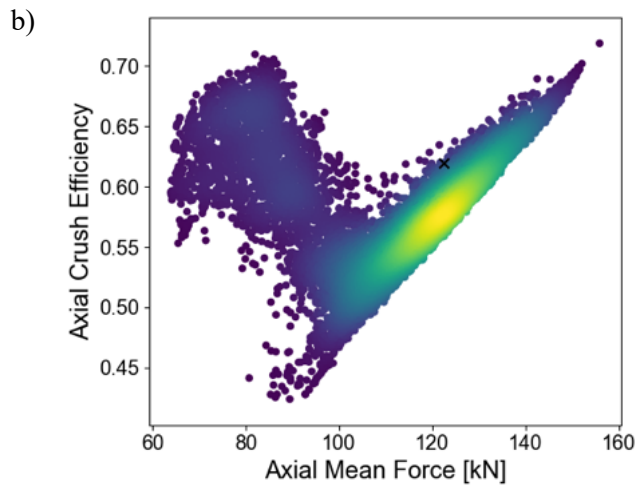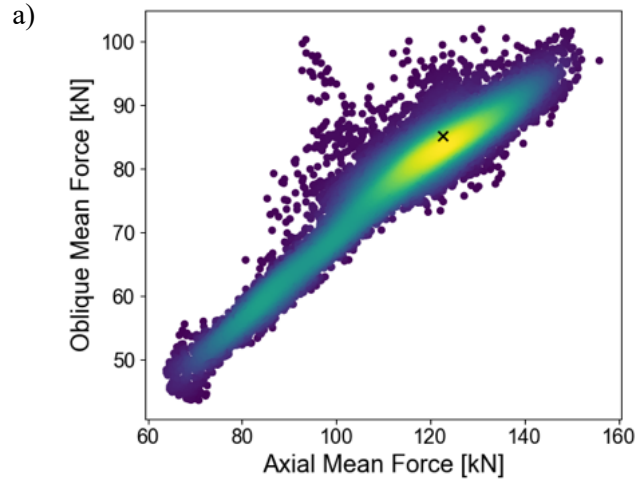
Figure 5.3: Correlation between Axial Mean Force and a) Oblique mean force, b) Axial Crush Efficiency, and c) Oblique Impact Coefficient.

6 FORMULATION OF OPTIMIZATION PROBLEM

This section formulates the optimization problem that was conducted in this study. In vehicle crashworthiness design, the crush rails should absorb as much energy as possible while limiting the peak force which the rail can produce [192]. The axial and oblique mean forces should be as high as possible to maximize energy absorption under axial and oblique loading. Furthermore, the oblique impact coefficient, which can be thought of as representing the design's sensitivity to oblique loading, should be as high as possible, lending confidence to the ability of the crush rail design to have good performance in a range of loading angles. To address the peak force requirement, axial crush efficiency is also introduced as a performance metric. Maximization of axial crush efficiency is preferred over minimization of peak force because designs with high crush efficiency will inherently tend to have good energy absorption qualities, while designs with low peak force do not. Oblique crush efficiency does not need to be considered, as the axial case will exhibit the highest peak forces developed by the crush rail. To this end, several criteria and constraints were used to formulate the optimization problem for this study:

1. The objectives of this study are to maximize the axial and oblique mean force, along with the axial crush efficiency and oblique impact coefficient.
2. All acceptable designs must have energy absorption characteristics (i.e., axial and oblique mean force, crush efficiency, oblique impact coefficient) that outperform the performance measured in the baseline UWR4.
3. The variations in the geometry must follow the parametric definitions outlined in Section 5. A constant mass of 1.4kg was used to ensure that no design would be heavier/lighter than the baseline UWR4 profile. This also allows the utilization of the results from the parametric study in Section 5.2.

Hence, the optimization problem is formulated as follows:

$$
\begin{aligned}
& \text{Max} \left(F_{mean}^{axial}, F_{mean}^{oblique}, \eta_{axial}, \lambda_{mean} \right) \\
& F_{mean}^{axial} \geq 122.5 \text{ kN} \\
& F_{mean}^{oblique} \geq 85.2 \text{ kN} \\
& \eta^{axial} \geq 0.620 \\
& \lambda_{mean} \geq 0.696 \\
& q_1 \in [-15, 10], \Delta q_1 = 1.0 \\
& q_2 \in [-30, 25], \Delta q_2 = 2.5 \\
& q_3 \in [-10, 5], \Delta q_3 = 1.0 \\
& s.t. \text{ Mass} = 1.4 \text{kg}
\end{aligned}
\tag{6.1}
$$

This is a multi-objective optimization problem with the assumption of four independent objective functions. Although crush mechanics dictates strong first-order dependencies between the oblique mean force, crush

efficiency, and oblique impact coefficient with respect to the axial mean force, the higher-order variations in these responses can create a potential trade-off with respect to each energy absorption characteristic. Therefore, there may be a Pareto front instead of a single optimum design. However, if the degree of the higher-order variations are minor, then the multi-objective optimization problem can collapse down to an approximate single-objective optimization study where the Pareto front is a single point. It is important to note that this relationship between the objectives is typically unknown prior to the optimization study. Nevertheless, the criteria and constraints that define the optimization study can be applied to the complete parametric study to identify the true optimal configurations and the Pareto front, which can be used to evaluate the suitability of multi-objective optimization schemes.

6.1 True Solution to the Multi-Objective Optimization Problem

Figure 6.1 presents the combinations of design parameters, $\mathbf{q}$, from the parametric study that dominates the baseline UWR4. In total, 35 out of the 9,568 different combinations of design parameters dominated the performance of the UWR4. Next, a non-dominated sorting algorithm (NSGA-II) from Deb et al. [157] was applied to all of the designs in the design space to create a Pareto front. Figure 6.1 also presents the corresponding Pareto front that satisfies the constraints presented in Equation 6.1. There were a total of 118 of 9,568 that lay on the Pareto front. These designs represent the total span in the spread of the designs that deviate from the theoretical idealized linear relationships between axial and oblique crush force, crush efficiency, and oblique impact coefficient. However, only 9 out of 9,568 were both on the Pareto front and dominated the performance of the original UWR4 design, which formed a constrained Pareto front. This set represents the solution to the multi-objective optimization problem, with at least 7.1% - 16.7% and 7.9% - 17.0% improvement in axial and oblique crush force, respectively, for this study. Table 6.1 presents the design parameters and their corresponding energy absorption characteristics for the solutions on the constrained Pareto front. A corresponding overlay of the geometries on the constrained Pareto front is presented in Figure 6.2. The design parameters that form the unconstrained and constrained Pareto front sets are well confined to a local region within the design space through the defined performance constraints.

Figure 6.3 presents the correlation between the axial mean force with the oblique mean force, axial crush efficiency, and oblique impact coefficient with the unconstrained and constrained Pareto front solutions. The optimization problem constraints are also superimposed in Figure 6.3. A narrow region within the upper left quadrants is formed by the performance criteria that reduce the design domain to the well-confined region. As such, the Pareto front is narrow and confined to a relatively small region in the design domain. Nevertheless, there is still some sensitivity in the trade-off with respect to each objective

function. The variation in F_{mean}^{axial}, $F_{mean}^{oblique}$, η^{axial}, and λ_{mean} are $\pm4.30\%$, $\pm4.47\%$, $\pm2.41\%$ and $\pm2.92\%$, respectively. It is also important to note that the solution with the highest axial mean force is not on the constrained Pareto front because of the minimum oblique impact coefficient constraint. Likewise, the solution with the highest mean oblique crush force is not on the constrained Pareto front due to the minimum crush efficiency constraint.
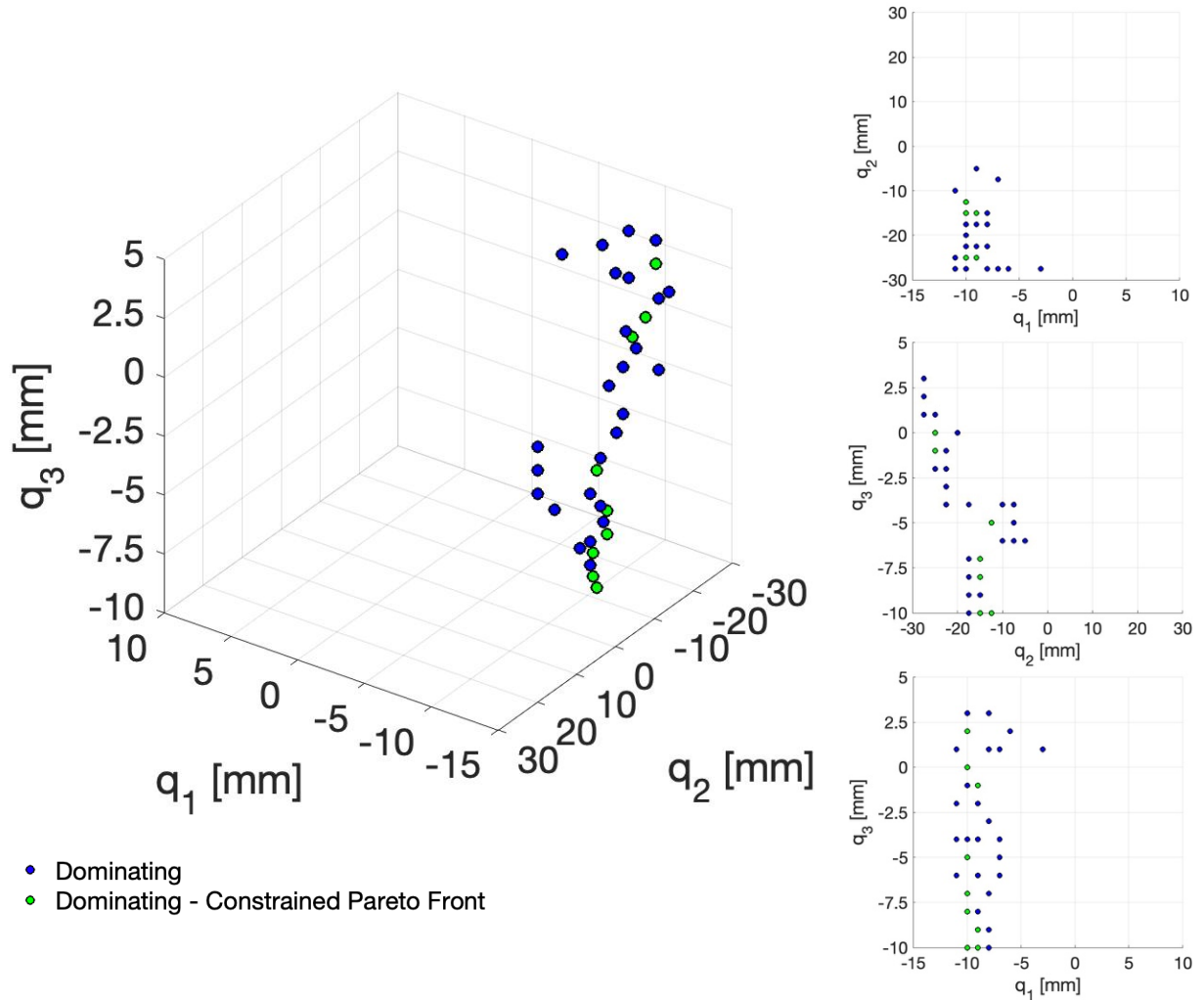
Figure 6.1: Solution Space and Constrained Pareto Front that Dominates the Original UWR4.

Table 6.1: Constrained Pareto Front Designs.

				Pareto Front Results				Compared to Original UWR4			
	q_1 [mm]	q_2 [mm]	q_3 [mm]	F_{mean}^{axial} [kN]	$F_{mean}^{oblique}$ [kN]	η^{axial}	λ_{mean}	F_{mean}^{axial} [%]	$F_{mean}^{oblique}$ [%]	η^{axial} [%]	λ_{mean} [%]
A	-10.0	-27.5	2.0	131.2	92.0	0.648	0.701	7.1	7.9	4.5	0.8
B	-10.0	-25.0	0.0	132.1	96.7	0.645	0.732	7.8	13.5	4.0	5.2
C	-9.0	-25.0	-1.0	132.6	92.6	0.648	0.698	8.3	8.7	4.4	0.4
D	-10.0	-15.0	-8.0	135.8	98.2	0.628	0.723	10.9	15.2	1.3	3.9
E	-9.0	-15.0	-9.0	136.1	**100.6**	0.628	**0.739**	11.1	18.0	1.2	6.3
F	-10.0	-12.5	-5.0	138.5	99.4	0.640	0.717	13.1	16.6	3.2	3.1
G	-10.0	-15.0	-7.0	139.3	99.0	0.644	0.711	13.7	16.2	3.7	2.2
H	-9.0	-15.0	-10.0	140.4	98.6	0.647	0.702	14.6	15.7	4.3	1.0
I	-10.0	-12.5	-10.0	**143.0**	99.7	**0.659**	0.697	16.7	17.0	6.3	0.3
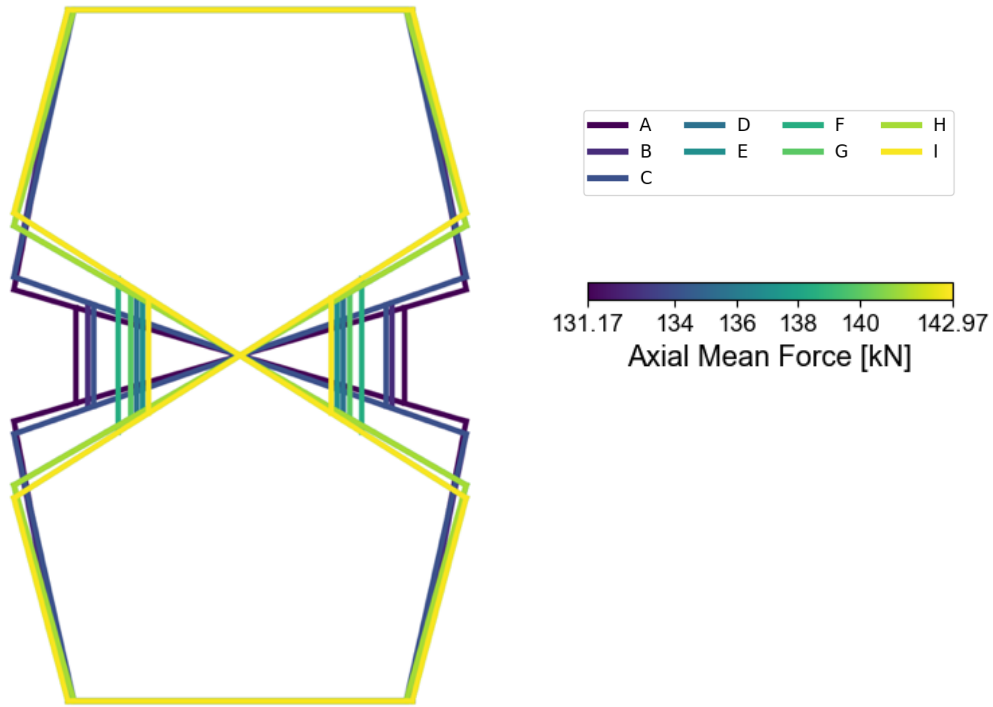
Figure 6.2: Overlay of Shapes from Constrained Pareto Front.
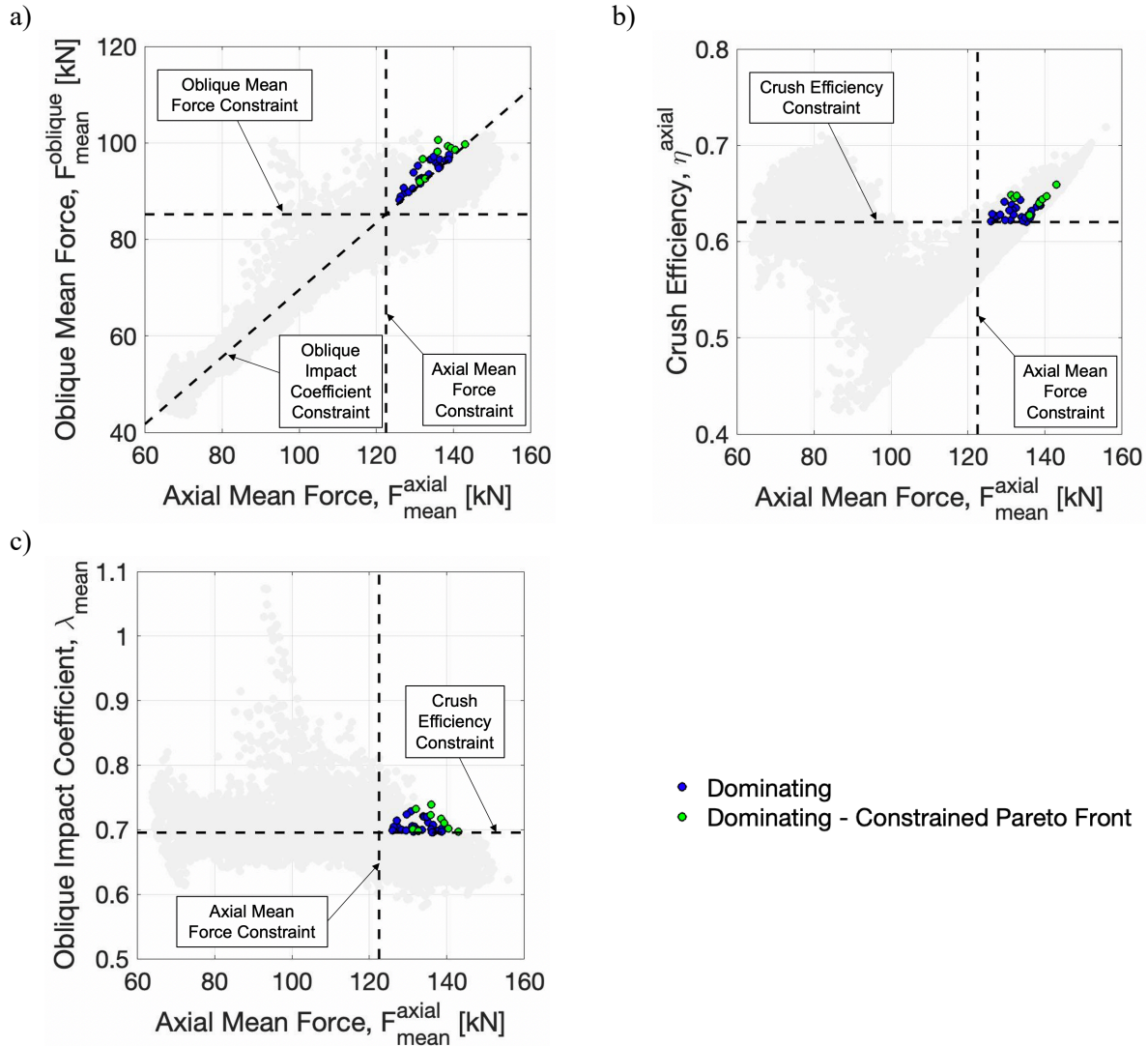
Figure 6.3: Correlation between Axial Mean Force and a) Oblique Mean Force, b) Axial Crush Efficiency, and c) Oblique Impact Coefficient with Dominating and Pareto Front Solutions.

7 OPTIMIZATION USING RESPONSE SURFACE METHODOLOGY

The parametric study presented in Section 6.1 showed that a significant improvement in the axial and oblique crush force could be achieved over the baseline UWR4 response. Furthermore, the parametric study highlighted a Pareto front with a meaningful trade-off between the different energy absorption objectives. However, simulating 9,568 unique designs, which required 30,522 core-hours of CPU time, can be potentially cost-prohibitive to a designer in a practical setting. This barrier can be compounded if additional design parameters or impact angles need to be considered. Therefore, intelligent strategies, such as the response surface methodology (RSM), that can efficiently navigate the design space to identify these Pareto fronts of optimum performance and trade-off are required. However, the true potential of RSM in its ability to identify the true Pareto front in many applications of structural crashworthiness is often not explored. Since the parametric study was performed, the computationally expensive task of performing the FE calculations has already been completed. Therefore, this study provides a rare opportunity to evaluate traditional RSM's suitability in obtaining the true Pareto front for various configurations.

7.1 Traditional Response Surface Methodology Studies

7.1.1 Setup of Traditional RSM Studies

The traditional RSM approach presented in Section 2.4.1 was implemented into a custom program using the Scikit-learn [193], DEAP [194], and Diversipy [195] libraries in Python. As described in Section 2.4.1.1, the maximin algorithm was chosen because it maintains strong diversity of the samples, it is easy to iteratively update with new points while maintaining diversity and avoiding duplicates, and it can sample from irregular domains. It is also very well-suited for discrete data. The initial point was seeded with the $\mathbf{q} = 0$ point. The FNN was chosen as the metamodel for its ability to capture very complex functionality. A comparison of metamodel techniques is provided in Section 2.4.1.2.6, and a description of the neural network technique is given in Section 2.4.1.2.4. After performing a small hyperparameter study, the network architecture used in this work was chosen to comprise of an input layer, two fully connected hidden dense layers consisting of 8 and 4 neurons, respectively, and an output layer. All hidden neurons utilized the Tanh(x) activation function. The initial parameters in each FNN were randomly initialized and trained using the L-BFGS [196] (described in Section 2.4.1.3.1) optimizer to minimize the MSE function. L-BFGS is chosen for its fast convergence and because the size of the network/training data is small enough that there are no scaling issues. On each iteration of the RSM after the first, the previous iteration's network weights were used as the initial values for the network training. An L2-regularization with a value of 0.001 was used to penalize large network parameters during the training process. No metamodel was used for the

prediction of the oblique impact coefficient values. Instead, the predicted value was computed based on the predicted values of axial mean force and oblique mean force.

During the training stage, 85% of all samples in the DOI were randomly sampled to calibrate the FNN. In comparison, the remaining 15% was used as a validation set to determine if the training had saturated. Each FNN was trained for 1000 epochs or until the MSE function was below a tolerance of 0.0001. The NSGA-II [157] algorithm was chosen for its strong ability to perform global multi-objective optimization. A comparison of optimization techniques is given in Section 2.4.1.3.5. The implementation in this work utilized 300 generations with a population size of 200. The simulated binary crossover and mutation operators available in the DEAP library were used, with a crossover probability of 0.85, mutation probability of 0.6, and distribution indices of 0. The binary tournament selection presented by Deb et al. [157] was used. A description of the algorithm is available in Section 2.4.1.3.4.

The sampling rate, N, was varied according to $N = 25 \times 2^i$ with $0 \leq i \leq 4$ to explore the convergence speed and accuracy of the framework. As mentioned earlier, the parametric study performed in Section 6.1 provides a unique opportunity to critically evaluate the accuracy of this framework in obtaining the true Pareto front. It should be emphasized that the RSM approach has no knowledge of the true Pareto front that was obtained in Table 6.1; this technique is only used as a post-mortem analysis of each configuration. A test score metric is used to evaluate the accuracy of each configuration. The test score metric, M_{test}, simply evaluates the number of unique solutions generated by the NSGA-II, known as $\mathbb{Y}^{NSGA-II}$, that intersects with the true Pareto front ($\mathbb{Y}^{true}$), which is defined as

$$M_{test} = \frac{n\left(\mathbb{Y}^{NSGA-II} \cap \mathbb{Y}^{true}\right)}{n(\mathbb{Y}^{true})} \times 100\% \tag{7.1}$$

This metric provides a strict evaluation of the RSM method as a true or false examination and gives no credit to solutions near the true Pareto front; this provides some intuition into the significance of the value. Each RSM configuration was repeated ten times to obtain a statistically representative response. The iteration scheme terminated when the metamodel accuracy satisfied $\epsilon^{err} \leq \epsilon^{err}_{tol} = 3\%$, and then continued to satisfy this criterion for consecutive iterations until 100 additional points were sampled. This corresponds to 5 iterations in a row for $N = 25$, 3 iterations in a row for a sampling rate of $N = 50$, and 2 iterations in a row for $N = 100, 200$ and 400. This simulates the traditional approach utilized in literature and practice. However, each configuration was allowed to iterate until 6000 simulations were sampled to investigate the method's continuous improvement after satisfying the termination criteria.

7.1.2 Results and Discussion of Traditional RSM Studies

Figure 7.1 and Table 7.1 present a summary of the results from the traditional RSM studies. The results of the traditional RSM studies highlighted a key deficiency in achieving the true Pareto front. Each RSM approach terminated within the first 125-800 simulations, which corresponds to approximately 1.3-8.4% of the total domain of interest. The post-mortem analysis of the performance metric showed that the traditional RSM approach is on average identifying 0.95 ± 0.94 out of 9 designs ($10.5\% \pm 10.4\%$) on the true Pareto front. In many instances, the traditional RSM approach terminates far too early after satisfying the metamodel accuracy criterion. There is some noticeable variation in each trial due to the optimization results converging to different solutions.

Table 7.1: Summary of Results for Traditional RSM Studies.

Samples / Iteration	25	50	100	200	400
Average Num. Samples	125	150	200	400	800
Average Test Score, M_{test}	0.08	0.13	0.14	0.10	0.08
Standard Dev., M_{test}	0.11	0.11	0.11	0.09	0.10

6000 Samples					
Samples / Iteration	25	50	100	200	400
Average Test Score, M_{test}	0.889	0.933	0.944	1.0	0.978
Standard Dev., M_{test}	0.099	0.089	0.075	0.0	0.067

After iterating beyond the metamodel accuracy criteria, the test score metric started to improve towards the true Pareto front gradually. After 6,000 simulations, the traditional RSM approach achieved a score of 8.54 ± 0.59 out of 9 designs ($94.8\% \pm 6.6\%$), and the variation improves. This is the natural result of higher sampling density statistically finding the Pareto front. Although 6,000 simulations is a reduction to 63% of the total domain, this can still be cost-prohibitive for optimization problems with more design parameters and load cases. The sampling rate appears to have little to no effect on the metamodel accuracy. Further metamodel hyperparameter studies can be performed to confirm this result. This study also shows that the sampling rate has little to no impact on the rate and overall convergence of the traditional RSM performance. This results from no information about the metamodel error being used in seeding the next generation in regions of higher error. More importantly, there is no guidance in seeding new samples around an optimum because the optimization operation is performed "out-of-loop" after the metamodel accuracy is achieved. The greedy minimax algorithm for domain sampling would continue to seed the entire DOI, including regions with good metamodel predictive capabilities that would show low energy absorption performance. Incorporating the optimization scheme during the iteration stage to aid in the next iteration sampling can improve accuracy and convergence speed. The use of the Adaptive Surrogate-Assisted Response Surface Methodology (ASA-RSM) [23], as discussed in Section 2.4.2.1, will facilitate this goal.
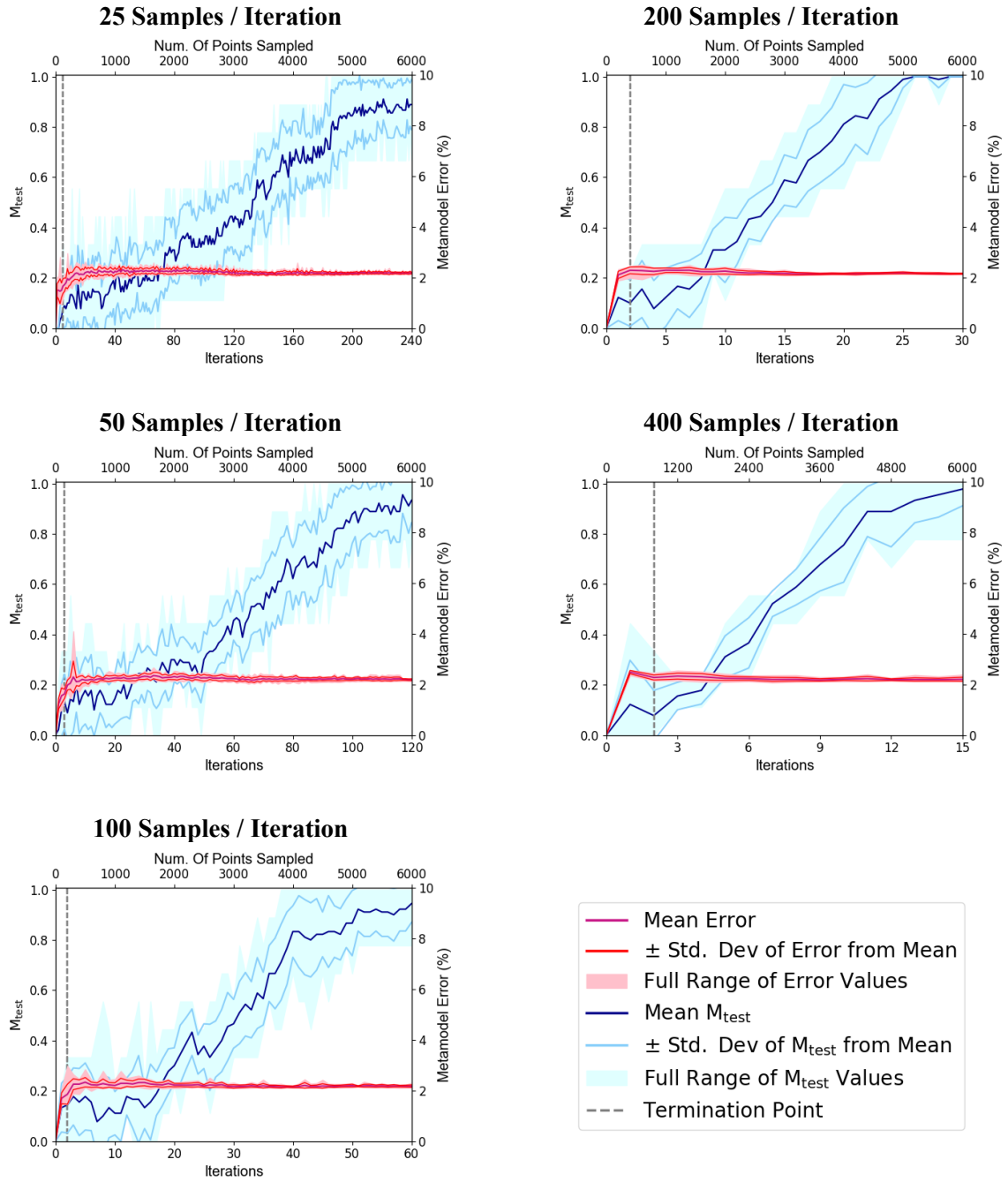
Figure 7.1: Results of the Traditional RSM Studies.

7.2 Adaptive Surrogate-Assisted Response Surface Methodology Studies

7.2.1 Setup of ASA-RSM Studies

This section outlines the various ASA-RSM studies that were conducted in this work. Similarly, the ASA-RSM presented in Section 2.4.2.1 was implemented into a custom program in Python. The FNN metamodel architecture and hyperparameters, average metamodel relative error tolerance, ϵ_{tol}^{err}, the NSGA-II optimization parameters, and performance metric definitions used with the traditional RSM used in Section 7.1 were used in this study as well, to facilitate a direct comparison between the two approaches. Similarly, the sampling rate, N, was varied according to $N = 25 \times 2^i$ with $0 \leq i \leq 4$ to explore the convergence speed and accuracy of the framework. The PDR parameters used in this study are $\eta = 0.75$, $\gamma_{pan} = 1.0$, $\gamma_{osc} = 0.85$, and $\beta = 1.0$. The additional stopping criterion used is $\epsilon_{Pareto}^{err} = 0.03$.

7.2.2 Results and Discussion of ASA-RSM Studies

Figure 7.2 and Table 7.2 presents the summary of the performance of the various studies of the ASA-RSM. The "in-the-loop" inclusion of the optimization step and the Pareto domain reduction allows the method to identify and focus on the optimal region more quickly. The ASA-RSM approach terminated on average with ~2,400 samples of the total domain, approximately 25% of the entire domain. The post-mortem analysis of the performance metric showed that the ASA-RSM approach is on average identifying 7.85 ± 1.06 out of 9 ($87.2\% \pm 11.8\%$) designs on the true Pareto front. N = 400 used an average of 3,180 samples (33%), but achieved 100% true Pareto front accuracy. In some trials, it converged with fewer samples. A higher sampling rate is more accurate because there are fewer iterations for the domain reduction scheme to concentrate on a particular region that does not contain the full Pareto front.

Conversely, some cases (N = [25,100]) required less than 2,000 samples before converging to an acceptable level of accuracy. In the particular instance of N = 100, very good accuracy is achieved after 1200 samples, and the average response continues to refine and improve until it satisfied the convergence criteria. Now, it should be noted that approximately 25% sampling of the entire domain may still be cost-prohibitive, especially in design applications with more parameters and load cases. However, using a criterion of maximum number of samples would provide some control to a designer, given that a continuous improvement would be observed. Nevertheless, the ASA-RSM shows continuous improvement with each iteration.

Table 7.2: Summary of Results for ASA-RSM Studies.

Samples / Iteration	25	50	100	200	400
Average Num. Samples	1850	2400	1900	2700	3120
Average Test Score, M_{test}	0.79	0.72	0.89	0.96	1.0
Standard Dev., M_{test}	0.18	0.16	0.15	0.10	0.0
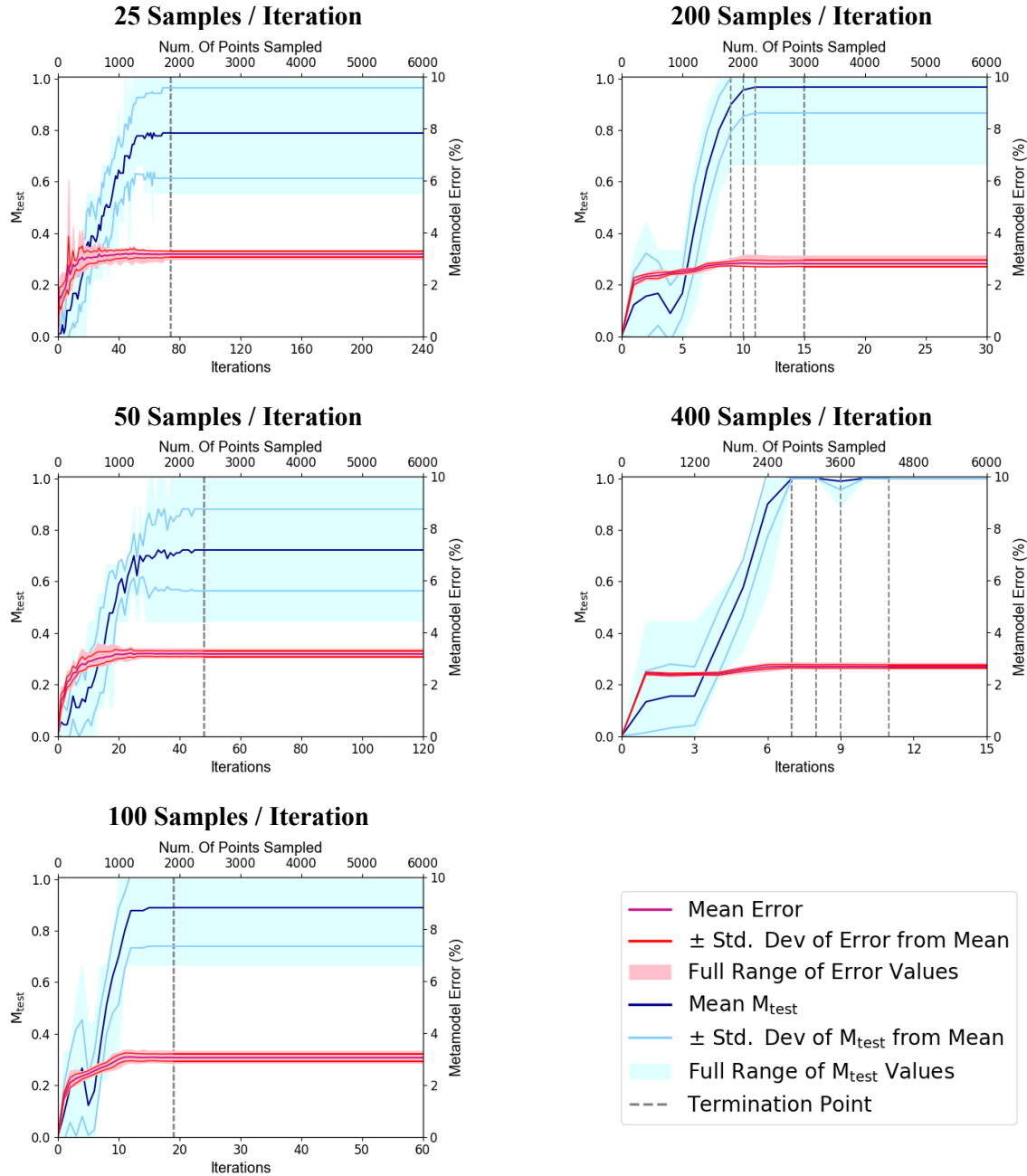
Figure 7.2: Results of the ASA-RSM Studies.

The result of the intelligent sampling method is that the full Pareto front may be efficiently found. This allows the designer to realize the real potential performance improvements that are available in the design space. Even without access to the costly brute force study, the ASA-RSM allows a designer to identify these high-performance designs efficiently. However, it should be noted that the present work is limited to three design variables and two load angles considered. Reducing the domain size in each dimension has a multiplicative effect on the reduction of the overall domain hypervolume size. It can reasonably be expected that a higher-dimension problem with more design variables and load cases would benefit even more from the domain reduction scheme. The high efficiency and high performance of the ASA-RSM open up the possibility for new and valuable studies to be feasibly performed.
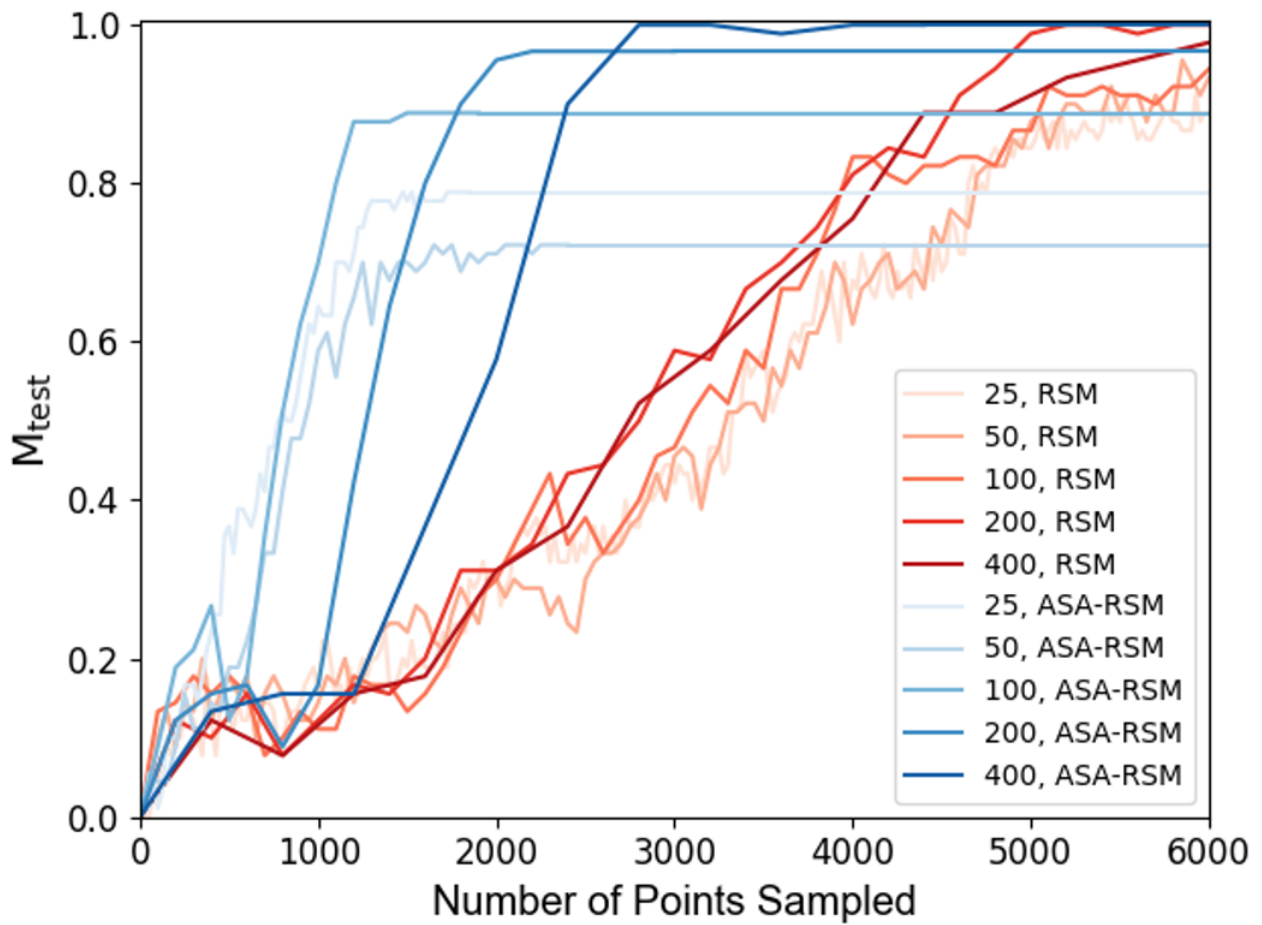
Figure 7.3: Comparison of ASA-RSM and RSM with Different Sampling Rates.

8 CONCLUSIONS

This work presented a multi-objective optimization analysis of a multi-cellular aluminum extrusion, known as the UWR4, which was subjected to axial and oblique loading conditions. The UWR4 profile was initially developed by Kohar et al. [24] and was previously studied in only axial crush applications. Although the UWR4 showed good performance in axial crush compared to a Baseline profile, the oblique impact's sensitivity had not been explored. Finite element simulations of both the Baseline and UWR4 profiles were constructed using the commercial FE software, LS-Dyna, to explore the energy absorption characteristics of the structures when subjected to oblique loading conditions. The construction of the FE models for both the baseline and UWR4 was verified using experimental sled testing experiments presented in Kohar et al. [24] and Zhumagulov [27].

The FE model of the UWR4 predicted a +37% higher mean force compared to the Baseline profile in axial crushing. When subjected to a 20º oblique impact, the FE model also predicted +31.9% higher energy absorption in the UWR4 than the Baseline profile. The UWR4 profile has higher energy absorption in oblique crush because the deformation mechanisms eventually transition to the progressive crush that arose during axial crushing. Although the Baseline profile also had lower oblique crush efficiency (0.61 vs. 0.67), the Baseline profile had a higher oblique impact coefficient for both mean (0.70) and peak (0.74) force compared to the mean (0.68) and peak (0.68) oblique impact coefficient of the UWR4 profile. The oblique impact coefficient can be interpreted as a measure of sensitivity to oblique impact loading. This means that the Baseline profile is less sensitive to oblique impact loading, while the UWR4 has higher mean axial and oblique energy absorption. These differences in these various energy absorption characteristics indicated that there is a trade-off between oblique and axial crush performance attributed to the cross-section profile.

Next, a parametric study that varied the cross-sectional geometry of the UWR4 was used to investigate the sensitivity of the energy absorption characteristics. A simplified FE model that embodied the physics and mechanisms of the detailed FE models was used to accelerate the sampling process. A full factorial design of experiments consisting of 9,568 simulations was used to exhaust the domain of interest fully and to identify true optimum solutions. The oblique mean force followed the approximate linear relationship with respect to the axial mean force established by Tran et al. [46], [49], while the axial mean force followed the approximate relationship observed in Kohar et al. [24], [25], [109]. However, the deviations towards the limit of performance represented a higher-order secondary effect of the geometry that allows for multi-objective optimization. Based on a criterion for generating solutions that dominated the UWR4, a Pareto front was constructed of only 9 out of 9,568 with at least 7.1% - 16.7% and 7.9% -

17.0% improvement in axial and oblique crush force, respectively. The variation in F_{mean}^{axial}, $F_{mean}^{oblique}$, η^{axial}, and λ_{mean} are ±4.30%, ±4.47%, ±2.41% and ±2.92%, respectively, which offers a design engineer flexibility in selecting a design.

Finally, multi-optimization schemes using the response surface methodology (RSM) were used to intelligently navigate the domain in an attempt to identify the Pareto front efficiently. Since an exhaustive search was performed in the parametric study, each RSM approach was evaluated in their ability to identify the true Pareto front. The traditional RSM and an adaptive surrogate-assisted RSM (ASA-RSM) were evaluated in this study. Feedforward neural networks and non-dominated sorting algorithms (NSGA-II), which are artificial intelligent models, were used as the metamodel and optimizer, respectively.

The traditional RSM approach showed the ability to capture 94% of the true Pareto front after sampling approximately 63% of the entire domain. Although this shows some benefit, the high amount of sampling may be prohibitive for more complex problems with higher input dimensionality. However, the traditional RSM is typically governed by a metamodel convergence criteria that terminates the scheme much earlier. As a result, the traditional RSM approach generally terminated after ~1.3-8.4% of domain sampling while only achieving an average of 0.95 out of 9 (10.5%) of the true Pareto front points. Even allowing the traditional RSM approach to use up to 1500 samples (~15% of the domain) showed similar performance of approximately 10% accuracy. The formulation showed little to no sensitivity to the sampling rate because no information about the metamodel or optimization solution was used in seeding the next generation of sampling.

By utilizing an intelligent domain sampling approach that utilizes information from each iteration to seed the next, the ASA-RSM showed a significantly improved ability to converge to the optimal solution compared to the traditional RSM approach. The ASA-RSM was able to identify 87% of the true Pareto front using 25% of the entire domain. In some instances, the ASA-RSM correctly identified the true Pareto front by using 33% of the domain. The ASA-RSM showed some sensitivity to the chosen sampling rate; a high sampling rate provided a "slow and very accurate" result, while a low sampling rate provided a "fast and moderately accurate" result. Across all sampling rates, the ASA-RSM showed significantly better performance than the traditional RSM approach. Depending on the configuration, the ASA-RSM achieved 40-80% accuracy in predicting the Pareto front compared to the 10% accuracy achieved by the traditional RSM approach when sampling up to 15% of the domain. Together, this comprehensive study provides critical insight into quantifying how much performance gain is possible through a multi-objective approach, how to perform it efficiently, and the associated cost.

9   RECOMMENDATIONS FOR FUTURE WORK

This thesis highlight the efficiency and effectiveness of advanced RSM techniques, such as the ASA-RSM approach, for multi-objective optimization of crush rails. Coupled with FE models, the ASA-RSM creates a platform for design optimization, which is relatively computationally efficient. As such, it opens the door for more complex studies to be performed, both in terms of more advanced FE models and more extensive optimization studies. The following recommendations are presented for future work.

9.1   Simulation

1. *Incorporation of a Detailed Fracture Model*: The current work assumes that no design produces a sufficiently complex deformation response locally to warrant fracture concerns. First, a simple fracture criteria that is based on effective plastic strain was used in this study. It is well known that fracture is dependent on the stress state and history. Incorporating more advanced fracture models, such the Lode-triaxiality dependent models by Bao and Wierzbicki [197], Bai and Wierzbicki [198], [199] or the generalized incremental stress state dependent damage model (GISSMO) by Neukamm et al. [200], could have a profound effect on the optimal results. Next, the simplified FE models that were used in the parametric study were conducted with 5mm x 5mm shell elements. However, the effective plastic strain criteria ($\bar{\varepsilon}^p = 1.4$) for fracture remained unchanged from the value used in the detailed FE models which utilized a mesh size of 1mm x 1mm. It is well understood that fracture models show significant mesh dependence, where larger elements require a lower effective plastic strain to failure due to an averaging effect across the element [201], [202]. This is known as mesh regularization. Therefore, a 5mm x 5mm shell element that uses the original failure criteria of the 1mm x 1mm elements will effectively be removing failure from the simulation. The simulations generated in the parametric study may violate this assumption, which could have a catastrophic implication on the overall performance of the structure. Future studies should incorporate a detailed fracture model that incorporates a mesh regularization scheme.

2. *Advanced Material Modelling:* The Yld-2004 plasticity model used in this work is a 3D model which captures anisotropy in both yield strength and Lankford coefficient. However, it is unable to account for the evolution of the material properties as the deformation occurs. The crystal-plasticity-based model recently introduced by Kohar et al. [70] can account for texture evolution and can better capture real material behaviour. The use of such a model is recommended to maximize the predictive capability of the FE model. Also, thermomechanical modeling can be incorporated to capture the physics of the problem better.

3. *Robust Design Considering Manufacturing Variation:* It was assumed that each profile design was independent of the material properties. However, the manufacturing process (i.e., extrusion) can affect the material's mechanical properties in terms of yield strength and hardening. A slight variation to the mechanical properties could have a profound effect on the stability and robustness of the optimized solution. A robustness optimization study that considers variations to the material properties can be explored.

4. *Extension to Additional Loading Conditions:* The design of automotive structures extends far beyond crush rails. Many structures are responsible for crashworthiness, such as the rocker panels and side cells. These structures experience loading conditions beyond the crushing loads examined in this work, particularly lateral bending deformation. An extension of the current work, to consider the multi-objective design optimization of these additional vehicle structures under additional loading conditions, would be of significant value to the broader study of vehicle crashworthiness.

9.2 Experimentation

1. *Optimal Designs:* Dynamic impact experiments of the optimal designs presented within this work would serve as a valuable final validation to determine their feasibility for use in a real-world application.

2. *Oblique Impact Testing:* Dynamic oblique impact experiments of extruded multi-cellular aluminum crush rails should be performed, either of the original UWR4 design or the new proposed optimal designs. Dynamic oblique impact data is rare in the literature and would be a valuable source of validation data for oblique crush FE models – both for this work and future work.

9.3 Optimization

1. *Higher-Dimension Optimization Problems:* The present work is limited to three design variables and two load angles. However, the introduction of the Pareto Domain Reduction scheme was found to be effective at reducing the expense of the framework. Reducing the domain size in each dimension has a multiplicative effect on reducing the overall domain hypervolume size. It can be reasonably expected that a higher-dimension problem with more design variables and load cases would benefit even more from the domain reduction scheme. Thus, a study is recommended to "push the limits" of the domain reduction scheme with a high-dimensionality problem by coupling shape optimization with thickness optimization and other parameters (i.e., functionally graded thickness, functionally graded material properties, etc.).

2. *Further RSM Enhancement by Advanced Sampling Methods*: In Section 2.4.2, there is a discussion of advanced RSM approaches that use information from the metamodel to intelligently sample points where the metamodel will most benefit from new information. In the present work, the approach is instead to use information about the optimal set to sample in the region around the optimal. However, these approaches are not exclusive. Once the domain has been reduced to the region around the optimal set, intelligent sampling may be performed. It is recommended to design an optimization framework that incorporates these elements and study their efficacy.

3. *Neural Network Studies*: Feedforward neural networks are powerful regression tools that can model very complex relationships. However, the number of hyperparameters is very high – particularly when selecting a network architecture. Performing a hyperparameter study on every new problem may not always be feasible. It is recommended that a wide-ranging study of various crashworthiness optimization problems be performed to investigate the best neural network architectures for these kinds of problems. Then, general recommendations on neural network architectures may be provided to the crashworthiness community, facilitating future use of FNN metamodels.

REFERENCES

[1]   G. of Canada, "Passenger Automobile and Light Truck Greenhouse Gas Emission Regulations," 2016.

[2]   Insurance Institute for Highway Safety, "Moderate Overlap Frontal Crashworthiness Evaluation Crash Test Protocol (Version XV) May 2014," no. May, 2014.

[3]   Insurance Institute for Highway Safety, "Small Overlap Frontal Crashworthiness Evaluation Crash Test Protocol (Version III)," no. May, p. 25, 2014.

[4]   NHTSA, "Overview of NHTSA Priority Plan for Vehicle Safety and Fuel Economy , 2015 to 2017," pp. 1–22, 2015.

[5]   S. Yang and C. Qi, "Multiobjective optimization for empty and foam-filled square columns under oblique impact loading," *Int. J. Impact Eng.*, vol. 54, pp. 177–191, 2013, doi: 10.1016/j.ijimpeng.2012.11.009.

[6]   L. Ying, M. Dai, S. Zhang, H. Ma, and P. Hu, "Multiobjective crashworthiness optimization of thin-walled structures with functionally graded strength under oblique impact loading," *Thin-Walled Struct.*, vol. 117, no. April, pp. 165–177, 2017, doi: 10.1016/j.tws.2017.04.007.

[7]   C. Qi, S. Yang, and F. Dong, "Crushing analysis and multiobjective crashworthiness optimization of tapered square tubes under oblique impact loading," *Thin-Walled Struct.*, vol. 59, pp. 103–119, 2012, doi: 10.1016/j.tws.2015.11.020.

[8]   K. Yamazaki and J. Han, "Maximization of the crushing energy absorption of tubes," *Struct. Optim.*, pp. 37–46, 1998, doi: 10.1007/BF01213998.

[9]   E. Acar, M. A. Guler, B. Gerçeker, M. E. Cerit, and B. Bayram, "Multi-objective crashworthiness optimization of tapered thin-walled tubes with axisymmetric indentations," *Thin-Walled Struct.*, vol. 49, no. 1, pp. 94–105, Jan. 2011, doi: 10.1016/j.tws.2010.08.010.

[10]   S. Wu, G. Zheng, G. Sun, Q. Liu, G. Li, and Q. Li, "On design of multi-cell thin-wall structures for crashworthiness," *Int. J. Impact Eng.*, vol. 88, pp. 102–117, 2016, doi: 10.1016/j.ijimpeng.2015.09.003.

[11]   H. R. Zarei and M. Kröger, "Crashworthiness optimization of empty and filled aluminum crash boxes," *Int. J. Crashworthiness*, vol. 12, no. 3, pp. 255–264, 2007, doi:

10.1080/13588260701441159.

[12]   T. Jansson, L. Nilsson, and M. Redhe, "Using surrogate models and response surfaces in structural optimization - With application to crashworthiness design and sheet metal forming," *Struct. Multidiscip. Optim.*, vol. 25, no. 2, pp. 129–140, 2003, doi: 10.1007/s00158-002-0279-y.

[13]   Y. Liu, "Crashworthiness design of multi-corner thin-walled columns," *Thin-Walled Struct.*, vol. 46, no. 12, pp. 1329–1337, 2008, doi: 10.1016/j.tws.2008.04.003.

[14]   X. Song, G. Sun, G. Li, W. Gao, and Q. Li, "Crashworthiness optimization of foam-filled tapered thin-walled structure using multiple surrogate models," *Struct. Multidiscip. Optim.*, vol. 47, no. 2, pp. 221–231, 2013, doi: 10.1007/s00158-012-0820-6.

[15]   W. J. Roux, N. Stander, and R. T. Haftka, "Response Surface Approximations for Structural Optimization," *Int. J. Numer. Methods Eng.*, vol. 42, no. December 1996, pp. 517–534, 1998, doi: 10.1002/(SICI)1097-0207(19980615)42:3<517::AID-NME370>3.0.CO;2-L.

[16]   Y. Liu, "Optimum design of straight thin-walled box section beams for crashworthiness analysis," *Finite Elem. Anal. Des.*, vol. 44, no. 3, pp. 139–147, 2008, doi: 10.1016/j.finel.2007.11.003.

[17]   A. Asanjarani, S. H. Dibajian, and A. Mahdian, "Multi-objective crashworthiness optimization of tapered thin-walled square tubes with indentations," *Thin-Walled Struct.*, vol. 116, no. March, pp. 26–36, 2017, doi: 10.1016/j.tws.2017.03.015.

[18]   X. Zhang, Z. Wen, and H. Zhang, "Axial crushing and optimal design of square tubes with graded thickness," *Thin-Walled Struct.*, vol. 84, pp. 263–274, 2014, doi: 10.1016/j.tws.2014.07.004.

[19]   Z. Zhang, W. Sun, Y. Zhao, and S. Hou, "Crashworthiness of different composite tubes by experiments and simulations," *Compos. Part B Eng.*, vol. 143, pp. 86–95, 2018, doi: 10.1016/j.compositesb.2018.01.021.

[20]   N. Tanlak, "Cross-sectional shape optimization of thin-walled columns enduring oblique impact loads," *Thin-Walled Struct.*, vol. 109, pp. 65–72, 2016, doi: 10.1016/j.tws.2016.09.009.

[21]   T. N. Tran and A. Baroutaji, "Crashworthiness optimal design of multi-cell triangular tubes under axial and oblique impact loading," *Eng. Fail. Anal.*, vol. 93, no. May, pp. 241–256, 2018, doi: 10.1016/j.engfailanal.2018.07.003.

[22]   Z. Li, W. Ma, P. Xu, and S. Yao, "Crashworthiness of multi-cell circumferentially corrugated square

tubes with cosine and triangular configurations," *Int. J. Mech. Sci.*, vol. 165, no. September 2019, p. 105205, Jan. 2020, doi: 10.1016/j.ijmecsci.2019.105205.

[23]   N. Stander, "An Adaptive Surrogate-Assisted Strategy for Multi-Objective Optimization," *10th World Congr. Struct. Multidiscip. Optim.*, pp. 1–11, 2013, doi: 10.1155/2016/9420460.

[24]   C. P. Kohar, A. Zhumagulov, A. Brahme, M. J. Worswick, R. K. Mishra, and K. Inal, "Development of high crush efficient, extrudable aluminium front rails for vehicle lightweighting," *Int. J. Impact Eng.*, vol. 95, 2016, doi: 10.1016/j.ijimpeng.2016.04.004.

[25]   C. P. Kohar, A. Brahme, J. Imbert, R. K. Mishra, and K. Inal, "Effects of coupling anisotropic yield functions with the optimization process of extruded aluminum front rail geometries in crashworthiness," *Int. J. Solids Struct.*, vol. 128, pp. 174–198, 2017, doi: 10.1016/j.ijsolstr.2017.08.026.

[26]   C. P. Kohar, "Multi-scale Modeling and Optimization of Energy Absorption and Anisotropy in Aluminum Alloys by," *Thesis Univ. Waterloo*, 2017.

[27]   A. Zhumagulov, "Crashworthiness and Material Characterization of Multi-Cellular AA6063 Extrusions," 2017.

[28]   NHTSA, "Purchasing With Safety in Mind," 2016.

[29]   Euro-NCAP, "European New Car Assessment Programme (Euro NCAP) Offset Deformable Barrier Frontal Impact," no. April, 2015.

[30]   E. G. Takhounts, M. J. Craig, K. Moorhouse, J. McFadden, and V. Hasija, "Development of Brain Injury Criteria (BrIC)," *SAE Tech. Pap.*, vol. 2013-Novem, no. November, pp. 243–266, 2013, doi: 10.4271/2013-22-0010.

[31]   A. Pugsley and M. Macaulay, "The Large Scale Crumpling of Thin Cylindrical Columns," no. December 1958, pp. 1–9, 1958, doi: 10.1093/qjmam/13.1.1.

[32]   J. M. Alexander, "An approximate analysis of the collapse of thin-walled cylindrical shells under axial loading," vol. XIII, 1959, doi: 10.1093/qjmam/13.1.10.

[33]   W. Johnson, P. D. Soden, and S. T. S. Al-Hassani, "Inextensional Collapse of Thin-Walled Tubes Under Axial Compression," *J. Strain Anal.*, vol. 12, no. 4, pp. 317–330, 1977, doi: 10.1243/03093247V124317.

[34] A. Reyes, M. Langseth, and O. S. Hopperstad, "Crashworthiness of aluminum extrusions subjected to oblique loading: Experiments and numerical analyses," *Int. J. Mech. Sci.*, vol. 44, no. 9, pp. 1965–1984, 2002, doi: 10.1016/S0020-7403(02)00050-4.

[35] S. R. Reid and T. Y. Reddy, "Static and dynamic crushing of tapered sheet metal tubes of rectangular cross-section," *Int. J. Mech. Sci.*, vol. 28, no. 9, pp. 623–637, 1986, doi: 10.1016/0020-7403(86)90077-9.

[36] "Crash Testing and Modelling of Structural Components." https://uwaterloo.ca/waterloo-forming-crash-lab/research-areas/crash-testing-and-modelling-structural-components (accessed Aug. 23, 2018).

[37] A. Reyes, M. Langseth, and O. S. Hopperstad, "Square aluminum tubes subjected to oblique loading," *Int. J. Impact Eng.*, vol. 28, no. 10, pp. 1077–1106, 2003, doi: 10.1016/S0734-743X(03)00045-9.

[38] A. Reyes, O. S. Hopperstad, and M. Langseth, "Aluminum foam-filled extrusions Subjected to oblique loading: experimental and numerical study," *Int. J. Solids Struct.*, vol. 41, no. 5–6, pp. 1645–1675, 2004, doi: 10.1016/j.ijsolstr.2003.09.053.

[39] Z. Ahmad, D. P. Thambiratnam, and A. C. C. Tan, "Dynamic energy absorption characteristics of foam-filled conical tubes under oblique impact loading," *Int. J. Impact Eng.*, vol. 37, no. 5, pp. 475–488, 2010, doi: 10.1016/j.ijimpeng.2009.11.010.

[40] A. L. Browne and N. L. Johnson, "Dynamic Crush Tests Using A 'Free-Flight' Drop Tower: Theory," *Exp. Tech.*, vol. 26, no. 5, pp. 43–46, Sep. 2002, doi: 10.1111/j.1747-1567.2002.tb00084.x.

[41] C. Peister, "Axial Crush Performance of Hot Stamped Tailor Welded Blanks - Experiments and Numerical Simulations," University of Waterloo, 2019.

[42] W. Abramowicz and N. Jones, "Dynamic Axial Crushing of Square Tubes," *Int. J. Impact Eng.*, vol. 2, no. 3, pp. 263–281, 1984, doi: 10.1016/0734-743X(84)90010-1.

[43] W. Abramowicz and N. Jones, "Dynamic progressive buckling of circular and square tubes," *Int. J. Impact Eng.*, vol. 4, no. 4, pp. 243–270, 1986, doi: 10.1016/0734-743X(86)90017-5.

[44] O. Jensen, M. Langseth, and O. S. Hopperstad, "Experimental investigations on the behaviour of short to long square aluminium tubes subjected to axial loading," *Int. J. Impact Eng.*, vol. 30, no. 8–9, pp. 973–1003, 2004, doi: 10.1016/j.ijimpeng.2004.05.002.

[45]   Y. Zhang, S. Wu, Y. Shi, J. Tu, and J. Hu, "Inclined Impact Test and Computer Simulation of Front Rail," Apr. 2014, doi: 10.4271/2014-01-0794.

[46]   T. N. Tran, "Crushing analysis under multiple impact loading cases for multi-cell triangular tubes," *Thin-Walled Struct.*, vol. 113, no. February 2016, pp. 262–272, 2017, doi: 10.1016/j.tws.2017.01.013.

[47]   A. G. Hanssen, M. Langseth, and O. S. Hopperstad, "Static and dynamic crushing of square aluminium extrusions with aluminium foam filler," *Int. J. Impact Eng.*, vol. 24, no. 5, pp. 475–507, 1999, doi: 10.1016/S0734-743X(99)00170-0.

[48]   K. R. F. Andrews, G. L. England, and E. Ghani, "Classification of the axial collapse of cylindrical tubes under quasi-static loading," *Int. J. Mech. Sci.*, vol. 25, no. 9–10, pp. 687–696, 1983, doi: 10.1016/0020-7403(83)90076-0.

[49]   T. N. Tran, S. Hou, X. Han, N. Nguyen, and M. Chau, "Theoretical prediction and crashworthiness optimization of multi-cell square tubes under oblique impact loading," *Int. J. Mech. Sci.*, vol. 89, pp. 177–193, 2014, doi: 10.1016/j.ijmecsci.2014.08.027.

[50]   T. Wierzbicki and W. Abramowicz, "On the Crushing Mechanics of Thin-Walled Structures," *J. Appl. Mech.*, vol. 50, no. 4a, pp. 727–734, Dec. 1983, doi: 10.1115/1.3167137.

[51]   T. Wierzbicki, L. Recke, W. Abramowicz, T. Gholami, and J. Huang, "Stress profiles in thin-walled prismatic columns subjected to crush loading-II. Bending," *Comput. Struct.*, vol. 51, no. 94, pp. 625–641, 1994, doi: http://dx.doi.org/10.1016/S0045-7949(05)80002-1.

[52]   W. Chen and T. Wierzbicki, "Relative merits of single-cell, multi-cell and foam-filled thin-walled structures in energy absorption," *Thin-Walled Struct.*, vol. 39, no. 4, pp. 287–306, 2001, doi: 10.1016/S0263-8231(01)00006-4.

[53]   G. R. Cowper and P. S. Symonds, "Strain hardening and strain-rate effects in the impact loading of cantilever beams," *Brown Univ. Tech. Rep.*, 1957.

[54]   X. Zhang, G. Cheng, and H. Zhang, "Theoretical prediction and numerical simulation of multi-cell square thin-walled structures," *Thin-Walled Struct.*, vol. 44, no. 11, pp. 1185–1191, 2006, doi: 10.1016/j.tws.2006.09.002.

[55]   X. Zhang and H. Huh, "Crushing analysis of polygonal columns and angle elements," *Int. J. Impact Eng.*, vol. 37, no. 4, pp. 441–451, 2010, doi: 10.1016/j.ijimpeng.2009.06.009.

[56]   X. Zhang and H. Zhang, "Numerical and theoretical studies on energy absorption of three-panel angle elements," *Int. J. Impact Eng.*, vol. 46, pp. 23–40, 2012, doi: 10.1016/j.ijimpeng.2012.02.002.

[57]   X. Zhang and H. Zhang, "Experimental and numerical investigation on crush resistance of polygonal columns and angle elements," *Thin-Walled Struct.*, vol. 57, pp. 25–36, 2012, doi: 10.1016/j.tws.2012.04.006.

[58]   X. Zhang and H. Zhang, "Theoretical and numerical investigation on the crush resistance of rhombic and kagome honeycombs," *Compos. Struct.*, vol. 96, pp. 143–152, 2013, doi: 10.1016/j.compstruct.2012.09.028.

[59]   X. Zhang and H. Zhang, "The crush resistance of four-panel angle elements," *Int. J. Impact Eng.*, vol. 78, pp. 81–97, 2015, doi: 10.1016/j.ijimpeng.2014.12.004.

[60]   W. Abramowicz, "The effective crushing distance in axially compressed thin-walled metal columns," *Int. J. Impact Eng.*, vol. 1, no. 3, pp. 309–317, 1983, doi: 10.1016/0734-743X(83)90025-8.

[61]   A. P. Meran, "Solidity effect on crashworthiness characteristics of thin-walled tubes having various cross-sectional shapes," *Int. J. Crashworthiness*, vol. 21, no. 2, pp. 135–147, 2016, doi: 10.1080/13588265.2015.1127584.

[62]   L. S. T. Corporation, *LS-DYNA Theory Manual*. Livermore, California: Livermore Software Technology Corporation, 2017.

[63]   T. Belytschko and J. Fish, *A First Course in Finite Elements*. Wiley & Sons, 2007.

[64]   T. J. R. Hughes, *The Finite Element Method: Linear Static and Dynamic Finite Element Analysis*. Englewood Cliffs, New Jersey: Prentice-Hall Inc., 1987.

[65]   T. Belytschko, W. K. Liu, and B. Moran, "Nonlinear Finite Elements for Continua and Structures," in *Nonlinear Finite Elements for Continua and Structures*, 2014.

[66]   L. S. T. Corporation, *LS-DYNA Keyword User's Manual Volume II Material Models LS-DYNA R9.0*. Livermore, California: Livermore Software Technology Corporation.

[67]   D. S. Connolly, C. P. Kohar, W. Muhammad, L. G. Hector, R. K. Mishra, and K. Inal, "A coupled thermomechanical crystal plasticity model applied to Quenched and Partitioned steel," *Int. J. Plast.*, vol. 133, p. 102757, Oct. 2020, doi: 10.1016/j.ijplas.2020.102757.

[68]	Y. L. Li, C. P. Kohar, R. K. Mishra, and K. Inal, "A new crystal plasticity constitutive model for simulating precipitation-hardenable aluminum alloys," *Int. J. Plast.*, vol. 132, p. 102759, Sep. 2020, doi: 10.1016/j.ijplas.2020.102759.

[69]	A. Iftikhar, Y. L. Li, C. P. Kohar, K. Inal, and A. S. Khan, "Evolution of subsequent yield surfaces with plastic deformation along proportional and non-proportional loading paths on annealed AA6061 alloy: Experiments and crystal plasticity finite element modeling," *Int. J. Plast.*, p. 102956, Mar. 2021, doi: 10.1016/j.ijplas.2021.102956.

[70]	C. P. Kohar, J. L. Bassani, A. Brahme, W. Muhammad, R. K. Mishra, and K. Inal, "A new multi-scale framework to incorporate microstructure evolution in phenomenological plasticity: Theory, explicit finite element formulation, implementation and validation," *Int. J. Plast.*, vol. 117, pp. 122–156, Jun. 2019, doi: 10.1016/j.ijplas.2017.08.006.

[71]	A. Abedini, J. Noder, C. P. Kohar, and C. Butcher, "Accounting for Shear Anisotropy and Material Frame Rotation on the Constitutive Characterization of Automotive Alloys using Simple Shear Tests," *Mech. Mater.*, vol. 148, p. 103419, Sep. 2020, doi: 10.1016/j.mechmat.2020.103419.

[72]	J. Tham, T. Sabiston, A. Trauth, J. Lévesque, K. A. Weidenmann, and K. Inal, "The effect of tension compression asymmetry on modelling the bending response of sheet moulding compound composites," *Compos. Part B Eng.*, vol. 154, pp. 157–165, Dec. 2018, doi: 10.1016/j.compositesb.2018.07.058.

[73]	A. Abedini, C. Butcher, and M. Worswick, "Application of an Evolving Non-Associative Anisotropic-Asymmetric Plasticity Model for a Rare-Earth Magnesium Alloy," *Metals (Basel).*, vol. 8, no. 12, p. 1013, Dec. 2018, doi: 10.3390/met8121013.

[74]	W. Muhammad, A. P. Brahme, R. K. Sabat, R. K. Mishra, and K. Inal, "A criterion for ductile failure in age-hardenable aluminum alloys," *Mater. Sci. Eng. A*, vol. 759, pp. 613–623, Jun. 2019, doi: 10.1016/j.msea.2019.05.055.

[75]	K. Chung and O. Richmond, "A deformation theory of plasticity based on minimum work paths," vol. 9, pp. 907–920, 1993.

[76]	J. W. Yoon, F. Barlat, R. E. Dick, K. Chung, and T. J. Kang, "Plane stress yield function for aluminum alloy sheets - Part II: FE formulation and its implementation," *Int. J. Plast.*, vol. 20, no. 3, pp. 495–522, 2004, doi: 10.1016/S0749-6419(03)00099-8.

[77] N. Abedrabbo, F. Pourboghrat, and J. Carsley, "Forming of aluminum alloys at elevated temperatures – Part 2 : Numerical modeling and experimental verification," vol. 22, pp. 342–373, 2006, doi: 10.1016/j.ijplas.2005.03.006.

[78] C. P. Kohar, M. Mohammadi, R. K. Mishra, and K. Inal, "The effects of the yield surface curvature and anisotropy constants on the axial crush response of circular crush tubes," *Thin Walled Struct.*, vol. 106, pp. 28–50, 2016, doi: 10.1016/j.tws.2016.04.021.

[79] R. Hill, "A general theory of uniqueness and stability in elastic-plastic solids," *J. Mech. Phys. Solids*, vol. 6, no. 3, pp. 236–249, May 1958, doi: 10.1016/0022-5096(58)90029-2.

[80] R. Hill, "Some basic principles in the mechanics of solids without a natural time," *J. Mech. Phys. Solids*, vol. 7, no. 3, pp. 209–225, Jun. 1959, doi: 10.1016/0022-5096(59)90007-9.

[81] R. Hill, *Aspects of Invariance in Solid Mechanics*, vol. 18. 1978.

[82] R. Von-Mises, "Mechanics of solid bodies in the plastically-deformable state," vol. 4, pp. 582–592, 1913.

[83] W. T. Lankford, S. C. Snyder, and J. A. Bausher, "New criteria for predicting the press performance of deep drawing sheets," *Trans. ASM*, no. 42, pp. 1197–1205, 1950.

[84] O. Mohr, "Welche Umstande bedingen die Elastizitatsgrenze und den Bruch eines Materials?," *Zeitschrift des Vereins Dtsch. Ingenieure*, vol. 44, pp. 1524–1530, 1900.

[85] D. C. Drucker and W. Prager, "Soil Mechanics and Plastic Analysis or Limit Design," *Q. Appl. Math.*, vol. 10, no. 2, pp. 157–165, 1952, doi: 10.1090/qam/48291.

[86] R. Hill, "A Theory of the Yielding and Plastic Flow of Anisotropic Metals," *Proceeding R. Soc. London*, vol. 193, no. 1033, pp. 281–297, 1948.

[87] F. Barlat and K. Lian, "Plastic behavior and stretchability of sheet metals. Part I: A yield function for orthotropic sheets under plane stress conditions," *Int. J. Plast.*, vol. 5, no. 1, pp. 51–66, 1989, doi: 10.1016/0749-6419(89)90019-3.

[88] F. Barlat *et al.*, "Plane stress yield function for aluminum alloy sheets—part 1: theory," *Int. J. Plast.*, vol. 19, no. 9, pp. 1297–1319, 2003, doi: http://dx.doi.org/10.1016/S0749-6419(02)00019-0.

[89] Y. Lou and J. W. Yoon, "Anisotropic yield function based on stress invariants for BCC and FCC metals and its extension to ductile fracture criterion," *Int. J. Plast.*, vol. 101, no. June 2017, pp. 125–

155, 2018, doi: 10.1016/j.ijplas.2017.10.012.

[90] F. Barlat, H. Aretz, J. W. Yoon, M. E. Karabin, J. C. Brem, and R. E. Dick, "Linear transfomation-based anisotropic yield functions," *Int. J. Plast.*, vol. 21, no. 5, pp. 1009–1039, 2005, doi: 10.1016/j.ijplas.2004.06.004.

[91] R. W. Logan and W. F. Hosford, "Upper-bound anisotropic yield locus calculations assuming 〈111〉-pencil glide," *Int. J. Mech. Sci.*, vol. 22, no. 7, pp. 419–430, 1980, doi: 10.1016/0020-7403(80)90011-9.

[92] W. F. Hosford, "On Yield Loci of Anisotropic Cubic Metals," in *7th North American Metalworking Conference*, 1979, pp. 191–197.

[93] D. C. Drucker, "A More Fundamental Approach to Plastic Stress-Strain Relations," *Proc. 1st U.s. Mat. Congr. Appl. Mech.*, pp. 487–491, 1952.

[94] E. Voce, "A Practical Strain-Hardening Function," *Metallurgia*, vol. 51, no. 307, pp. 219–226, 1955.

[95] B. W. Williams, C. H. M. Simha, N. Abedrabbo, R. Mayer, and M. J. Worswick, "Effect of anisotropy, kinematic hardening, and strain-rate sensitivity on the predicted axial crush response of hydroformed aluminium alloy tubes," *Int. J. Impact Eng.*, vol. 37, no. 6, pp. 652–661, 2010, doi: 10.1016/j.ijimpeng.2009.10.010.

[96] A. Zhumagulov, J. Imbert, C. P. Kohar, K. Inal, M. J. Worswick, and R. K. Mishra, "Energy absorption characterization of multicellular AA6063-T6 extrusions," *ICILSM*, 2016.

[97] P. Larour, "Strain rate sensitivity of automotive sheet steels: influence of plastic strain, strain rate, temperature, microstructure, bake hardening and pre-strain," Berichte aus dem Institut für Eisenhüttenkunde, 2010.

[98] M. F. Shi and D. J. Meuleman, "Strain Rate Sensitivity of Automotive Steels," in *SAE Technical Paper*, 1992, doi: 10.4271/920245.

[99] A. Uenishi, H. Yashida, M. Takahashi, and K. Yukihisa, "Material Characterization at High Strain Rates for Optimizing Car Body Structures for Crash Events," *Nippon Steel Tech. Rep.*, no. 88, pp. 22–26, 2003.

[100] G. R. Johnson and W. H. Cook, "A constitutive model and data for metals subjected to large strains, high strain rates and high temperatures," *7th International Symposium on Ballistics*. pp. 541–547,

1983, doi: 10.1038/nrm3209.

[101] F. J. Zerilli and R. W. Armstrong, "Dislocation-mechanics-based constitutive relations for material dynamics calculations," *J. Appl. Phys.*, vol. 61, no. 5, pp. 1816–1825, 1987, doi: 10.1063/1.338024.

[102] J. Heinrich and D. Pepper, "1.2 Short History of the Finite Element Method," in *The Intermediate Finite Element Method: Fluid Flow And Heat Transfer Applications*, 1999.

[103] A. Otubushin, "Detailed validation of a non-linear finite element code using dynamic axial crushing of a square tube," *Int. J. Impact Eng.*, vol. 21, no. 5, pp. 349–368, 1998, doi: 10.1016/S0734-743X(97)00041-9.

[104] M. Langseth, O. S. Hopperstad, and T. Berstad, "Crashworthiness of aluminium extrusions: validation of numerical simulation, effect of mass ratio and impact velocity," *Int. J. Impact Eng.*, vol. 22, no. 9–10, pp. 829–854, 1999, doi: 10.1016/S0734-743X(98)00070-0.

[105] D. C. Han and S. H. Park, "Collapse behavior of square thin-walled columns subjected to oblique loads," *Thin-Walled Struct.*, vol. 35, no. 3, pp. 167–184, 1999, doi: 10.1016/S0263-8231(99)00022-1.

[106] D. Karagiozova and N. Jones, "Dynamic buckling of elastic–plastic square tubes under axial impact—II: structural response," *Int. J. Impact Eng.*, vol. 30, no. 2, pp. 167–192, 2004, doi: 10.1016/S0734-743X(03)00062-9.

[107] G. Li, Z. Zhang, G. Sun, F. Xu, and X. Huang, "Crushing analysis and multiobjective optimization for functionally graded foam-filled tubes under multiple load cases," *Int. J. Mech. Sci.*, vol. 89, pp. 439–452, 2014, doi: 10.1016/j.ijmecsci.2014.10.001.

[108] O. Fyllingen, O. S. Hopperstad, A. G. Hanssen, and M. Langseth, "Brick versus shell elements in simulations of aluminium extrusions subjected to axial crushing," *7th Eur. LS-DYNA Conf.*, 2009.

[109] C. P. Kohar, M. Mohammadi, R. K. Mishra, and K. Inal, "Effects of elastic-plastic behaviour on the axial crush response of square tubes," *Thin-Walled Struct.*, vol. 93, pp. 64–87, 2015, doi: 10.1016/j.tws.2015.02.023.

[110] T. Giagmouris, S. Kyriakides, Y. P. Korkolis, and L. H. Lee, "On the localization and failure in aluminum shells due to crushing induced bending and tension," *Int. J. Solids Struct.*, vol. 47, no. 20, pp. 2680–2692, 2010, doi: 10.1016/j.ijsolstr.2010.05.023.

[111] B. Plunkett, O. Cazacu, and F. Barlat, "Orthotropic yield criteria for description of the anisotropy in tension and compression of sheet metals," *Int. J. Plast.*, vol. 24, pp. 847–866, 2008, doi: 10.1016/j.ijplas.2007.07.013.

[112] W. F. Hosford, "A Generalized Isotropic Yield Criterion," *J. Appl. Mech.*, vol. 39, no. 2, pp. 607–609, Jun. 1972, doi: 10.1115/1.3422732.

[113] J. Arora, "Multi-Objective Optimum Design Concepts and Methods," in *Introduction to Optimum Design*, Edition 3., New York: McGraw-Hill, 2012, pp. 663–664.

[114] G. Zheng and J. Huang, *Multiple Attribute Decision Making: Methods and Applications*. Boca Raton, FL: Taylor & Francis, 2011.

[115] T. Gal, "Multiple objective decision making - methods and applications: A state-of-the art survey," *Eur. J. Oper. Res.*, vol. 4, no. 4, Apr. 1980, doi: 10.1016/0377-2217(80)90117-4.

[116] S. Hou, Q. Li, S. Long, X. Yang, and W. Li, "Multiobjective optimization of multi-cell sections for the crashworthiness design," *Int. J. Impact Eng.*, vol. 35, no. 11, pp. 1355–1367, 2008, doi: 10.1016/j.ijimpeng.2007.09.003.

[117] L. Ying, X. Zhao, M. Dai, S. Zhang, and P. Hu, "Crashworthiness design of quenched boron steel thin-walled structures with functionally graded strength," *Int. J. Impact Eng.*, vol. 95, pp. 72–88, 2016, doi: 10.1016/j.ijimpeng.2016.05.001.

[118] N. Stander *et al.*, "LS-OPT Users Manual," no. 6.0. Livermore Software Technology Corporation, Livermore, California, 2019.

[119] M. D. McKay, R. J. Beckman, and W. J. Conover, "A Comparison of Three Methods for Selecting Values of Input Variables in the Analysis of Output from a Computer Code," *Technometrics*, vol. 42, no. 1, pp. 55–61, 2000, doi: 10.1080/00401706.2000.10485979.

[120] G. Taguchi, Y. Yokoyama, and Y. Wu, *Taguchi methods: design of experiments*. Allen Park, MI: American Supplier Institute, 1993.

[121] L. Pronzato, "Minimax and maximin space-filling designs : some properties and methods for construction," *J. la Soc. Française Stat.*, vol. 158, pp. 7–36, 2017.

[122] S. M. Stigler, *The History of Statistics: The Measurement of Uncertainty before 1900*. Cambridge: Harvard, 1986.

[123] F. Hayashi, "Econometrics." Princeton University Press, 2000.

[124] A. E. Hoerl and R. W. Kennard, "Ridge Regression: Biased Estimation for Nonorthogonal Problems," *Technometrics*, vol. 12, no. 1, pp. 55–67, Feb. 1970, doi: 10.1080/00401706.1970.10488634.

[125] S. S. (viaf)32080613 Rao, *Applied numerical methods for engineers and scientists*. Upper Saddle River, N.J.: Prentice-Hall, 2002.

[126] S. Haykin, *Neural networks: a comprehensive foundation*. 1994.

[127] A. Shirzad, M. Tabesh, and R. Farmani, "A comparison between performance of support vector regression and artificial neural network in prediction of pipe burst rate in water distribution networks," *KSCE J. Civ. Eng.*, vol. 18, no. 4, pp. 941–948, May 2014, doi: 10.1007/s12205-014-0537-8.

[128] M. Hemmat Esfe, M. Afrand, W.-M. Yan, and M. Akbari, "Applicability of artificial neural network and nonlinear regression to predict thermal conductivity modeling of Al2O3–water nanofluids using experimental data," *Int. Commun. Heat Mass Transf.*, vol. 66, pp. 246–249, Aug. 2015, doi: 10.1016/j.icheatmasstransfer.2015.06.002.

[129] H. Li, S. Guo, C. Li, and J. Sun, "A hybrid annual power load forecasting model based on generalized regression neural network with fruit fly optimization algorithm," *Knowledge-Based Syst.*, vol. 37, pp. 378–387, Jan. 2013, doi: 10.1016/j.knosys.2012.08.015.

[130] A. L. Maas, A. Y. Hannun, and A. Y. Ng, "Rectifier Nonlinearities Improve Neural Network Acoustic Models," *Proc. 30 th Int. Conf. Mach. Learn.*, vol. 28, p. 6, 2013, [Online]. Available: https://web.stanford.edu/~awni/papers/relu_hybrid_icml2013_final.pdf.

[131] D. E. Rumelhart, G. E. Hinton, and R. J. Williams, "Learning representations by back-propagating errors," *Nature*, vol. 323, no. 6088, pp. 533–536, 1986, doi: 10.1038/323533a0.

[132] T. Tieleman and G. E. Hinton, "Lecture 6.5 - RMSProp, COURSERA: Neural Networks for Machine Learning," 2012.

[133] D. P. Kingma and J. Ba, "Adam: A Method for Stochastic Optimization," pp. 1–15, 2014, doi: http://doi.acm.org.ezproxy.lib.ucf.edu/10.1145/1830483.1830503.

[134] S. Hochreiter, "Untersuchungen zu dynamischen neuronalen Netzen," Technische Univ. Munich,

1991.

[135] G. E. Hinton, N. Srivastava, A. Krizhevsky, I. Sutskever, and R. R. Salakhutdinov, "Improving neural networks by preventing co-adaptation of feature detectors," pp. 1–18, 2012, doi: arXiv:1207.0580.

[136] R. Kohavi, "A study of cross-validation and bootstrap for accuracy estimation and model selection," *Int. Jt. Conf. Artif. Intell.*, vol. 2, pp. 1137–1143, 1995, doi: 10.5555/1643031.1643047.

[137] C. E. Rasmussen and C. K. I. Williams, *Gaussian processes for machine learning.*, vol. 14, no. 2. MIT Press, 2004.

[138] S. S. Esfahlani, H. Shirvani, A. Shirvani, S. Nwaubani, H. Mebrahtu, and C. Chirwa, "Hexagonal honeycomb cell optimisation by way of meta-model techniques," *Int. J. Crashworthiness*, vol. 18, no. 3, pp. 264–275, 2013, doi: 10.1080/13588265.2013.776337.

[139] N. Qian, "On the momentum term in gradient descent learning algorithms," *Neural Networks*, vol. 12, no. 1, pp. 145–151, Jan. 1999, doi: 10.1016/S0893-6080(98)00116-6.

[140] P. E. Gill, W. Murray, and M. H. Wright, *Practical Optimization*. New York: Academic Press, 1981.

[141] V. Černý, "Thermodynamical approach to the traveling salesman problem: An efficient simulation algorithm," *J. Optim. Theory Appl.*, vol. 45, no. 1, pp. 41–51, 1985, doi: 10.1007/BF00940812.

[142] R. Storn and K. Price, "Differential Evolution - A Simple and Efficient Heuristic for Global Optimization over Continuous Spaces," *J. Glob. Optim.*, vol. 11, pp. 341–359, 1997, doi: 10.1023/A:1008202821328.

[143] R. Eberhart and J. Kennedy, "New optimizer using particle swarm theory," *Proc. Int. Symp. Micro Mach. Hum. Sci.*, pp. 39–43, 1995, doi: 10.1109/mhs.1995.494215.

[144] M. Mitchell, *An Introduction to Genetic Algorithms*. Cambridge, MA: MIT Press, 1996.

[145] D. E. Rumelhart, G. E. Hinton, and R. J. Williams, "Learning Internal Representations by Error Propagation Volume I: Foundations," in *Parallel Distributed Processing: Explorations in the Microstructure of Cognition*, D. E. Rumelhart and J. L. Mcclelland, Eds. Cambridge, MA: MIT Press, 1986, pp. 318–362.

[146] E. Süli and D. Meyers, *An Introduction to Numerical Analysis*. Cambridge, UK: Cambridge University Press, 2003.

[147] P. Wolfe, "Convergence Conditions for Ascent Methods," *SIAM Rev.*, vol. 11, no. 2, pp. 226–235, Apr. 1969, doi: 10.1137/1011036.

[148] D. C. Liu and J. Nocedal, "On the limited memory BFGS method for large scale optimization," *Math. Program.*, vol. 45, no. 1–3, pp. 503–528, Aug. 1989, doi: 10.1007/BF01589116.

[149] J. Holland, *Adaptation in natural and artificial systems: an introductory analysis with applications to biology, control, and artificial intelligence*, 2nd ed. Ann Arbor, Michigan: University of Michigan Press, 1992.

[150] J. Arora, "GA Crossover," in *Introduction to Optimum Design*, Edition 3., Elsevier, 2011, p. 648.

[151] J. Arora, "GA Steps," in *Introduction to Optimum Design*, Edition 3., Elsevier, 2011, p. 650.

[152] J. Arora, "Roulette Selection," in *Introduction to Optimum Design*, Edition 3., Elsevier, 2011, p. 647.

[153] J. Arora, "Tournament Selection," in *Introduction to Optimum Design*, Edition 3., Elsevier, 2011, p. 670.

[154] K. Deb and R. B. Agrawal, "Simulated Binary Crossover for Continuous Search Space," *Complex Syst.*, vol. 9, pp. 1–34, 1994.

[155] J. D. Knowles and D. W. Corne, "Approximating the Nondominated Front Using the Pareto Archived Evolution Strategy," *Evol. Comput.*, vol. 8, no. 2, pp. 149–172, 2000, doi: 10.1162/106365600568167.

[156] E. Zitzler, "Evolutionary Algorithms for Multiobjective Optimization: Methods and Applications." Zurich, Switzerland, 1999.

[157] K. Deb, A. Pratap, S. Agarwal, and T. Meyarivan, "A fast and elitist multiobjective genetic algorithm: NSGA-II," *IEEE Trans. Evol. Comput.*, vol. 6, no. 2, pp. 182–197, 2002, doi: 10.1109/4235.996017.

[158] N. Stander and K. J. Craig, "On the robustness of a simple domain reduction scheme for simulation-based optimization," *Eng. Comput.*, vol. 19, no. 4, pp. 431–450, 2002, doi: 10.1108/02644400210430190.

[159] R. Allmendinger, M. T. M. Emmerich, J. Hakanen, Y. Jin, and E. Rigoni, "Surrogate-assisted multicriteria optimization: Complexities, prospective solutions, and business case," *J. Multi-*

Criteria Decis. Anal., vol. 24, no. 1–2, pp. 5–24, 2017, doi: 10.1002/mcda.1605.

[160] Y. Liu, "Design optimisation of tapered thin-walled square tubes," *Int. J. Crashworthiness*, vol. 13, no. 5, pp. 543–550, 2008, doi: 10.1080/13588260802222102.

[161] G. Chen, M. F. Shi, and T. Tyan, "Cross-Section Optimization for Axial and Bending Crushes Using Dual Phase Steels," *SAE Int. J. Mater. Manuf.*, Apr. 2009, doi: 10.4271/2008-01-1125.

[162] T. N. Tran, A. Baroutaji, Q. Estrada, A. Arjunan, H. S. Le, and N. P. Thien, "Crashworthiness analysis and optimization of standard and windowed multi-cell hexagonal tubes," *Struct. Multidiscip. Optim.*, no. 2004, 2021, doi: 10.1007/s00158-020-02794-y.

[163] Q. Liu, K. Liufu, Z. Cui, J. Li, J. Fang, and Q. Li, "Multiobjective optimization of perforated square CFRP tubes for crashworthiness," *Thin-Walled Struct.*, vol. 149, no. May 2019, p. 106628, 2020, doi: 10.1016/j.tws.2020.106628.

[164] R. Qin, J. Zhou, and B. Chen, "Crashworthiness Design and Multiobjective Optimization for Hexagon Honeycomb Structure with Functionally Graded Thickness," *Adv. Mater. Sci. Eng.*, vol. 2019, 2019, doi: 10.1155/2019/8938696.

[165] R. Lu, W. Gao, X. Hu, W. Liu, Y. Li, and X. Liu, "Crushing analysis and crashworthiness optimization of tailor rolled tubes with variation of thickness and material properties," *Int. J. Mech. Sci.*, vol. 136, pp. 67–84, 2018, doi: 10.1016/j.ijmecsci.2017.12.020.

[166] J. Song, S. Xu, S. Liu, and M. Zou, "Study on the crashworthiness of bio-inspired multi-cell tube under axial impact," *Int. J. Crashworthiness*, vol. 0, no. 0, pp. 1–10, 2020, doi: 10.1080/13588265.2020.1807686.

[167] H. Nikkhah, A. Baroutaji, and A. G. Olabi, "Crashworthiness design and optimisation of windowed tubes under axial impact loading," *Thin-Walled Struct.*, vol. 142, no. May, pp. 132–148, 2019, doi: 10.1016/j.tws.2019.04.052.

[168] F. Usta, Z. Eren, H. Kurtaran, H. S. Türkmen, Z. Kazancı, and Z. Mecitoglu, "Crashworthiness optimization of nested and concentric circular tubes using response surface methodology and genetic algorithm," *Lat. Am. J. Solids Struct.*, vol. 15, no. 5, 2018, doi: 10.1590/1679-78254385.

[169] A. Baroutaji, M. Sajjia, and A. G. Olabi, "On the crashworthiness performance of thin-walled energy absorbers: Recent advances and future developments," *Thin-Walled Struct.*, vol. 118, no. April, pp. 137–163, 2017, doi: 10.1016/j.tws.2017.05.018.

[170] P. Bandi, D. Detwiler, J. P. Schmiedeler, and A. Tovar, "Design of progressively folding thin-walled tubular components using compliant mechanism synthesis," *Thin-Walled Struct.*, vol. 95, pp. 208–220, 2015, doi: 10.1016/j.tws.2015.06.010.

[171] J. Forsberg and L. Nilsson, "On polynomial response surfaces and Kriging for use in structural optimization of crashworthiness," *Struct. Multidiscip. Optim.*, vol. 29, no. 3, pp. 232–243, 2005, doi: 10.1007/s00158-004-0487-8.

[172] J. Song, "Numerical simulation on windowed tubes subjected to oblique impact loading and a new method for the design of obliquely loaded tubes," *Int. J. Impact Eng.*, vol. 54, pp. 192–205, 2013, doi: 10.1016/j.ijimpeng.2012.11.005.

[173] Z. Bai, J. Liu, F. Zhu, F. Wang, and B. Jiang, "Optimal design of a crashworthy octagonal thin-walled sandwich tube under oblique loading," *Int. J. Crashworthiness*, vol. 20, no. 4, pp. 401–411, 2015, doi: 10.1080/13588265.2015.1024995.

[174] W. Guan, G. Gao, J. Li, and Y. Yu, "Crushing analysis and multi-objective optimization of a cutting aluminium tube absorber for railway vehicles under quasi-static loading," *Thin Walled Struct.*, vol. 123, no. December 2017, pp. 395–408, 2018, doi: 10.1016/j.tws.2017.11.031.

[175] A. Baroutaji, M. D. Gilchrist, D. Smyth, and A. G. Olabi, "Crush analysis and multi-objective optimization design for circular tube under quasi-static lateral loading," *Thin-Walled Struct.*, vol. 86, pp. 121–131, 2015, doi: 10.1016/j.tws.2014.08.018.

[176] C. P. Kohar, M. Cherkaoui, H. El Kadiri, and K. Inal, "Numerical modeling of TRIP steel in axial crashworthiness," *Int. J. Plast.*, vol. 84, pp. 224–254, 2015, doi: 10.1016/j.ijplas.2016.05.010.

[177] Ted Belytschko, Bak Leong Wong, and Huai-Yang Chiang, "Advances in one-point quadrature shell elements," *Comput. Methods Appl. Mech. Eng.*, vol. 96, no. 1, pp. 93–107, 1992, doi: 10.1016/0045-7825(92)90100-X.

[178] T. Belytschko, J. I. Lin, and T. Chen-Shyh, "Explicit algorithms for the nonlinear dynamics of shells," *Comput. Methods Appl. Mech. Eng.*, vol. 42, no. 2, pp. 225–251, Feb. 1984, doi: 10.1016/0045-7825(84)90026-4.

[179] SAE, "J211-1," 1995, doi: 10.1520/G0154-12A.

[180] C. Qi, Z. Ma, N. Kikuchi, C. Pierre, and B. Raju, "A Magic Cube Approach for Crashworthiness Design," *Design*, vol. 2006, no. 724, 2006, doi: 10.4271/2006-01-0671.

[181] S. Hu, Z.-D. Ma, C. Qi, and Y. Ding, "Front Rail Crashworthiness Design for Front Oblique Impact Using a Magic Cube Approach," pp. 100–113, 2013, doi: 10.4271/2013-01-0651.

[182] J. Marzbanrad, M. Ebrahimi-F, and M. Khosravi, "Optimization of crush initiators on steel front rail of vehicle," *Int. J. Automot. Eng.*, vol. 4, no. 2, pp. 749–757, 2014.

[183] J. Song and F. Guo, "A comparative study on the windowed and multi-cell square tubes under axial and oblique loading," *Thin-Walled Struct.*, vol. 66, pp. 9–14, 2013, doi: 10.1016/j.tws.2013.02.002.

[184] D.-Z. Wang, G.-J. Cao, C. Qi, Y. Sun, S. Yang, and Y. Du, "Crushing analysis and lightweight design of tapered tailor welded hybrid material tubes under oblique impact," *SAE Int. J. Mater. Manuf.*, vol. 9, no. 3, pp. 2016-01–0407, 2016, doi: 10.4271/2016-01-0407.

[185] J. Fender, F. Duddeck, and M. Zimmermann, "On the calibration of simplified vehicle crash models," *Struct. Multidiscip. Optim.*, vol. 49, no. 3, pp. 455–469, Mar. 2014, doi: 10.1007/s00158-013-0977-7.

[186] X. Gu, G. Sun, G. Li, L. Mao, and Q. Li, "A Comparative study on multiobjective reliable and robust optimization for crashworthiness design of vehicle structure," *Struct. Multidiscip. Optim.*, vol. 48, no. 3, pp. 669–684, Sep. 2013, doi: 10.1007/s00158-013-0921-x.

[187] G. M. Nagel and D. P. Thambiratnam, "Dynamic simulation and energy absorption of tapered thin-walled tubes under oblique impact loading," *Int. J. Impact Eng.*, vol. 32, no. 10, pp. 1595–1620, 2006, doi: 10.1016/j.ijimpeng.2005.01.002.

[188] S. Shinde, P. Bandi, D. Detwiler, and A. Tovar, "Structural Optimization of Thin-Walled Tubular Structures for Progressive Buckling Using Compliant Mechanism Approach," *SAE Int. J. Passeng. Cars - Mech. Syst.*, vol. 6, no. 1, pp. 2013-01–0658, 2013, doi: 10.4271/2013-01-0658.

[189] J. S. Qiao, J. H. Chen, and H. Y. Che, "Crashworthiness assessment of square aluminum extrusions considering the damage evolution," *Thin-Walled Struct.*, vol. 44, no. 6, pp. 692–700, 2006, doi: 10.1016/j.tws.2006.04.015.

[190] O. M. Qureshi and E. Bertocchi, "Crash behavior of thin-walled box beams with complex sinusoidal relief patterns," *Thin-Walled Struct.*, vol. 53, pp. 217–223, 2012, doi: 10.1016/j.tws.2011.12.006.

[191] B. W. Silverman, "Density Estimation for Statistics and Data Analysis," *Monogr. Stat. Appl. Probab.*, 1986.

[192] D. E. Malen, *Fundamentals of automobile body structure design*. Warrendale, PA: SAE International, 2011.

[193] F. Pedregosa *et al.*, "Scikit-learn: Machine Learning in Python," *J. Mach. Learn. Res.*, vol. 12, pp. 2825–2830, 2011.

[194] F.-A. Fortin, F.-M. De Rainville, M.-A. Gardner, M. Parizeau, and C. Gagné, "DEAP: Evolutionary Algorithms Made Easy," *J. Mach. Learn. Res.*, vol. 13, pp. 2171–2175, 2012.

[195] S. Wessing, "diversipy: sample in hypercubes, select diverse subsets, and evaluate diversity indicators," 2018. https://pypi.python.org/pypi/diversipy.

[196] C. Zhu, R. H. Byrd, P. Lu, and J. Nocedal, "Algorithm 778: L-BFGS-B," *ACM Trans. Math. Softw.*, vol. 23, no. 4, pp. 550–560, Dec. 1997, doi: 10.1145/279232.279236.

[197] Y. Bao and T. Wierzbicki, "On fracture locus in the equivalent strain and stress triaxiality space," *Int. J. Mech. Sci.*, vol. 46, no. 1, pp. 81–98, Jan. 2004, doi: 10.1016/j.ijmecsci.2004.02.006.

[198] Y. Bai and T. Wierzbicki, "A new model of metal plasticity and fracture with pressure and Lode dependence," *Int. J. Plast.*, vol. 24, no. 6, pp. 1071–1096, Jun. 2008, doi: 10.1016/j.ijplas.2007.09.004.

[199] Y. Bai and T. Wierzbicki, "Application of extended Mohr–Coulomb criterion to ductile fracture," *Int. J. Fract.*, vol. 161, no. 1, pp. 1–20, Jan. 2010, doi: 10.1007/s10704-009-9422-8.

[200] F. Neukamm, M. Feucht, and A. Haufe, "Consistent damage modelling in the process chain of forming to crashworthiness simulations," in *LS-DYNA Anwenderforum*, 2008, pp. 11–20.

[201] J. Effelsberg, A. Haufe, M. Feucht, F. Neukamm, and P. Du Bois, "On parameter identification for the GISSMO damage model," in *12th International LS-DYNA Users Conference*, 2012, pp. 1–12.

[202] F. X. C. Andrade, M. Feucht, A. Haufe, and F. Neukamm, "An incremental stress state dependent damage model for ductile failure prediction," *Int. J. Fract.*, vol. 200, no. 1–2, pp. 127–150, Jul. 2016, doi: 10.1007/s10704-016-0081-2.